Dielectric elastomer actuators

Cite as: J. Appl. Phys. **129**, 151102 (2021); https://doi.org/10.1063/5.0043959
Submitted: 12 January 2021 • Accepted: 19 March 2021 • Published Online: 19 April 2021

Ehsan Hajiesmaili and David R. Clarke

Journal of Applied Physics TUTORIAL scitation.org/journal/jap

Dielectric elastomer actuators

Cite as: J. Appl. Phys. **129**, 151102 (2021); doi: 10.1063/5.0043959
Submitted: 12 January 2021 · Accepted: 19 March 2021 ·
Published Online: 19 April 2021

Ehsan Hajiesmaili[a] and David R. Clarke

AFFILIATIONS

School of Engineering and Applied Sciences, Harvard University, Cambridge, Massachusetts 02138, USA

[a]**Authors to whom correspondence should be addressed:** hajiesmaili@seas.harvard.edu

ABSTRACT

Dielectric elastomer actuators (DEAs) are soft, electrically powered actuators that have no discrete moving parts, yet can exhibit large strains (10%–50%) and moderate stress (~100 kPa). This Tutorial describes the physical basis underlying the operation of DEA's, starting with a simple linear analysis, followed by nonlinear Newtonian and energy approaches necessary to describe large strain characteristics of actuators. These lead to theoretical limits on actuation strains and useful non-dimensional parameters, such as the normalized electric breakdown field. The analyses guide the selection of elastomer materials and compliant electrodes for DEAs. As DEAs operate at high electric fields, this Tutorial describes some of the factors affecting the Weibull distribution of dielectric breakdown, geometrical effects, distinguishing between permanent and "soft" breakdown, as well as "self-clearing" and its relation to proof testing to increase device reliability. New evidence for molecular alignment under an electric field is also presented. In the discussion of compliant electrodes, the rationale for carbon nanotube (CNT) electrodes is presented based on their compliance and ability to maintain their percolative conductivity even when stretched. A procedure for making complaint CNT electrodes is included for those who wish to fabricate their own. Percolative electrodes inevitably give rise to only partial surface coverage and the consequences on actuator performance are introduced. Developments in actuator geometry, including recent 3D printing, are described. The physical basis of versatile and reconfigurable shape-changing actuators, together with their analysis, is presented and illustrated with examples. Finally, prospects for achieving even higher performance DEAs will be discussed.

I. INTRODUCTION

The goal of creating artificial muscles with performances comparable to mammalian muscles has proven to be a rallying call to scientists and engineers, particularly in the soft robotics community. Several different active polymer approaches have been proposed[1] for reaching this goal, but in this Tutorial, we focus on dielectric elastomer actuators (DEAs). DEAs are solid electrostatic actuators, with no discrete moving parts, that can be controlled electrically to produce large actuation strains and high energy densities on a par with mammalian muscles and over a moderate range of frequencies (up to <1 kHz). Fundamental to the actuator performance is the use of thin elastomers as the dielectric, sandwiched between compliant electrodes, because elastomers exhibit the unusual combination of being soft, highly extensible, and nearly incompressible.

A DEA, in its simplest configuration, consists of an elastomer layer that is coated by compliant electrodes on its two opposite surfaces [Fig. 1(a) (left)]. Applying a voltage to the compliant electrodes compresses the elastomer in thickness due to the Coulombic attraction of opposite charges and causes lateral expansions of the elastomer due to its incompressibility [Fig. 1(a) (right)]. The notion that DEAs could be used as an artificial muscle was proposed in 2000 by Pelrine *et al.*[2,3] According to Google Scholar, publications in which "dielectric elastomer actuators" are discussed has increased from 14 publications per year in 2000 to over 800 in 2019. To date, more than 6000 articles and book chapters on dielectric elastomer actuators have been published. Early on, much of the research consisted of demonstrations of electrically driven actuation using thin elastomer membranes, usually held on a frame to keep them taut [Fig. 1(b)]. One of the major concerns at the time was avoiding electromechanical instability leading to abrupt failure. Although this instability had first been described in the 1950s[4] and is now recognized as an abrupt "snap-through" thinning above a critical electrical field [Fig. 2(a)], it was found empirically that the instability could be forestalled by prestretching the elastomer.[2] This necessitated the use of a rigid frame, limiting possible actuator designs. By introducing a rigorous thermodynamic basis for describing the mechanics of actuation, Suo *et al.* showed that the strain stiffening of prestretched elastomers is the reason for

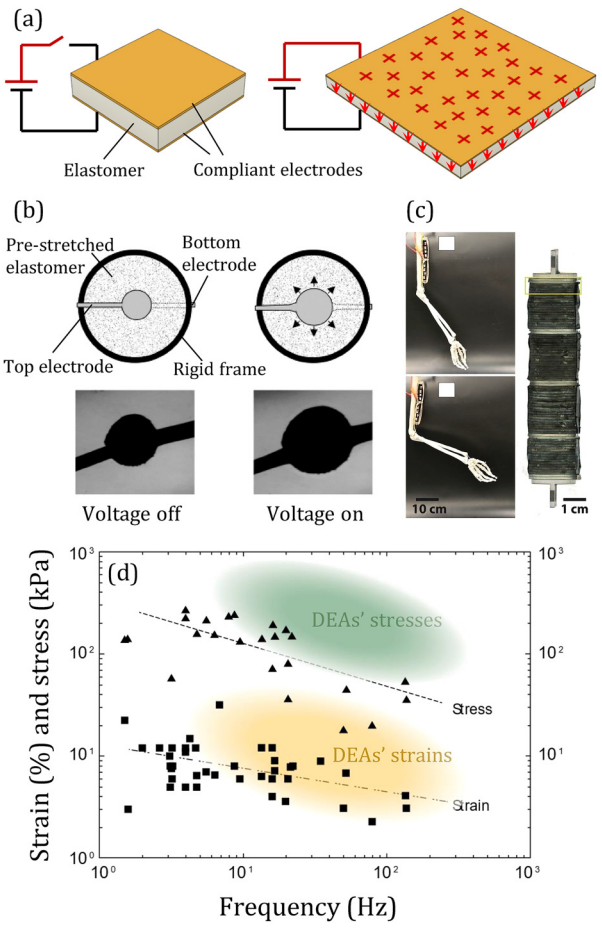

FIG. 1. Physical basis and examples of DEA devices, and their performance compared to skeletal muscles. (a) A DEA, in its simplest configuration, consists of a layer of soft elastomer sandwiched between two compliant electrodes (left) that contracts in thickness under an applied voltage (right) due to Coulombic attractions of opposite charges on the two electrodes. The red arrows represent the electric field vectors inside the elastomer. (b) One of the first demonstrations of dielectric elastomer actuation consisted of a film of a commercial elastomer stretched on a circular frame with painted carbon grease as the compliant electrodes, showing an area expansion of 68% under DC applied voltages.[2] Reproduced with permission from Pelrine *et al.*, Science **287**(5454), 836–839 (2000). Copyright 2000 The American Association for the Advancement of Science. (c) An example of a multilayer DEA used as the artificial muscle on a real-size human skeleton.[27] (d) The actuation stresses and strains that DEAs produce with current materials and technology, shown by color shading, are on a par with that of the natural muscles shown by the data points.[23,28] Typical stresses and strains of natural muscles are ~100 kPa and ~10%, respectively, operating over frequencies up to ~100 Hz, both of which decrease with the actuation frequency. From Full, *Comprehensive Physiology.* Copyright 2010 John Wiley and Sons. Reproduced with permission from Wiley Books.

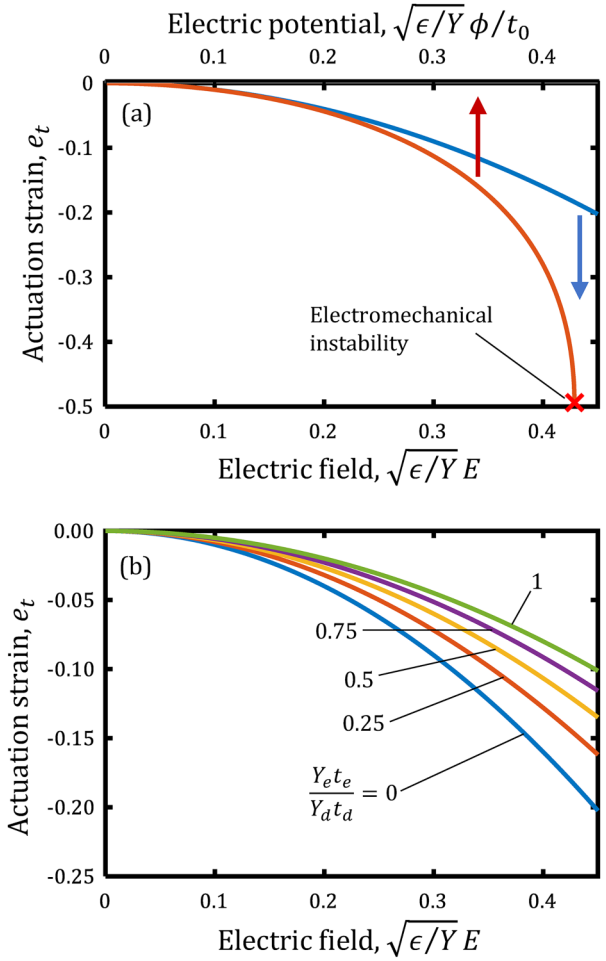

FIG. 2. Actuation strains of biaxial DEAs as described by linear elasticity. (a) The actuation strain, $e_t = \log(t/t_0)$, varies with the square of the non-dimensional electric field, $\sqrt{\epsilon/Y}E$, assuming the electrodes are fully compliant, and the strain varies nonlinearly with the non-dimensional applied voltage, $\sqrt{\epsilon/Y}\,\phi/t_0$. The electromechanical instability point is indicated. (b) Compliance of the electrodes plays a key role in achieving large actuation deformations: the more compliant the electrode the larger the attainable actuation strains.

preventing the instability and the instability could also be avoided by using an elastomer with certain strain-stiffening characteristics without prestretching.[5–7] This removed the constraint of having to use a rigid frame to support the actuator, enabling new design configurations. It was also increasingly recognized that devices require elastomer/electrode multilayer configurations[8–11] in order to generate sufficiently large forces at moderate applied voltages [Fig. 1(c)].

Since those early studies, considerable advances have been made toward the goal of producing dielectric elastomer artificial muscles. These include elastomer materials engineered to show optimum strain-stiffening behaviors; electrodes optimized for high compliance, electrical conductivity, and self-clearing; new functionalities such as self-sensing have been added; a variety of different configurations proposed; and numerous novel devices based on DEAs have been demonstrated. Many of these advances can be

found in the review articles on DEAs[12–21] and will not be discussed in this Tutorial.

To place dielectric elastomer actuator performance in context, it is useful to compare some of their characteristics with those of mammalian muscles as well as other types of actuators. Skeletal muscles are made up of repeating units, called sarcomeres, consisting of actin–myosin segments.[22] These can produce contractile stresses that range from less than 100 kPa up to 1000 kPa,[3,23,24] as shown in Fig. 1(d). The actuation strains of the skeletal muscles are typically less than 10%.[23] In addition to the actual values, muscle tissues show their maximum force near zero strain where the actin–myosin overlap is maximum and approaches nearly zero at the maximum actuation strain where the actin–myosin overlap is nearly zero.[25] As will be described in Sec. II, both the maximum forces and actuation strain capabilities of multilayer DEAs can match and even exceed those of natural muscles. For instance, for an elastomer with a typical electrical breakdown strength of $\sim 100\,\mathrm{V}\,\mu\mathrm{m}^{-1}$ and permittivity of $\sim 3\epsilon_0$, the maximum blocking force per area according to Eq. (3), $F/A = \epsilon E^2$, is larger than 250 kPa, which is on par with that quoted for skeletal muscles. The actuation strain that a DEA can produce depends on the stiffness behavior of the elastomer [Eqs. (1) and (20)] and can be as large as 100% laterally,[26] which corresponds to a decrease of 75% in thickness, although the maximum actuation strains more typically fall in the range of 10%–30% laterally, i.e., between 17% and 40% decrease in thickness. The actuation force vs strain for DEAs has its maximum at zero strain, called the blocking force, and becomes zero at maximum actuation strain [Fig. 3(b)] resembling the actuation force-strain behavior of natural muscles. Equations (3) and (20) describe the quasi-static force–displacement characteristic of a biaxial DEA. Although not the focus of this article, the bandwidth of DEAs and skeletal muscles are also similar, as well as their energy densities.

More generally, actuators can be characterized in terms of three independent parameters: the forces and displacements they can produce and their frequency bandwidth. Pneumatic and hydraulic actuators can be designed to produce combinations of arbitrarily large forces and large displacements, but their bandwidth is small (few Hz) and decreases with increasing size. By contrast, at the other extreme, piezoelectric actuators can operate over a large bandwidth (hundreds of MHz and above) and produce large forces, but the displacements are small, usually micrometers, unless embodied into a stepping motor device. In comparison, dielectric elastomers actuators occupy a more restricted region in this three-dimensional space, generating small forces at frequencies up to ~1 kHz but with displacements of millimeter to centimeters, a range of interest in haptics and soft robotics. Other favorable comparisons can be drawn in terms of specific powers and energies since the densities of elastomers are so much lower than other engineering materials. However, the biggest advantage is that their mechanical properties are comparable to those of skin and there are no discrete moving parts.

This Tutorial seeks to describe the key, relatively mature concepts as well as areas where it can confidently be anticipated that with future developments artificial muscles will not only exceed the force–displacement characteristics of some of the best mammalian muscles but also will be capable of new, shape-morphing capabilities. The organization of this paper is as follows. In Sec. II, the physical basis for DEA is first described in terms of the "compliant capacitor model" in which the deformation of a soft material by electrostatic forces in a parallel plate configuration is considered. This is useful conceptually even though the equations usually reported in the literature are based on the linear elastic behavior. These equations are usually too simplistic because elastomers rarely behave as linear elastic solids and many of the important consequences, such as the details of the electromechanical instability and the required constitutive elastomer mechanical properties to avoid premature instability, cannot be captured in terms of linear elasticity. Instead, the large, nonlinear elastic response, characteristic of elastomers, need to be incorporated in deriving equations relating the displacements, geometry, and applied voltage. This is presented in Sec. III that describes a consistent mathematical description for deriving these relationships. Section IV is devoted to the mechanical responses of elastomers, aspects of their electrical breakdown, and methods being employed to increase their dielectric constant. In Sec. V, approaches to creating compliant electrodes using percolating networks of carbon nanotubes (CNTs) are described together with the consequences on the mechanical stiffness and strain cycling. Appendix B presents the method we often use for preparing and transferring CNT electrodes. Section VI describes actuator geometries that are different implementations of the basic compliant capacitor configuration. Finally, before summarizing the prospects for future developments, Sec. VII describes shape-changing actuators, a different path in the evolution of electrically driven and reversible actuators.

II. PHYSICAL BASIS OF ELECTROSTATIC ACTUATIONS OF DIELECTRIC ELASTOMERS

DEAs are devices that convert electrostatic energy, provided by an external electric potential, to strain energy and mechanical work through the deformation of a soft dielectric. The simplest actuator configuration is analogous to a parallel plate capacitor and consists of a thin elastomer sheet between two conducting electrodes to which a potential can be applied [Fig. 1(a)]. When connected to a power supply, one electrode becomes positively charged and the other one correspondingly becomes negative. The opposite charges attract one another creating a net Coulombic attraction acting through the elastomer subjecting it to a compressive force. The areal density of charges on each electrode is proportional to the applied electric field, E, and the electric permittivity of the dielectric, ϵ, i.e., $q = \pm\epsilon E$, which results in a compressive stress, $P = qE$, that is proportional to the square of the electric field, $P = \varepsilon E^2$. The electric field is the applied voltage, ϕ, divided by the thickness of the dielectric layer, t. In response, the dielectric deforms by decreasing in thickness until the net electrostatic attraction is balanced by the mechanical stress, σ_t, resisting the deformation which for small linear elastic strains is proportional to Young's modulus, Y, and the (true) strain in thickness direction, e_t, i.e., $\sigma_t = Ye_t$. [True strain is the natural logarithm of final thickness divided by the initial thickness $e_t = \ln(t/t_0)$.] Linear elasticity is used throughout this section to give a simple and qualitatively description of the physical basis of the DEAs; a more rigorous mathematical analysis of DEAs under large deformations will be

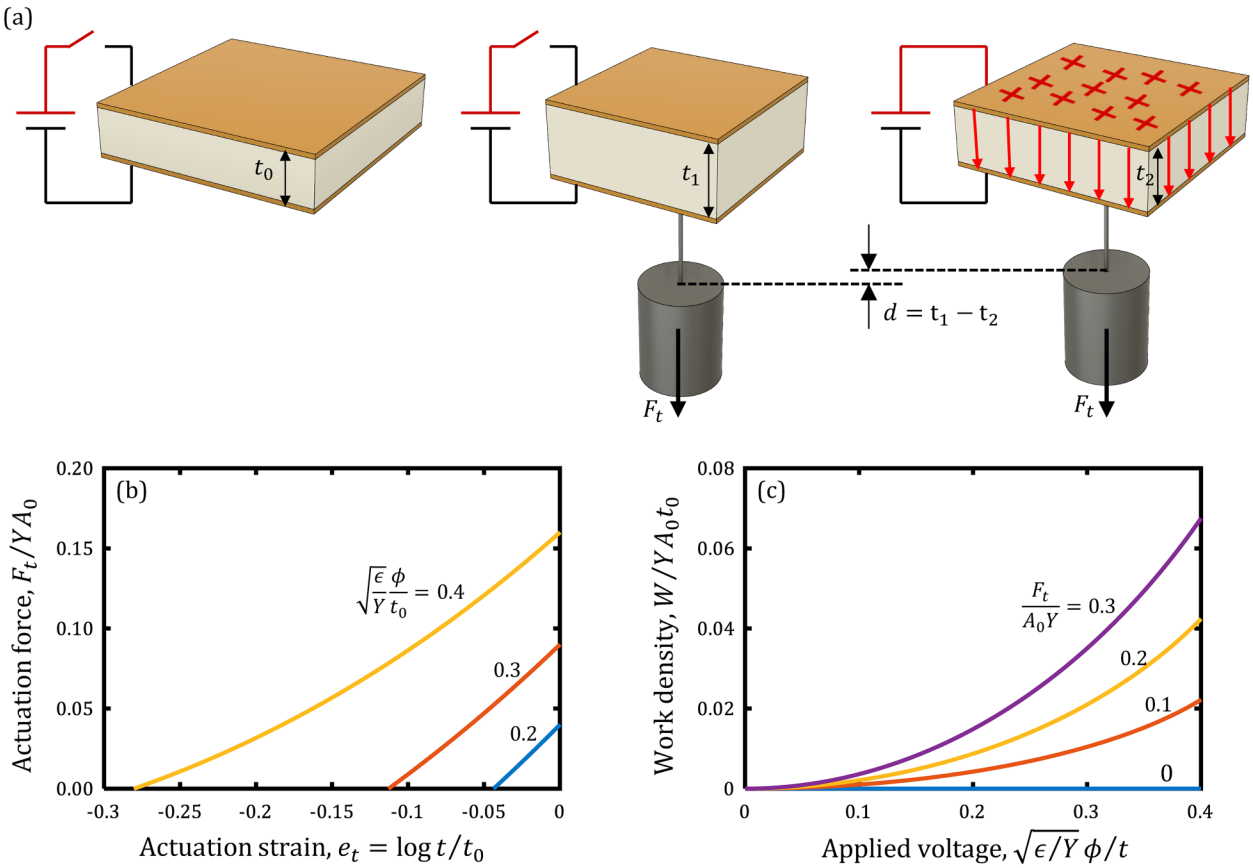

FIG. 3. Actuation force and work output of dielectric elastomer actuators. (a) A dielectric elastomer actuator having an initial thickness of t_0 (left) is first stretched by a dead load, F_t, reaching a thickness of t_1 (middle). The voltage is then applied (right) that lifts the load up against gravity by $d = t_1 - t_2$. (b) The force balance in the right figure in (a) leads to actuation forces that decrease with the strain, having a maximum of $F_t = A\epsilon E^2$ at $e_t = 0$, the blocking force, and decreasing to zero at $e_t = -\epsilon E^2/Y$. The actuation forces increase with the non-dimensional applied voltage. (c) The non-dimensional work done by the DEA on the dead load, F_t, when the voltage is applied is $W/A_0t_0Y = (F_t/A_0Y)(d/t_0)$.

presented in Sec. III. At force equilibrium, the relationship between the applied electric field and the decrease in thickness can be written as

$$e_t = -P/Y = -\varepsilon E^2/Y. \tag{1}$$

This is plotted in Fig. 2(a), the blue curve. The through-thickness actuation strain is proportional to the square of the non-dimensional electric field, $\sqrt{\epsilon/Y}E$. This non-dimensional parameter appears in all analyses of DEAs with the shear modulus, μ, replacing Young's modulus for large deformations, i.e., as $\sqrt{\epsilon/\mu}E$, as will be discussed in Sec. III.

Although Eq. (1) only applies for small deformations and for linear elastic dielectrics, it is useful, even with these restrictions, to compare the strains for different classes of dielectrics (Table I). For instance, common dielectrics, such as oxides and high-field polymers, are stiff and consequently cannot deform appreciably under these Coulombic forces; thus, their displacements and strains are tiny, typically of the order of 10^{-9} per V/μm. Significantly, because the shear moduli of elastomers are orders of magnitude smaller than oxides and even most polymers, their displacements are correspondingly far larger. In terms of energy conversion, the ratio of the strain energy density stored in the DEA, $Ye_t^2/2$, to its electrostatic energy density, $\epsilon E^2/2$, is $\varepsilon E^2/Y$. This indicates that the low elastic modulus of elastomers is key to converting appreciable electrostatic energy into the mechanical strain energy; a stiff material acts as an electrical capacitor storing most of the input electrical energy in the form of electrostatic energy, whereas a soft elastomer acts as an actuator converting a significant portion of the input energy into mechanical strain energy. As will be shown later, the work done on an external load also scales with $1/Y$. To fully appreciate the advantages of using an elastomer as the dielectric in an actuator, three other key attributes of elastomer materials need to be taken into account: they are incompressible, they can deform by large amounts before rupturing, and they behave as "liquid-like" dielectrics.

TABLE I. Properties of actuator materials.

Material	Density (kg/m^3)	Shear modulus (MPa)	Poisson ratio	Recoverable elastic limit (%)	Dielectric permittivity
Gold[a]	19 320	30 000	0.3	0.02	N/A
Aluminum[a]	2730	70 000	0.3	0.02	N/A
Low density polyethylene	965	~730	~0.44	0.4	2.2
Polypropylene sheet	913	~612	~0.46	15	2.2
Polyaniline[b]	1360	~1000	N/A	1.0	>100
Conjugated polymer, PDOT[b]	1011	~1200	N/A	2.0	>100
PDMS—Sylgard 10:1	1030	0.44	~0.5	>100	2.7
Acrylic[b]	~960	0.3	~0.5	>100	5.5
Eco-flex	~1050	0.1	~0.5	~500	3.2

[a]Polycrystalline, pure elements.
[b]Blends: properties depend on amount of cross-linking.

Being nearly incompressible, elastomers have a Poisson ratio close to 0.5. In the context of Fig. 1(a), the compressive stress in the electric field direction creates a compressive strain through the thickness, which, by the Poisson effect, means that the elastomer expands laterally with the lateral strain being equal to half of the thickness contraction strain, $e_l = -e_t/2 = \varepsilon E^2/2Y$, assuming that the strains are infinitesimal. Being highly extensible, the elastomer strains can be very large, beyond the usual deformation regimes described by infinitesimal elasticity theory where the strains are linearly related to stresses; in some special cases, the strains can be many hundred percent,[29] and for this reason, the deformations are often described in terms of "stretches" rather than strains. (For simple equibiaxial and uniaxial actuators, stretch can be defined as the length upon straining divided by the original length, that is, $\lambda_1 = l/l_0$, $\lambda_2 = w/w_0$, and $\lambda_3 = t/t_0$, where l, w, and t are the length, width, and thickness of the elastomer layer after actuation, respectively, and the subscript 0 corresponds to the initial dimensions under zero voltages and forces.) Furthermore, a consequence of the molecular structure of elastomers is that their elastic deformation is nonlinearly (but reversibly) related to the stress imposed on them. Also, unlike many crystalline dielectrics, the dielectric properties of elastomers are independent of deformation and isotropic, as liquid dielectrics are.

Increasing the applied voltage, ϕ, not only directly increases the electric field inside the elastomer, $E = \phi/t$, but also squeezes the elastomer in thickness, causing a further increase in electric field by reducing t. At sufficiently large applied voltages, this positive feedback between the electric field and the thickness strain leads to an abrupt decrease in elastomer thickness, the so-called electromechanical instability. This is analogous to the "pull-in" instability in MEMS cantilevered electrostatic switches.[30] The instability results in a sudden increase in electric field, which may exceed the electrical breakdown strength of the elastomer and cause failure. To estimate the critical strain at which the electro mechanical instability occurs, the thickness, t, is related to the initial thickness of the elastomer, t_0, and the true strain, $e_t = \log(t/t_0)$, which results in a nonlinear equation for the true strain: $e_t = -\varepsilon\phi^2/Yt_0^2 \exp(2e_t)$. This is plotted in Fig. 2(a), the red curve. At electromechanical instability, no additional voltage is required to increase the strain, i.e., $\partial\phi/\partial e_t = 0$, which yields the critical strain at electromechanical instability: $e_t = -50\%$ or $t/t_0 = 0.6$.[4] This value is very close to that established using the large deformation analysis discussed in Sec. III. It is important, though, to emphasize that the use of engineering strain instead of the true strain can be misleading since it describes the DEAs as monotonic systems exhibiting no electromechanical instabilities.

The analysis leading to Eq. (1) implicitly assumes that the electrodes are completely compliant meaning that they extend in area to match the lateral expansion of the elastomer and, furthermore, exert no resistance or constraint to the lateral elongation of the elastomer. In practice, however, no electrode is fully compliant and always shows some level of resistance to lateral elongation, reducing the electric field induced deformation of the elastomer from $\varepsilon E^2/2Y_d$ to a smaller lateral strain, e_l (subscript d refers to the dielectric). An estimate of the effect of the electrode constraint can be obtained assuming that the electrodes are attached to the elastomer and no slip occurs between the electrodes and the elastomer. Under these conditions, both the electrodes and elastomer have the same lateral strain, e_l. The expanding elastomer stretches the electrode causing a tensile lateral stress in the electrode, $\sigma_e = Y_e e_l$, constraining the lateral expansion of the elastomer and causing a compressive lateral stress in the elastomer, $\sigma_d = Y_d(e_l - \varepsilon E^2/2Y_d)$ (subscript e refers to the electrode). Mechanical equilibrium on a cross section through the elastomer and the two electrodes requires that $\sigma_d t_d = 2\sigma_e t_e$, enabling the strains to be expressed as

$$e_l = \frac{\varepsilon E^2/2Y_d}{1 + 2Y_e t_e/Y_d t_d}, \quad e_t = -2e_l = -\frac{\varepsilon E^2/Y_d}{1 + 2Y_e t_e/Y_d t_d}. \tag{2}$$

So, as shown in Fig. 2(b), to achieve the largest actuation deformations, the product of the electrode stiffness and its thickness must be much smaller than that of the elastomer, $Y_e t_e \ll Y_d t_d$. The constraining effect can, equivalently, be understood in terms of the additional strain energy required to deform the electrode materials as described by Eq. (29) in Sec. III and results in the same conclusion; the product of the electrode

thickness and modulus must be as small as possible to minimize the constraint from the electrodes and thereby maximize the actuation stretch. This is not achievable with metals that are commonly used as electrodes; for example, even a 1 nm thick layer of aluminum causes a constraining effect, $Y_e t_e \sim 70$ Pa m, even larger than that of a 100 μm thick silicone elastomer, $Y_d t_d \sim 30$ Pa m. Currently available conductive polymers are also too stiff to be used as the electrodes primarily because their electrical conduction relies on charge transfer along stiff polymer chains. For example, polyaniline, an electrically conductive polymer with a modulus of elasticity of ~1 GPa, must have its thickness in the order of ~1 nm in order to achieve $Y_e t_e / Y_d t_d < 10\%$. However, it may be possible in the future to synthesize new conducting polymers having stretchability and low shear modulus characteristics of elastomers, just as there exist soft liquid crystal elastomers containing long stiff molecules. It is also implicitly assumed that the electrodes can stretch elastically by large strains without rupturing or cracking and return to their original size when the electric potential is removed. Metals and conductive polymers are incapable of elastically deforming to large strains as their yield strains are typically small—less than a few percent in even the purest metals.

At present, the possible solutions for compliant electrodes are mats of conductive nanoparticles, liquid metals, and ionogels. Of all possible metals, liquid metals come closest to having the lowest resistance to deformation, but at present they cannot be made sufficiently thin to take advantage of their low flow stress, especially at higher frequencies. Another possibility is to use an ionogel or ionic liquids; however, they can diffuse into elastomer and cause electrical breakdown. A liquid electrode may also limit possible applications because it lacks any tensile strength limiting adhesion. As will be described in Sec. V, the best practical approach for compliant electrodes of DEAs, at present, are thin electrodes consisting of mats of nanowires, carbon nanotubes, or other conductive nanoparticles, which are deposited onto the surfaces of the elastomer layers or embedded in an elastomer while remaining electrically conducting by percolation between them.

As artificial muscles, DEAs must be able to do mechanical work by displacing loads, and therefore, the actuation forces are of prime importance. The force balance between the external load, F_P, parallel to the direction of electric field vector, the Coulombic attractions, and internal stresses of the DEA in Fig. 3(a) (right) gives

$$e_t = \frac{F_P}{YA} - \frac{\epsilon E^2}{Y}, \tag{3}$$

in which A is the surface area of the DEA. The largest actuation deformation occurs when the actuation force, F_P, has decreased to zero, namely, when $e_t = -\epsilon E^2/Y$. At the other extreme, when the elastomer is not allowed to deform at all, $e_t = 0$, the actuation force is at its maximum, $F_t = A\epsilon E^2$, which is often referred to as the blocking force. Significantly, the blocking force is independent of the elasticity of the elastomer. Anywhere in between, the actuation force varies linearly with the strain from its maximum $F_t = A\epsilon E^2$ at zero strain $e_t = 0$ to zero force $F_t = 0$ at the maximum strain $e_t = -\epsilon E^2/Y$, assuming that the deformations are infinitesimal and the electric field is held constant. A more accurate representation of the force–displacement characteristic of the DEA at different voltages includes the change in surface area and thickness with voltage. These are given by $A = A_0/\exp(e_t)$ and $t = t_0\exp(e_t)$. The actuation strain then varies nonlinearly as $e_t = F_t\exp(e_t)/YA_0 - \epsilon\phi^2/Yt_0^2\exp(2e_t)$ [Fig. 3(b)], but the blocking force remains independent of the elastomer modulus.

To characterize the mechanical work output of the DEAs, the sequence of operations shown in Fig. 3(a) is considered. The elastomer is first subjected to a dead load while the voltage is off [Fig. 3(a) (middle)], which deforms the DEA by $e_t = \log(t_1/t_0) = F_t/A_1Y$. t_1 and A_1 are the thickness and surface area after deformation, respectively, and are related to each other through the incompressibility condition $A_0t_0 = A_1t_1$. Applying the voltage [Fig. 3(a) (right)] causes the elastomer to shrink in thickness, $e_t = \log(t_2/t_0) = F_t/A_2Y - \epsilon E^2/Y$, lifting the load by $d = t_1 - t_2$. The work done on the dead load by the DEA is $W = F_t d$. In terms of non-dimensional parameters, the work is W/A_0t_0Y, the force is F_t/A_0Y, and displacement is d/t_0, so $W/A_0t_0Y = (F_t/A_0Y)(d/t_0)$. The non-dimensional work and displacement scale with the thickness of the elastomer and are also functions of the applied load and the voltage. Figure 3(c) shows the work done on a dead load as a function of the applied voltage, obtained by numerically solving for t_1 and t_2 in $d = t_1 - t_2$ and then calculating for $W = F_t d$.

The actuation displacements, work, and even actuation forces (when applied laterally as opposed to the parallel forces discussed so far) all scale with the thickness of the elastomer layer. However, for a thick elastomer layer, extremely large electric potentials are required to achieve large electric fields, $E = \phi/t$. In practice, this limits the thickness of the elastomer layers that can be used for a given voltage. A simple and efficient way to achieve large actuation forces, displacements, and work, while maintaining the required voltage as low as possible, is to multilayer the DEA. A multilayer DEA consisting of n elastomer layers with a total thickness t requires a voltage that is n times smaller, as compared to a single-layer DEA of the same total thickness, to achieve the electric field $E = (\phi/n)/(t/n) = \phi/t$, and therefore, would show exactly the same performance as a thick single-layer DEA but at a fraction of the voltage. In addition, multilayering provides other attributes. For instance, as will be illustrated in Sec. VII, the ability to produce a multilayer structure also facilitates the fabrication of shape-morphing actuators by incorporating different electrode geometries within the actuator to create inhomogeneous internal electric fields. A multilayer DEA is also less susceptible to the local electromechanical instabilities since the surfaces of each layer are constrained by the other layers.

III. MATHEMATICAL DESCRIPTION OF ELECTROSTATIC ACTUATIONS OF DIELECTRIC ELASTOMERS

To emphasize the physical basis of the dielectric elastomer actuators, Sec. II was couched in terms of the small-scale, linear-elastic response of elastomers. However, one of the major reasons for using elastomers in actuators is that they can sustain very large strains, and elastic strains can be nonlinearly dependent on stress. For this reason, this section describes the nonlinear

elastic response of DEAs for large deformations using two equivalent descriptions, the Newtonian and energy method.

The Newtonian approach uses the partial differential equations of mechanical and electrostatic equilibriums together with the problem-specific equations for the boundary conditions, while the energy method uses the principle of least action applied to the Lagrangian of the entire system, including the power supply. The following introduces these two approaches for quasi-static actuations and applies them to three types of actuators. First, actuations of equibiaxial and uniaxial actuators are analyzed using the Newtonian approach. Equibiaxial actuators are allowed to deform equally in both lateral directions and were used to discuss the physical basis of DEAs in Sec. II, while uniaxial actuators are constrained from deformation in one of the lateral directions. Analysis of these two actuation types is particularly insightful because most designs of dielectric elastomer actuators locally behave as equibiaxial or uniaxial actuators, and these analyses lead to very useful dimensionless groups and the scaling relations between the applied voltage, actuation displacements, and forces. Second, the energy method is used to analyze the actuations of the dielectric elastomer actuators with finite-thickness electrodes and bilayer bending actuators. The analysis of actuators with finite-thickness electrodes is helpful to understand the importance of soft and thin electrodes, and the analysis of bilayer bending actuators gives insight into the out-of-plane actuation deformations of dielectric elastomer actuators. The description for the more complex, shape-morphing dielectric elastomer actuators is given in Sec. VII together with a finite element formulation and codes for their analysis.

A. The Newtonian approach

The Newtonian approach describes the actuations of DEAs using the two governing partial differential equations in the bulk for the mechanical and electrostatic equilibriums, together with the problem-specific boundary condition equations. The quasi-static mechanical equilibrium is essentially Newton's second law of motion applied to infinitesimal elements, resulting in a partial differential equation of the balance between the Cauchy stress tensor, $\boldsymbol{\sigma}$, and the electrostatic contributions. The electrostatic forces can be written either in terms of the electrostatic body forces, $\vec{b}$, or, as is more commonly practiced, in terms of their equivalent stress tensor, often called the Maxwell stress tensor, $\boldsymbol{\sigma}^{\text{Maxwell}}$,

$$\frac{\partial \sigma_{ij}}{\partial x_i} + b_j = 0, \quad \text{or} \quad \frac{\partial}{\partial x_i}\left(\sigma_{ij} + \sigma_{ij}^{\text{Maxwell}}\right) = 0, \quad \text{for } j = 1, 2, 3. \tag{4}$$

(Einstein summation convention is used.) The Cauchy stress tensor is a function of the elastomer deformation through an appropriate constitutive material model. For elastomers under large deformations, these models are often expressed in terms of the Helmholtz free energy, ψ, as a function of the Cauchy–Green deformation tensors. The right and left Cauchy–Green deformation tensors are defined as $\boldsymbol{C} = \boldsymbol{F}^T\boldsymbol{F}$ and $\boldsymbol{B} = \boldsymbol{F}\boldsymbol{F}^T$, respectively, where $\boldsymbol{F}$ is the deformation gradient tensor $F_{ij} = \partial x_i/\partial X_j$ and X_i and $x_i(X_1, X_2, X_3)$ are the initial and current spatial coordinates, respectively. $x_i(X_1, X_2, X_3)$ is also called the deformation mapping function. Considering only the mechanical forces in an isothermal and reversible process, the rate of change in Helmholtz free energy is equal to the mechanical work done on the system, i.e., $\dot{\psi} = \boldsymbol{P}:\dot{\boldsymbol{C}}$, where $\boldsymbol{P}$ is the first Piola–Kirchhoff stress tensor defined as the force in the current coordinate system per infinitesimal surfaces in initial coordinate system. (The dots over variables denote time derivatives.) The first Piola–Kirchhoff stress tensor is related to the Cauchy stress tensor through $\boldsymbol{P} = \frac{J}{2}\boldsymbol{F}^{-1}\boldsymbol{\sigma}\boldsymbol{F}^{-T}$, where J is the Jacobian of $\boldsymbol{F}$ and describes the ratio of the current volume to its initial volume. The Helmholtz free energy can then be written in terms of the Cauchy stress tensor as $\dot{\psi} = \left(\frac{J}{2}\boldsymbol{F}^{-1}\boldsymbol{\sigma}\boldsymbol{F}^{-T}\right):\dot{\boldsymbol{C}}$. Since the Helmholtz free energy is a function of the right Cauchy–Green deformation tensor, $\psi = \psi(\boldsymbol{C})$, its change can be expressed as $\dot{\psi} = \frac{\partial \psi}{\partial \boldsymbol{C}}:\dot{\boldsymbol{C}}$, which gives $\frac{J}{2}\boldsymbol{F}^{-1}\boldsymbol{\sigma}\boldsymbol{F}^{-T} = \frac{\partial \psi}{\partial \boldsymbol{C}}$ or

$$\boldsymbol{\sigma} = \frac{2}{J}\boldsymbol{F}\frac{\partial \psi}{\partial \boldsymbol{C}}\boldsymbol{F}^T. \tag{5}$$

Some of the most common constitutive mechanical models express the Helmholtz free energy in terms of the invariants of the Cauchy–Green deformation tensors, $\psi(I_1, I_2, I_3)$, where the invariants are

$$\begin{aligned} I_1 &= \text{tr}(\boldsymbol{C}) = \text{tr}(\boldsymbol{B}) = \lambda_1^2 + \lambda_2^2 + \lambda_3^2, \\ I_2 &= \frac{1}{2}((\text{tr}(\boldsymbol{C}))^2 - \text{tr}(\boldsymbol{C}^2)) = \frac{1}{2}((\text{tr}(\boldsymbol{B}))^2 - \text{tr}(\boldsymbol{B}^2)) = \lambda_1^2\lambda_2^2 + \lambda_1^2\lambda_3^2 + \lambda_2^2\lambda_3^2, \\ I_3 &= J^2 = \det(\boldsymbol{C}) = \det(\boldsymbol{B}) = \lambda_1^2\lambda_2^2\lambda_3^2, \end{aligned} \tag{6}$$

where λ_1, λ_2, and λ_3 are the first, second, and third principal stretches, respectively, defined as the current length per initial length in three orthogonal principal directions. For instance, the third principal stretch in Fig. 3(a) is along the thickness direction and are $\lambda_3 = t_1/t_0$ and $\lambda_3 = t_2/t_0$.

For material models that define the Helmholtz free energy as a function of the invariants of the Cauchy–Green deformation tensors, the Cauchy stress tensor becomes

$$\begin{aligned} \boldsymbol{\sigma} &= \frac{2}{J}\boldsymbol{F}\left(\frac{\partial \psi}{\partial I_1}\frac{\partial I_1}{\partial \boldsymbol{C}} + \frac{\partial \psi}{\partial I_2}\frac{\partial I_2}{\partial \boldsymbol{C}} + \frac{\partial \psi}{\partial I_3}\frac{\partial I_3}{\partial \boldsymbol{C}}\right)\boldsymbol{F}^T \\ &= \left(-\frac{2}{J}\frac{\partial \psi}{\partial I_2}\right)\boldsymbol{B}^2 + \left(\frac{2}{J}\frac{\partial \psi}{\partial I_1} + \frac{2}{J}\frac{\partial \psi}{\partial I_2}I_1\right)\boldsymbol{B} + \left(\frac{2}{J}\frac{\partial \psi}{\partial I_3}I_3\right)\boldsymbol{I}, \end{aligned} \tag{7}$$

where for the derivation of the invariants of the Cauchy–Green deformation tensors with respect to the tensor itself, $\partial \text{tr}(\boldsymbol{C})/\partial \boldsymbol{C} = \boldsymbol{I}$, $\partial \text{tr}(\boldsymbol{C}^2)/\partial \boldsymbol{C} = \boldsymbol{C}^T$, and $\partial \det(\boldsymbol{C})/\partial \boldsymbol{C} = \det(\boldsymbol{C})\boldsymbol{C}^{-T}$ are used.

It is often more convenient to express the Helmholtz free energy as the sum of the deviatoric contributions due to the material distortions and volumetric contributions due to the material volume compressions and expansions, $\psi(I_1, I_2, I_3) = \psi_{\text{dev}}(I_1, I_2) + \psi_{\text{vol}}(I_3)$. For the deviatoric contributions, two commonly used hyperelastic material models for dielectric elastomers are the incompressible neo-Hookean and Gent models. The neo-Hookean model is the simplest hyperelastic continuum material model that describes the Helmholtz free energy of the elastomer as a linear function of the first invariant of the Cauchy–Green deformation tensor and is suitable for stretches before any strain stiffening occurs. For the larger deformations, where the polymer chains are stretched nearly to their fully extended length, the Gent material model[31] is used since it

captures the strain-stiffening behavior of the elastomers using a simple empirical equation. The Helmholtz free energy equation for the incompressible neo-Hookean and Gent material models are $\psi_{\text{dev}}(I_1) = \frac{\mu}{2}(I_1 - 3)$ and $\psi_{\text{dev}}(I_1) = -\frac{\mu J_m}{2}\ln\left(1 - \frac{I_1 - 3}{J_m}\right)$, respectively, where μ is the shear modulus of the material and $J_m = I_m - 3$ defines the strain stiffening limit of $I_1 - 3$. For the volumetric contributions of the Helmholtz free energy, $\psi_{\text{vol}}(I_3) = \frac{\kappa}{2}(J-1)^2$ is often used, in which κ is the bulk modulus.

The Helmholtz free energy equations of any material model need to satisfy two conditions:[32] one is that in the absence of any deformations the Helmholtz free energy should, by convention, be zero, namely, $\psi(3, 3, 1) = 0$, and the other is that the Cauchy stresses when there are no deformations should be zero, i.e., $\boldsymbol{\sigma} = 0$ when $\boldsymbol{B} = \boldsymbol{I}$, which gives $\partial\psi/\partial I_1 + 2\partial\psi/\partial I_2 + \partial\psi/\partial I_3 = 0$. The former is satisfied by material models. However, the latter is not automatically satisfied by either the original neo-Hookean or Gent formulations. For instance, for the neo-Hookean Helmholtz free energy, $\psi(I_1, I_3) = \frac{\mu}{2}(I_1 - 3) + \frac{\kappa}{2}(J-1)^2$, the Cauchy stress tensor becomes $\boldsymbol{\sigma} = \frac{\mu}{J}\boldsymbol{B} + \kappa(J-1)\boldsymbol{I}$, using Eq. (7), which is nonzero when $\boldsymbol{B} = \boldsymbol{I}$. There are two common ways to resolve this issue: one is to add extra terms, for instance, $-\mu \ln J$,[33] to the volumetric contribution ψ_{vol}. From a molecular point of view, this added term corresponds to the change in the distribution of the cross-links in space as the material deforms.[34] The other way is to use the deviatoric invariants of the Cauchy–Green deformation tensors, $\bar{I}_1 = I_1/I_3^{1/3}$ and $\bar{I}_2 = I_2/I_3^{2/3}$, and express the deviatoric Helmholtz free energies in terms of $\bar{I}_1$ and $\bar{I}_2$ instead of I_1 and I_2. It is straightforward to show that $\psi_{\text{dev}} = \psi_{\text{dev}}(\bar{I}_1, \bar{I}_2)$ automatically satisfies $\partial\psi/\partial I_1 + 2\partial\psi/\partial I_2 + \partial\psi/\partial I_3 = 0$ regardless of the material model that is chosen for $\psi_{\text{dev}}(\bar{I}_1, \bar{I}_2)$. The volumetric contribution still needs to satisfy $\partial\psi_{vol}/\partial I_3 = 0$ at $I_3 = 1$, which is the case for $\psi_{\text{vol}}(J) = \frac{\kappa}{2}(J-1)^2$. In addition, the volumetric part is required to satisfy $\psi_{\text{vol}} \to +\infty$ when $J \to +\infty$ and $\psi_{\text{vol}} \to +\infty$ when $J \to 0$; the second condition is not satisfied by $\psi_{\text{vol}}(J) = \frac{\kappa}{2}(J-1)^2$; however, since dielectric elastomer materials are nearly incompressible, this model for volumetric contributions to the Helmholtz free energy remains a good approximation near $J \to 1$.

Using the deviatoric invariants of the Cauchy–Green deformation tensors, the Cauchy stress tensor for $\psi = \psi_{\text{dev}}(\bar{I}_1, \bar{I}_2) + \psi_{\text{vol}}(J)$ becomes

$$\boldsymbol{\sigma} = \left(-\frac{2}{J^{7/3}}\frac{\partial\psi_{\text{dev}}}{\partial\bar{I}_2}\right)\boldsymbol{B}^2 + \left(\frac{2}{J^{5/3}}\frac{\partial\psi_{\text{dev}}}{\partial\bar{I}_1} + \frac{2}{J^{5/3}}\frac{\partial\psi_{\text{dev}}}{\partial\bar{I}_2}\bar{I}_1\right)\boldsymbol{B} + \left(-\frac{2}{3J}\bar{I}_1\frac{\partial\psi_{\text{dev}}}{\partial\bar{I}_1} - \frac{4}{3J}\bar{I}_2\frac{\partial\psi_{\text{dev}}}{\partial\bar{I}_2} + 2J\frac{\partial\psi_{\text{vol}}}{\partial I_3}\right)\boldsymbol{I}. \tag{8}$$

Therefore, the neo-Hookean Helmholtz free energy in terms of the deviatoric invariants and its Cauchy stress tensor are, respectively,

$$\psi(\bar{I}_1, J) = \frac{\mu}{2}(\bar{I}_1 - 3) + \frac{\kappa}{2}(J-1)^2,$$
$$\boldsymbol{\sigma} = \left(\frac{\mu}{J^{5/3}}\right)\boldsymbol{B} + \left(-\frac{\mu}{3J}\bar{I}_1 + \kappa(J-1)\right)\boldsymbol{I}. \tag{9}$$

In addition, the Gent Helmholtz free energy in terms of the deviatoric invariants and its Cauchy stress tensor are, respectively,

$$\psi(\bar{I}_1, J) = -\frac{\mu J_m}{2}\ln\left(1 - \frac{\bar{I}_1 - 3}{J_m}\right) + \frac{\kappa}{2}(J-1)^2, \quad \boldsymbol{\sigma} = \frac{\mu}{J^{5/3}(1 - (\bar{I}_1 - 3)/J_m)}\boldsymbol{B} + \left(-\frac{\mu}{3J(1 - (\bar{I}_1 - 3)/J_m)}\bar{I}_1 + \kappa(J-1)\right)\boldsymbol{I}. \tag{10}$$

As the material is stretched to its limit, $I_1 - 3 \to J_m$, the Cauchy stress increases very sharply, $\boldsymbol{\sigma} \to \infty$, and when the stretch is small, $I_1 - 3 \ll J_m$, the Cauchy stress from the Gent model is similar to that of the neo-Hookean model. For the nearly incompressible elastomers, the bulk modulus is much larger than the shear modulus, $\mu \ll \kappa$; for the limit where $\kappa/\mu \to \infty$, the finiteness of $\kappa(J-1)$ term in Cauchy stress tensor gives $J \to 1$.

The other term in the balance of momentum is the Maxwell stress tensor. The equivalence of the two equations in Eq. (4) indicates that the Maxwell stress tensor needs to satisfy $\partial\sigma_{ij}^{\text{Maxwell}}/\partial x_i = b_j$. The electrostatic body forces arise from the interaction of the density of free charges, ρ_f, and the electric field, $\vec{E}$, given by $b_j = \rho_f E_j$. In turn, the density of free charges is related to the electric displacement field, $\vec{D}$, through $\rho_f = \partial D_i/\partial x_i$. By definition, the electric displacement is the sum of the electric field scaled by the vacuum electric permittivity and the polarization density of the dielectric, $\vec{D} = \epsilon_o\vec{E} + \vec{P}$. The relation between the electric field and the electric displacement is defined through the electrostatic constitutive model of the material. Often the material polarization under an applied electric field is proportional to the field, $\vec{P} \propto \vec{E}$. For such liquid-like dielectrics, the electric displacement, $\vec{D} = \epsilon_o\vec{E} + \vec{P}$, is also proportional to the applied electric field with the material permittivity, $\epsilon = \epsilon_0\epsilon_r$ (ϵ_r being the dielectric constant of material), as the proportionality constant, $\vec{D} = \epsilon\vec{E}$. The electrostatic Maxwell stresses is

$$\begin{aligned}\frac{\partial}{\partial x_i}\sigma_{ij}^{\text{Maxwell}} &= b_j = \rho_f E_j = \frac{\partial D_i}{\partial x_i}E_j = \frac{\partial}{\partial x_i}(\epsilon E_i E_j) - \epsilon E_i\frac{\partial E_j}{\partial x_i} \\ &= \frac{\partial}{\partial x_i}(\epsilon E_i E_j) - \epsilon E_i\frac{\partial E_i}{\partial x_j}\frac{\partial}{\partial x_i}(\epsilon E_i E_j) - \epsilon\delta_{ij}E_k\frac{\partial E_k}{\partial x_i} \\ &= \frac{\partial}{\partial x_i}\left(\epsilon E_i E_j - \frac{1}{2}\epsilon\delta_{ij}E_k E_k\right).\end{aligned} \tag{11}$$

In deriving this expression, the electrostatic Maxwell–Faraday equation, curl $\vec{E} = 0 \to \partial E_j/\partial x_i = \partial E_i/\partial x_j$, is used and it is assumed that the permittivity does not change with position in the dielectric, $\partial\epsilon/\partial x_i = 0$. Equation (11) is satisfied when

$$\sigma_{ij}^{\text{Maxwell}} = \epsilon\left(E_i E_j - \frac{1}{2}\delta_{ij}E_k E_k\right). \tag{12}$$

Equation (4) described the mechanical equilibrium inside the elastomer. The other governing equation for the analysis of DEAs using the Newtonian approach is the Poisson's equation for electric

potential, ϕ, describing electrostatic equilibrium,

$$\frac{\partial^2 \phi}{\partial x_i \partial x_i} = \frac{\rho}{\epsilon_0}, \quad \text{or} \quad \frac{\partial D_i}{\partial x_i} = \rho_f, \tag{13}$$

in which ρ and ρ_f are the volume density of total and free charges, respectively. Poisson's equation is essentially Gauss's flux theorem applied to Coulomb's law, $\vec{F}_1 = (k_e e_1 e_2 / r_{21}^2)\vec{r}_{21}/r_{21}$, with $\vec{E} = \vec{F}_1/e_1$ as the definition of the electric field and $E_i = \partial\phi/\partial x_i$ as the definition of the electric potential.

Finally, at the outer and internal boundary surfaces, the Dirichlet and Neumann boundary conditions for the mechanical equilibrium prescribe the displacements and stresses, respectively, and, for the electrostatic equilibrium, prescribe the electric potentials and electric fields, respectively,

$$\begin{aligned} \vec{x}(\vec{X}) &= \vec{x}_0(\vec{X}), \ \forall \vec{X} \in S_u, \\ \vec{n}(\vec{X}) \cdot \boldsymbol{\sigma}(\vec{X}) &= \vec{n}(\vec{X}) \cdot \boldsymbol{\sigma_0}(\vec{X}), \quad \forall \vec{X} \in S_\sigma, \\ \phi(\vec{X}) &= \phi_0(\vec{X}), \ \forall \vec{X} \in S_\phi, \\ \vec{E}(\vec{X}) &= \vec{E}_0(\vec{X}), \ \forall \vec{X} \in S_D, \end{aligned} \tag{14}$$

in which $\vec{x}_0$, $\boldsymbol{\sigma}_0$, ϕ_0, and $\vec{E}_0$ are the prescribed displacements, stresses, electric potentials, and electric fields, respectively, specified over the boundary surfaces S_u, S_σ, S_ϕ, and S_D. $\vec{n}(\vec{X})$ is the normal vector field to the S_σ boundary. The boundary condition equations are problem-specific, having a different form for any different problems.

B. Equibiaxial DEAs analysis using the Newtonian approach

A simple equibiaxial DEA, subjected to electric potential ϕ_0 and through-thickness and lateral stresses f_T and f_L, is shown in Fig. 4(a). f_T and f_L, which are parallel and normal to the electric field vectors, respectively, account for any external forces that are applied to the DEA (and in reaction is applied by the DEA). For instance, for a prestretched elastomer, f_L, represents the force per unit area exerted by a stretching frame, or f_T in the context of the artificial muscles shown in Fig. 2(b) is the actuation force per unit area that bends the elbow. By convention, the directions of $\vec{f}_T$ and $\vec{f}_L$ in Fig. 4 point outward so that positive applied stresses, f_T or f_L, lead to tensile internal stresses.

Neglecting the edge effects, the electric field can be assumed to be normal to the electrodes, $\vec{E} = (0, 0, E)$. Consequently, Poisson's equation with zero density of charges inside the elastomer, $\rho = 0$, combined with the electrostatic boundary conditions, $\phi(x_3 = 0) = 0$ and $\phi(x_3 = t) = \phi_0$, lead to $\phi = x_3\phi_0/t$ and, therefore, $E = \phi_0/t$.

When the external stresses in the two lateral directions, x_1 and x_2, are equal, an equibiaxial and homogeneous actuations is produced when a voltage ϕ_0 is applied. The mapping function has the following mathematical form:

$$x_1 = \lambda_1 X_1, \ x_2 = \lambda_2 X_2, \ x_3 = \lambda_3 X_3. \tag{15}$$

The homogeneity of actuation means that λ_1, λ_2, and λ_3 are independent of the spatial position and the equibiaxial actuation means that $\lambda_1 = \lambda_2$. For this mapping function, the deformation gradient tensor and the left Cauchy–Green deformation tensor are

$$\boldsymbol{F} = \left[\frac{\partial x_i}{\partial X_j}\right] = \begin{bmatrix} \lambda_1 & 0 & 0 \\ 0 & \lambda_1 & 0 \\ 0 & 0 & \lambda_3 \end{bmatrix}, \quad \boldsymbol{B} = FF^T = \begin{bmatrix} \lambda_1^2 & 0 & 0 \\ 0 & \lambda_1^2 & 0 \\ 0 & 0 & \lambda_3^2 \end{bmatrix}. \tag{16}$$

Using the neo-Hookean material model [Eq. (9)], the Cauchy stress tensor becomes

$$\boldsymbol{\sigma} = \begin{bmatrix} \frac{\mu}{J^{5/3}}\lambda_1^2 - \frac{\mu}{3J}\bar{I}_1 + \kappa(J-1) & 0 & 0 \\ 0 & \frac{\mu}{J^{5/3}}\lambda_1^2 - \frac{\mu}{3J}\bar{I}_1 + \kappa(J-1) & 0 \\ 0 & 0 & \frac{\mu}{J^{5/3}}\lambda_3^2 - \frac{\mu}{3J}\bar{I}_1 + \kappa(J-1) \end{bmatrix}. \tag{17}$$

Since none of the terms in the Cauchy and Maxwell stress tensors depend on spatial position, due to the homogeneity of the deformation, the equation of balance of momenta [Eq. (4)] results in nothing but $0 = 0$. This simply represents the fact that any homogeneous deformation automatically satisfies the partial differential equation of mechanical equilibrium. The only set of equations that then remain to be satisfied are the mechanical boundary conditions on the faces of the actuator, six in Fig. 4. The boundary conditions on the four vertical sides of the actuator are equivalent and the equations for the top and bottom surfaces are both equivalent as well, and so the six boundary conditions reduce to two, e.g., for the surfaces with (1, 0, 0) and (0, 0, 1) outward normals at the right side and the top of the actuator,

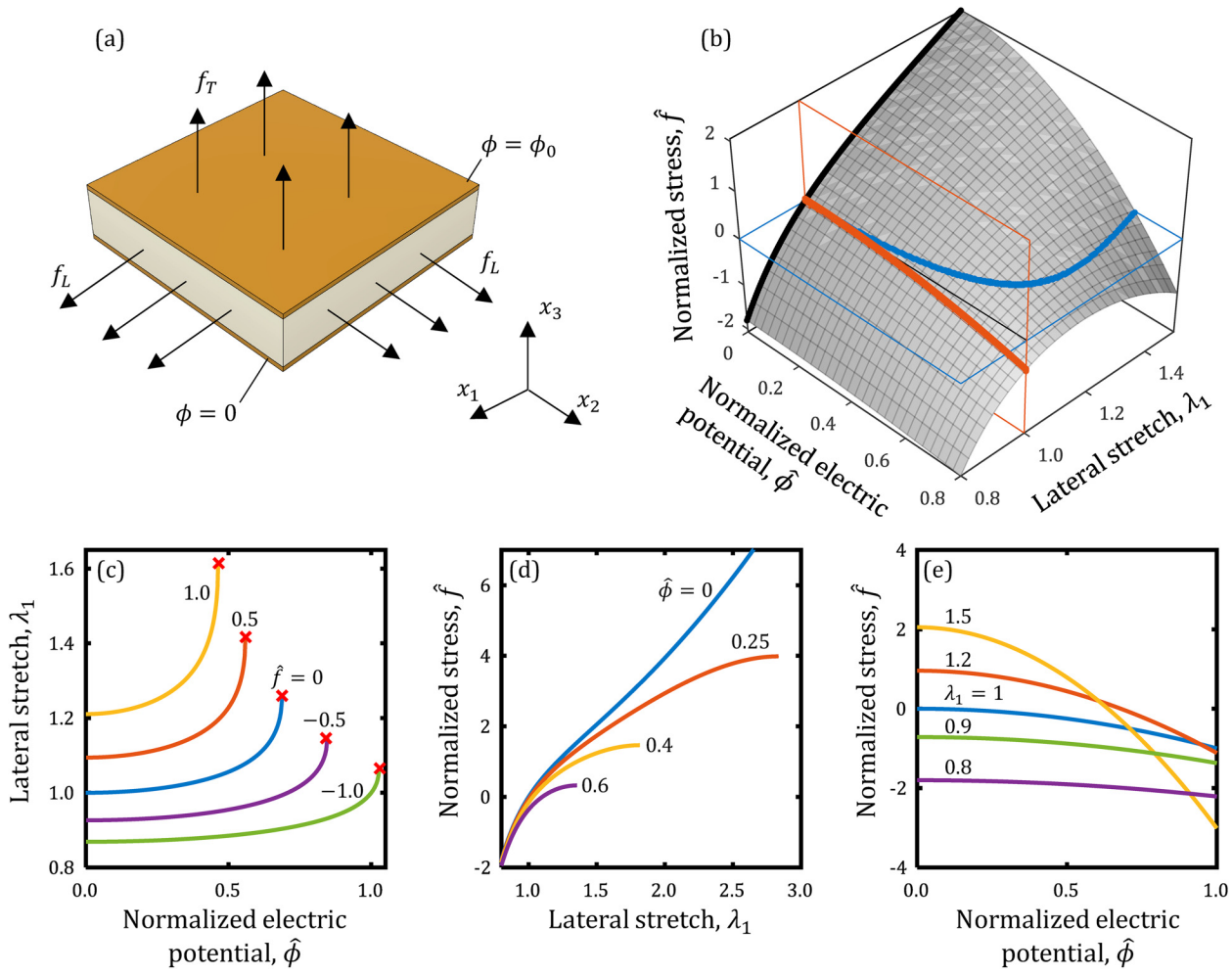

FIG. 4. Characterization of electrostatic actuations of equibiaxial DEAs. (a) Free-body diagram of an equibiaxial dielectric elastomer actuator that consists of a dielectric elastomer layer sandwiched between two compliant electrodes, to which electric potentials of $\phi = 0$ and $\phi = \phi_0$ are applied. The through-thickness and lateral stresses f_T and f_L are any external stresses applied to the DEA along the thickness x_3 and lateral x_1/x_2 directions, respectively. The changes in these two stresses as the voltage is being applied represent the voltage-induced actuation forces. The directions for f_T and f_L are chosen conventionally to point outward such that a positive applied stress leads to tensile internal stresses. (b) The three-dimensional representation of the non-dimensional actuation stress, $\hat{f} = (f_L - f_T)/\mu$, vs the non-dimensional electric potential, $\hat{\phi} = \sqrt{\epsilon/\mu}\phi_0/t_0$, and lateral stretch, λ_1, of the equibiaxial DEA expressed by Eq. (21). Also shown are the curves for the blocking force (red curve) and actuation stretch under no external forces (blue curve). μ, ϵ, and t_0 are the elastomer's shear modulus, electrical permittivity, and initial thickness, respectively. The lateral stretch, λ_1, is the ratio of lateral length (or width) of the elastomer layer after actuation to its initial length (or initial width) under zero voltages and zero forces. (c) Lateral stretch of the DEA increases gradually at low normalized electric potentials, followed by large increase that at some critical point, indicated by the red crosses, leads to electromechanical instability at which no further applied voltage is required to increase the stretch. The abrupt thinning of the elastomer results in extreme electric fields that if they exceed the electrical breakdown strength of the dielectric causes electrical breakdown. Applying tensile lateral stresses or compressive transverse stresses results in larger actuation stretch at lower electric potentials. (d) The stress vs stretch decreases with the applied voltage and shows instabilities under any applied voltage at which no further increase in applied stress is required to stretch the elastomer further. (e) The actuation forces vs the electric potential show larger changes when the elastomer is stretched laterally.

$$(1, 0, 0) \cdot \boldsymbol{\sigma}(X_1 = L) = \vec{f}_L,$$
$$(0, 0, 1) \cdot \boldsymbol{\sigma}(X_3 = T) = \vec{f}_E + \vec{f}_T. \tag{18}$$

The changes in the two traction vectors $\vec{f}_L$ and $\vec{f}_T$ with applied voltage represent the voltage-induced actuation stresses. $\vec{f}_E$ is the electrostatic forces per surface area and is calculated from the surface density of free charges multiplied by the jump in electric field at the surface, $f_e = \rho_f[[E]] = -\rho_f E$. The surface density of free charges is equal to the jump in electric displacement, $\rho_f = [[D]] = \epsilon E$, which gives $f_E = -\epsilon\phi^2/t^2 = -\epsilon\phi^2/\lambda_3^2 t_0^2$, where t_0 is the initial thickness of the elastomer layer. Therefore, the actuation of the equibiaxial DEA can be described by

$$\frac{\mu}{J^{5/3}}\lambda_1^2 - \frac{\mu}{3J}\bar{I}_1 + \kappa(J-1) = f_L,$$
$$\frac{\mu}{J^{5/3}}\lambda_3^2 - \frac{\mu}{3J}\bar{I}_1 + \kappa(J-1) = -\frac{\epsilon\phi_0^2}{b^2T^2} + f_T. \tag{19}$$

For a compressible material, the two equations can be solved numerically for λ_1 and λ_3. However, for nearly incompressible materials, such as most elastomers, $\kappa/\mu \to \infty$, the change in volume is negligible, i.e., $J \to 1$ and therefore $\lambda_1^2\lambda_3 \to 1$. Subtracting the two equations in (19) and letting $J = 1$ and $\lambda_3 = 1/\lambda_1^2$ leads to a normalized actuation equation,

$$\lambda_1^2 - \lambda_1^{-4} = \frac{\epsilon\phi_0^2}{\mu t_0^2}\lambda_1^4 + \frac{f_L - f_T}{\mu}. \tag{20}$$

The dimensionless groups are the lateral stretch λ_1 (or thickness stretch $\lambda_3 = 1/\lambda_1^2$), normalized applied electric potential $\hat{\phi} = \sqrt{\epsilon/\mu}\phi_0/t_0$, and the normalized difference in the two stresses $\hat{f} = (f_L - f_T)/\mu$. A positive $\hat{f}$ corresponds to applied stresses that laterally stretch the elastomer layer, namely, tensile lateral stresses and/or compressive through-thickness stresses. The non-dimensional electric potential for a multilayer DEA with n elastomer layers and total thickness of t_0 becomes $\hat{\phi} = \sqrt{\epsilon/\mu}n\phi_0/t_0$. In terms of $\hat{\phi}$ and $\hat{f}$, the actuation equation becomes

$$\lambda_1^2 - \lambda_1^{-4} = \hat{\phi}^2\lambda_1^4 + \hat{f}. \tag{21}$$

Several important insights into the behavior of DEAs are revealed by this form of the actuation equation. For example, the actuation of an incompressible dielectric elastomer actuator is not directly a function of the through-thickness and lateral stresses, f_T and f_L, themselves but only their difference. Consequently, the actuations are independent of any external pressure, suggesting that DEAs have equal potential to be used in low pressure environments such as outer space and in high pressure environments such as in the ocean. Another insight is that a softer elastomer with smaller μ needs a lower voltage to actuate to the same stretch as a stiffer material, $\phi_0 \propto \sqrt{\mu}$; however, the magnitude of the actuation stresses $f_L - f_T$ will be proportionally lower, $(f_L - f_T) \propto \mu$. The exception being that the blocking stresses, defined when the deformation is completely confined, $\lambda_1 = \lambda_3 = 1$, are independent of the shear modulus and only depend on the applied voltage, permittivity, and thickness: $f_L - f_T = -\epsilon\phi_0^2/t_0^2$. For a higher permittivity elastomer, the voltage to actuate to the same stretch and forces is smaller than that of a low permittivity elastomer, $\phi_0 \propto \epsilon^{-1/2}$. Therefore, increasing permittivity is one possible route to higher performance DEAs with the caveat that the electrical breakdown strength needs to be maintained.

Figure 4(b) is a plot of the equibiaxial actuation equation [Eq. (21)] in which the non-dimensional actuation stresses are plotted as a function of the normalized electric potential and the lateral stretch. The lateral stretch as a function of the normalized applied voltage, for different constant normalized stresses, is plotted in Fig. 4(c) showing that the increase in lateral stretch is larger at higher applied voltage, and at some critical points, shown with red crosses in Fig. 4(c), the increase in lateral stretch becomes so steep that no further applied voltage is needed to further actuate the elastomer; this is the electromechanical instability referred to previously.[4,5,29] Mathematically, the electromechanical instability when no stresses are applied, $\hat{f} = 0$, occurs when $d\hat{\phi}/d\lambda_1 = 0$, which occurs at $\lambda_1 = 1.26$ for which the stretch in thickness direction is $\lambda_3 = 0.63$ and the normalized electric field is $\hat{E} = 0.687$.

Important for the design of equibiaxial dielectric elastomer devices is that the electromechanical instability point depends on the normalized stresses: a tensile lateral stress (or compressive through-thickness stresses) shifts the instability point to a lower normalized electric potential; however, the possible actuation before the onset of the instability will be larger than the case where the elastomer is not stretched, even when the material shows no stress stiffening effects. For example, when $\hat{f} = 1$, the actuation stretch before the instability is about $\lambda_1(\hat{\phi} = \hat{\phi}_c)/\lambda_1(\hat{\phi} = 0) \cong 1.61/1.21 = 1.33$, which is significantly larger than $\lambda_1 = 1.26$ for $\hat{f} = 0$. On the other hand, when the dielectric elastomer is pressed laterally (or stretched in the thickness direction), the instability occurs at higher normalized electric potentials but the actuation stretch at the instability is smaller; for example, when $\hat{f} = -1$, the actuation stretch is about $\lambda_1(\hat{\phi} = \hat{\phi}_c)/\lambda_1(\hat{\phi} = 0) \cong 1.06/0.87 = 1.22$, which is slightly smaller than the case where $\hat{f} = 0$. These considerations indicate that the maximum output work, prior to electromechanical instability, increases with the normalized stresses, $\hat{f}$. Also, it suggests that when comparing the maximum actuation of actuators made of different materials, it is necessary that the actuation stresses must be the same.

Applying an electric potential also changes the stress–stretch characteristics of the DEA as shown in Fig. 4(d). In the absence of voltage, the externally applied stress increases monotonically with the stretch, whereas applying a voltage lowers the stress and makes the curve non-monotonic. There are also conditions, under an applied voltage, at which the slope of the stress–stretch curves is zero at which the elastomer can be continuously stretched.

The non-dimensional actuation stresses as a function of non-dimensional electric potential and different constant stretches are shown in Fig. 4(e). Stretching the elastomer reduces the thickness of the elastomer and results in larger changes of the actuation forces with applied electric potentials. The relation between the actuation forces and electric potentials is monotonic when the elastomer is held at a constant stretch. The blocking force in Fig. 4(e) is labeled $\lambda_1 = 1$.

Of particular interest is when the DEA operates under constant external loads, for which the stresses could be replaced by $f_T = F_T/l^2 = F_T/\lambda_1^2 l_0^2$ and $f_L = F_L/lt = F_L/\lambda_1\lambda_3 L t_0$, leading to the following actuation equation. l and l_0 are the initial and actuated width (and length) of the DEA, respectively.

$$\lambda_1^2 - \lambda_1^{-4} = \hat{\phi}^2\lambda_1^4 + \hat{F}_L\lambda_1 - \hat{F}_T\lambda_1^{-2}, \tag{22}$$

where $\hat{F}_L = F_L/\mu LT$ and $\hat{F}_T = F_T/\mu L^2$ are the normalized lateral and through-thickness stresses, when the applied loads are constant.

The onset of electromechanical instability of the equibiaxial DEAs, shown by the red crosses in Fig. 4(c), can be suppressed if the elastomer undergoes strain stiffening before the electromechanical instability point.[29] Rederiving the actuation equation for the equibiaxial dielectric elastomer actuators using the Gent model gives

$$\frac{\lambda_1^2-\lambda_1^{-4}}{1-(2\lambda_1+\lambda_1^2-3)/J_m}=\hat{\phi}^2\lambda_1^4+\hat{f}. \tag{23}$$

The effect of strain stiffening is illustrated in Fig. 5(a) for a strain-stiffening parameter of $J_m=15$, corresponding to a maximum stretch of $\lambda_1=3.0$ in equibiaxial actuation. The electromechanical instability leads to a snap-through, shown by the vertical dashed lines in Fig. 5(a), corresponding to drastic decrease in thickness, t, and increase in electric fields, $E=\phi/t$. Prestretching can prevent the electromechanical instability. The prestretch required depends on the J_m parameter of the material, as shown in Fig. 5(b). As mentioned in Sec. I, prestretching the elastomer was one of the early breakthroughs in dielectric elastomer actuators that allowed unprecedented large area actuations,[2] even though at the time the underlying reason was not well understood.

It should be emphasized that the electromechanical instability is not intrinsically a failure mechanism since it only describes a snap-through instability to a smaller thickness. Whether the snap-through results in failure or not depends on the electrical breakdown strength of the material. In the context of Fig. 5(a), the DEA fails when the actuation curve of the DEA intersects with the electrical breakdown curve of the dielectric (the red curves). Several scenarios are indicated in this figure; the elastomer is prestretched to different extents and a variety of electrical breakdown strengths are assumed for the dielectric. When the non-dimensional electrical breakdown strength, $\hat{E}_b=\sqrt{\epsilon/\mu}E_b$, is small, e.g., $\hat{E}_b<1$, the electrical breakdown occurs before the electromechanical instability, for $J_m=15$; avoiding the electromechanical instability is irrelevant. For larger electrical breakdown strengths, e.g., $\hat{E}_b=2$, the snap-through of the material leads to electrical breakdown and hence failure of the actuator, shown with the red crosses in Fig. 5(a). In this case, significantly larger actuation stretches can be achieved if the elastomer is prestretched to the extent where the stretch vs electric potential becomes monotonic and the electromechanical instability is avoided. For very large electrical breakdown strength, e.g., $\hat{E}_b=10$, the electromechanical instability does not cause any electrical breakdown and instead the snap-through could be employed for large actuations and possibly novel devices at small electric potential increments near the instability point.

Significantly, as shown in Fig. 5(c), the electromechanical instability can also be avoided without any prestretch, if the dielectric elastomer material is engineered such that its strain stiffening occurs at $J_m<7.3$, which corresponds to $\lambda_1=2.26$ for equibiaxial actuation: in other words, the theoretical maximum actuation stretch of a non-prestretched equibiaxial actuator before the electromechanical instability is $\lambda_1=2.26$, provided that the material deformation follows the Gent model. In experiment, actuation stretches close to this theoretical limit has been achieved; for example, the interpenetrating polymer networks[35] within VHB elastomers are used to tune the strain-stiffening parameter and actuation area strain of 233% has been achieved, which corresponds to $\lambda_1=1.82$.

In closing this discussion on the electromechanical instability analysis of the equibiaxial DEAs, it has been assumed that actuation is homogeneous and, therefore, the possibility of local instabilities was neglected. Inhomogeneities will invariably cause local instabilities to occur at lower electric fields for which the analysis is more involved.[36,37] DEAs can also form wrinkling patterns when their actuation is confined, for instance, by a frame. A rich pattern of wrinkling geometries has been studied and the interested readers are referred to Refs. 38–41.

C. Uniaxial DEA analysis using the Newtonian approach

By incorporating arrays of parallel fibers or strips that have a very high stiffness compared to that of the elastomer, the biaxial actuation can be converted into a uniaxial actuation. For instance, when the fibers are arranged parallel to the x_2 direction [Fig. 6(a)], the actuation in the x_2 direction is constrained, $\lambda_2=1$, and the actuator can only expand along x_1 while contracting in thickness. The deformation mapping function is then

$$x_1=\lambda_1X_1,\ x_2=X_2,\ x_3=\lambda_3X_3. \tag{24}$$

Following the same procedure as for the equibiaxial actuators, i.e., using the mapping function to calculate the deformation gradient tensor, the right Cauchy–Green deformation tensor, and the Cauchy stress tensor from the neo-Hookean material model, we get

$$\boldsymbol{\sigma}=\begin{bmatrix}\frac{\mu}{J^{5/3}}\lambda_1^2-\frac{\mu}{3J}\bar{I}_1+\kappa(J-1) & 0 & 0\\ 0 & \frac{\mu}{J^{5/3}}-\frac{\mu}{3J}\bar{I}_1+\kappa(J-1) & 0\\ 0 & 0 & \frac{\mu}{J^{5/3}}\lambda_3^2-\frac{\mu}{3J}\bar{I}_1+\kappa(J-1)\end{bmatrix}. \tag{25}$$

Once again, since the deformation is homogeneous, the partial differential equation of the mechanical equilibrium is automatically satisfied and leads to $0=0$ for any choice of stretches, λ_1 and λ_3. To evaluate the actual stretches, the boundary conditions are used

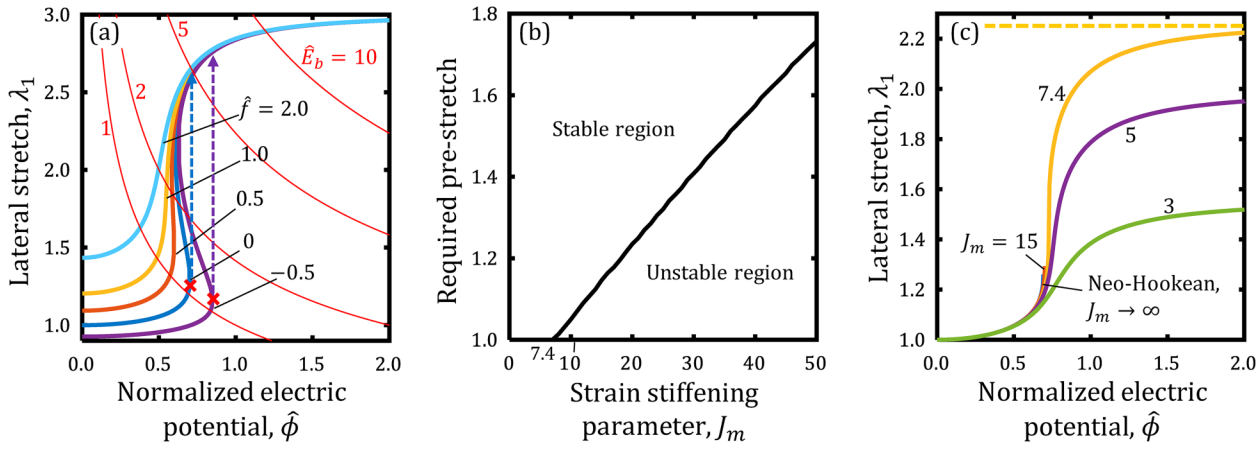

FIG. 5. Electromechanical instability can be prevented by prestretching the elastomer or designing the elastomer to exhibit certain strain-stiffening characteristics. (a) An example of lateral stretch as a function of the non-dimensional electric potential and at different prestretches. In this example, the strain stiffening is assumed to be $J_m = 15$. The electromechanical instability results in snap-through increase in lateral stretch shown by the vertical dashed lines. The thin red lines show four examples of the electrical breakdown strengths of the dielectric. (b) The required prestretch to avoid the electromechanical instability is a function of the strain-stiffening parameter of the elastomer. No prestretch is required when $J_m < 7.4$. (c) Lateral stretch as a function of the non-dimensional electric potential for elastomer materials with different strain-stiffening characteristics. The electromechanical instability can be prevented by designing the elastomer material such that $J_m < 7.4$, for which no prestretch is required.

resulting in

$$\begin{aligned} \frac{\mu}{J^{5/3}}\lambda_1^2 - \frac{\mu}{3J}\bar{I}_1 + \kappa(J-1) &= f_L, \\ \frac{\mu}{J^{5/3}}\lambda_3^2 - \frac{\mu}{3J}\bar{I}_1 + \kappa(J-1) &= -\frac{\epsilon\phi^2}{t^2} + f_T. \end{aligned} \tag{26}$$

Subtracting the two equations and assuming an incompressible material with $J \to 1$ and, therefore, $\lambda_3 = \lambda_1^{-1}$ results in the uniaxial actuation equation

$$\lambda_1^2 - \lambda_1^{-2} = \hat{\phi}^2\lambda_1^2 + \hat{f}. \tag{27}$$

Figure 6(b) shows the three-dimensional representation of the non-dimensional actuation forces as a function of the non-dimensional electric potential and the lateral stretch for uniaxial actuators. In contrast to the biaxial actuator (Fig. 4), the uniaxial DEA does not show any electromechanical instability [Fig. 6(c)], unless the DEA is under compressive lateral stress (or tensile through-thickness stress). The stress–stretch curve of the uniaxial DEA [Fig. 6(d)] softens when a voltage is applied, but there are no conditions corresponding to zero-stiffness. Also, comparing the graphs in Figs. 4(e) and 6(e), it can be seen that the change in non-dimensional forces with the applied voltage is larger when the elastomer is stretched laterally.

D. Energy methods for analysis of dielectric elastomer actuators

The energy approach can be a more straightforward analytical approach in some cases, such as when considering the effect of finite-thickness electrodes. In this approach, a mathematical form is assumed for the solution variables, similar to the procedure for the analytical solutions using the Newtonian method, and equilibrium is sought which minimizes the total potential energy of the system consisting of dielectric elastomer, the charging unit, and the mechanical loading. As with other energy methods used in physics, there is no assurance that the mathematical form assumed for the solution variables satisfies all the governing equations.

For a dielectric elastomer actuator consisting of dielectric elastomer layers with total initial thickness of t_{a0} and electrodes with total initial thickness of t_{p0}, undergoing homogeneous equibiaxial actuation, the strain energy is given by the Helmholtz free energy of the elastomer and electrode materials. Using the neo-Hookean elastomer model, the strain energy becomes $U_{\text{strain}} = \frac{\mu_a}{2}(I_1 - 3)l_0^2 t_{a0} + \frac{\mu_p}{2}(I_1 - 3)l_0^2 t_{p0}$, where μ_a and μ_p are the shear moduli of the elastomer and electrode materials, respectively, l_0 is the initial length and width of the actuator, and I_1 is the first invariant of the Cauchy–Green deformation tensor, which for equibiaxial actuation of incompressible elastomer becomes $I_1 = 2\lambda_1^2 + \lambda_1^{-4}$, assuming the same deformation mapping function as in equibiaxial DEAs [Eq. (15)]. The stored electrostatic energy in the elastomer dielectric is $U_{\text{electric}} = \epsilon E^2 l_0^2 t_{a0}/2 = \epsilon n^2\phi^2\lambda_1^4 l_0^2/2t_{a0}$. The change in the potential of the charging unit is $U_{\text{charger}} = -Q\phi = -C\phi^2 = -\epsilon n^2\phi^2\lambda_1^4 l_0^2/t_{a0}$, and therefore the total change in

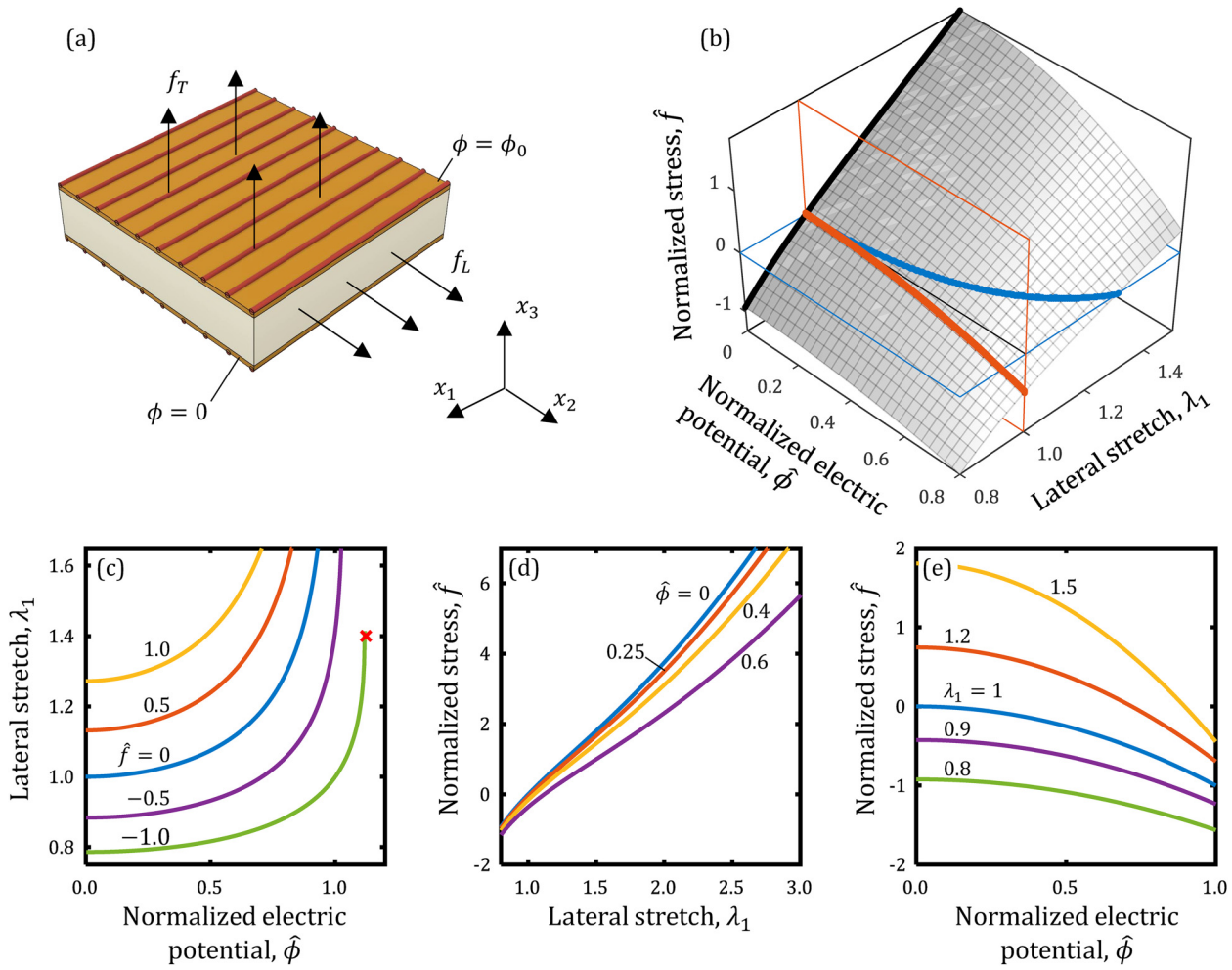

FIG. 6. Characterization of electrostatic actuations of uniaxial DEAs. (a) Adding parallel stiff fibers to an equibiaxial DEA constraints the deformation along the fibers, i.e., along x_2, and results in a uniaxial DEA, which in this example expands in the x_1 direction and contracts in thickness, x_3 direction, when actuated. (b) The three-dimensional representation of the non-dimensional actuation stress, $\hat{f} = (f_L - f_T)/\mu$, vs the non-dimensional electric potential, $\hat{\phi} = \sqrt{\epsilon/\mu}\phi_0/t_0$, and lateral stretch, λ_1, of the uniaxial DEA together with the curves for the blocking forces (red curve) and actuation stretches under no external forces (blue curve). (c) The lateral stretches of uniaxial DEAs increase monotonically with the non-dimensional electric potentials unless the actuator is subjected to compressive lateral forces (or tensile through-thickness forces). (d) The stress–stretch curve of the elastomer is lowered when the electric potential and its slope decreases, i.e., it softens; however, no zero-stiffness point is encountered. (e) The change in the actuation stress of the DEA as a function of electric potential is larger when the elastomer is stretched laterally, due to the decrease in its thickness. The blocking force, i.e., the actuation force when the deformation is completely confined, is annotated by $\lambda_1 = 1$.

electrostatic potential of the elastomer and the charging unit is $U_{\text{electric}} + U_{\text{charger}} = -\epsilon n^2\phi^2\lambda_1^4 l_0^2/2t_{a0}$. The work done by the external stresses f_L and f_T are $U_L = 2\int (f_L\lambda_1 l_0\lambda_3 t_0)(\lambda_1 - 1)l_0\, d\lambda_1 = 2(1 - \ln\lambda_1)f_L l_0^2 t_0$ and $U_T = \int (f_T\lambda_1^2 l_0^2)(\lambda_3 - 1)t_0\, d\lambda_3 = (1 + 2\ln\lambda_1)f_L l_0^2 t_0$, where $t_0 = t_{a0} + t_{p0}$. Therefore, the total potential energy due to the mechanical stresses is $U_{\text{mech}} = -(2(1 - \ln\lambda_1)f_L + (1 + 2\ln\lambda_1)f_T)l_0^2 t_0$. The total potential energy of the entire system can be written as

$$U = \frac{\mu_a}{2}(I_1 - 3)l_0^2 t_{a0} + \frac{\mu_p}{2}(I_1 - 3)l_0^2 t_{p0} - \frac{\epsilon n^2\phi^2\lambda_1^4 l_0^2}{2t_{a0}} - (2(1 - \ln\lambda_1)f_L + (1 + 2\ln\lambda_1)f_L)l_0^2 t_0. \quad (28)$$

The equilibrium is where the actuation results in minimum total potential energy, i.e., where $\partial U/\partial\lambda_1 = 0$ and $\partial^2 U/\partial\lambda_1^2 > 0$,

leading to the following equation for the homogeneous equibiaxial actuation of an incompressible dielectric elastomer with finite-thickness electrodes,

$$\lambda_1^2-\lambda_1^{-4}-\frac{\epsilon n^2\phi^2}{\mu_a t_{a0}^2(1+\mu_p t_{p0}/\mu_a t_{a0})}\lambda_1^4-\frac{(1+t_{P0}/t_{a0})}{(1+\mu_p t_{p0}/\mu_a t_{a0})}\frac{(f_L-f_T)}{\mu_a}=0. \tag{29}$$

This is the same as the actuation equation of equibiaxial DEAs with infinitesimally thin electrodes [Eq. (20)], except that the non-dimensional electric potential is scaled by $(1+\mu_p t_{p0}/\mu_a t_{a0})^{-1/2}$ and the non-dimensional actuation forces are scaled by $(1+t_{P0}/t_{a0})/(1+\mu_p t_{p0}/\mu_a t_{a0})$. Considering the actuation under no external stresses, the actuation stretch is maximized when the product of the electrode thickness and stiffness is minimized, demonstrating the importance of having compliant electrodes.

IV. DIELECTRIC ELASTOMERS

Elastomers consist of large molecular networks with low cross-linking densities and long polymer chains. The essential physics and the relationship between their molecular structure and properties have been well established and the reader is referred to textbooks on the subject[42,43] including liquid crystal elastomers.[44] In this section, we only include discussion of the major factors that directly affect an actuator response. Before doing so, it is important to emphasize that the elastomers used in DEAs to date have been commercially available materials, such as VHB films and Sylgard silicone elastomers, developed for very different applications, for instance as sealing or insulating compounds. Motivated by potential applications of DEAs, programs are now under way to develop elastomer compositions for DEA applications.[45–47]

A. Fabrication of thin layers of elastomer

Elastomer layers of DEAs are either manufactured sheets, such as 3M VHB™ acrylic films and ELASTOSIL® silicone films, or fabricated by polymerization of commercial precursors, such as Sylgard® silicones. As discussed in Secs. II and III, the actuation stretches and forces increase with the non-dimensional electric potential, $\hat{\phi}=\sqrt{\epsilon/\mu}n\phi_0/t_0$. So, to achieve large actuations at a given applied voltage ϕ_0, it is important to fabricate DEAs as multilayers with thicknesses t_0/n, often in the range of 10–50 μm. Handling such thin films individually and stacking them up can be tedious and difficult to exclude air bubbles. For this reason, high-performance multilayer DEAs are often made through layer-by-layer fabrication schemes, in which first a precursor is deposited onto a substrate and polymerized and then an electrode is formed onto the elastomer layer, as will be discussed in Sec. V, followed by forming another elastomer layer and repeating this process until the desired number of layers and total thickness are achieved.[27]

The precursors are viscous liquids containing the oligomers to form the backbones of the polymer chains, as well as catalysts, initiators, cross-linkers, plasticizers, and other additives. Based on their combination of low stiffness, permittivity, and electrical breakdown strength, the urethane and acrylate elastomers as well as silicone-based elastomers were identified as the suitable actuator materials.[48] Polymerization of the oligomers is initiated either by heating if a catalyst, such as Pt, is present or by exposure to light when a photo-initiator is used. The latter has the advantage of fast polymerization, tens of seconds as compared to tens of minutes for the thermal initiators, and has potential for spatial control of the polymerization, for instance using a laser, masking, or half-tone lithography.[49] Light with a wavelength corresponding to absorption bands of the photo-initiators, often in the ultraviolet, either causes homolytic cleavage for type I photo-initiators such as hydroxyacetophenone or hydrogen abstraction for type II photo-initiators such as benzophenone, which forms radicals that initiate the polymerization process. Catalysts such as platinum are often found in two-part thermally initiated precursors, such as Sylgard 184 silicones. The cross-linkers are chosen based on the side groups of the polymer chain or end groups of the oligomers. For instance, the polymer chain can be extended by using vinyl terminated oligomers with thiol 3-functional cross-linkers. Gel fraction is typically used as a measure of the effectiveness of the cross-linking. For more on the chemistry of silicone and acrylic-based elastomers for DEA applications, the interested reader is referred to recent articles.[47,50]

The most common methods to deposit the precursors are spin-coating[51,52] and doctor blading, also known as knife coating and tape casting.[53,54] Other effective methods that have been applied to deposit precursors and form elastomer layers are spray coating,[10] used for fabrication of multilayer DEAs, inkjet printing[55] that can create precise profiles of deposited elastomer layers, dip coating[56] that has been used for multilayer coaxial DEAs, and pad-printing that can create elastomer layers as thin as 3 μm, with lateral strains of 7.5% at only 245 V.[57]

B. Mechanical response of elastomers

Various hyperelastic models have been devised to represent the mechanical behavior of elastomers, some for analytical simplicity in modeling and others for capturing the molecular rearrangements under deformation. Two of the most common material models used to describe mechanical responses of dielectric elastomers are the neo-Hookean and the Gent model (Sec. III A). The neo-Hookean model is the simplest hyperelastic material model that describes the stored energy of the elastomer under deformation in terms of the sum of squared principal stretches. From a statistical mechanics point of view, it is equivalent to a Gaussian model in which the change in stored energy due to mechanical deformations is associated with the decrease in configurational entropy of randomly oriented polymer chains.[58] For the larger deformations, where the polymer chains are stretched nearly to their fully extended length, the phenomenological Gent material model[31] is generally preferred since it incorporates strain stiffening using a simple empirical equation. It is also known to be an accurate approximation to a molecular based stretch-averaged full-network model involving the inverse Langevin function.[59]

Representative stress–stretch behaviors of elastomers are shown in Fig. 7. Figure 7(a) is of a commercial urethane acrylate

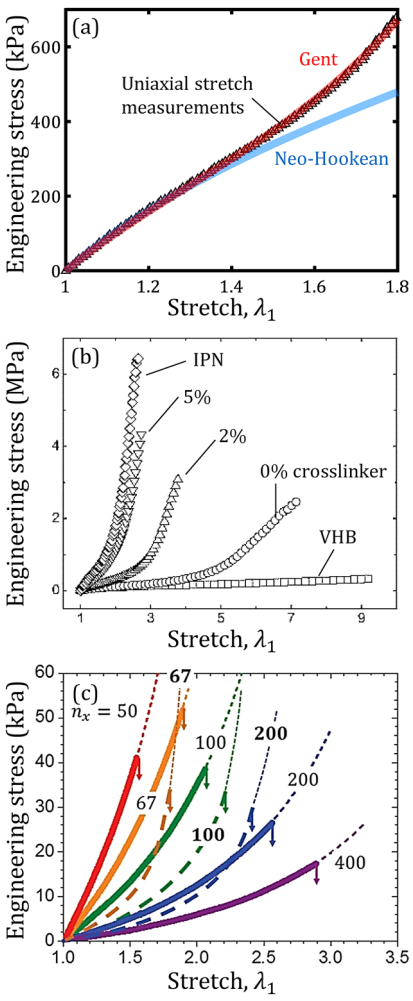

FIG. 7. Examples of the mechanical response of acrylic-based and silicone-based elastomers. (a) Stress–stretch measurements of a commercial urethane acrylate elastomer (CN9018, Sartomer Arkema Group) with 5% HDDA cross-linker, together with the fitting curves of neo-Hookean and Gent models. The increase in the slope of stress–stretch curves with the stretch is a measure of strain-stiffening and is only captured by the Gent model. (b) Stress–stretch measurements of another commercial urethane acrylate elastomer (CN9021, Sartomer Arkema Group) with different concentrations of HDDA cross-linker, compared to 3M VHB™ elastomer films and an interpenetrating network (IPN) of VHB and poly(1,6-hexanediol diacrylate).[60] Increasing cross-linking increases the stiffness at the expense of extensibility. Reproduced with permission from Niu *et al.*, J. Polym. Sci., Part B: Polym. Phys. **51**(3), 197–206 (2012). Copyright 2012 John Wiley and Sons. (c) Stress–stretch measurements for bottlebrush elastomers with side chain degree of polymerization of $n_{sc} = 14$ and 28, shown with solid and dashed lines, respectively, and different backbone degrees of polymerization, n_x,[26] to which a two-parameter material model is fitted. The measurements show the highly controllable strain-stiffening of the bottlebrush elastomers and their low stiffness, nearly two orders of magnitude lower than the acrylic-based elastomers shown in (a) and (b). The downward arrows show the rupture stretch of the samples that is approximately inversely proportional to the elastomer stiffness. Reproduced with permission from Vatankhah-Varnoosfaderani *et al.*, Adv. Mater. **29**(2), 1604209 (2016). Copyright 2016 John Wiley and Sons.

elastomer (CN9018, Sartomer Arkema Group) with 5% 1,6-hexanediol diacrylate cross-linker (HDDA). The neo-Hookean model fitted to the measurements can describe only the initial portion of the curve accurately, whereas the Gent model overlaps the data over the entire stress–stretch curve capturing the strain-stiffening behavior, the increase in slope with stretch. The role of cross-linking in modifying the stress–stretch behavior is illustrated in Fig. 7(b) for a typical urethane acrylate based elastomer, CN9021, with different densities of 1,6-hexanediol diacrylate cross-linker.[60] With no cross-linker, the acrylic exhibits a low storage modulus of less than 1 MPa and a stretchability of more than 600% uniaxial strain. With increasing cross-linking density, the modulus increases and the attainable stretch decreases. The former is consistent with polymer physics theories that predict the elastic modulus varies as the reciprocal of the molecular weight of chains between cross-links.[42] Also, the stretch at which the elastomer shows strain stiffening decreases with the density of cross-linkers. Since strain stiffening is desirable to prevent electromechanical instability, as discussed in Secs. II and III, the optimum cross-linking density is one that balances achieving a low modulus for a large actuation with appreciable strain stiffening. This optimum is commonly determined empirically by varying the cross-linking density.[11,60]

Another approach to manipulate the strain-stiffening behavior of elastomers is the use of interpenetrating polymer networks,[35] in which, first, a soft elastomer consisting of long polymer chains is stretched biaxially and then, while stretched, a precursor of shorter oligomers is diffused into the host network and reacted to form a relatively stiff strain-free secondary network inside the host elastomer. Releasing the stretch of the host elastomer compresses the secondary network leaving the host elastomer partially stretched. This is, in essence, similar to prestretching the elastomer to avoid electromechanical instability, but instead of the common practice of holding it stretched by attaching to a rigid frame, the prestretch is maintained internally by the secondary network. Based on the density of the secondary network, the strain-stiffening behavior of the initial elastomer can be manipulated. For instance, DEAs based on interpenetrating networks (IPN) of VHB as the host elastomer and poly(1,6-hexanediol diacrylate) as the interpenetrating network has shown area actuation strains of 233%, corresponding to equibiaxial lateral actuation stretch of $\lambda_1 = 1.82$.[35] This value is close to the maximum theoretical limit of $\lambda_1 = 2.26$ for equibiaxial DEAs, assuming that the electromechanical instability is the failure mechanism (Sec. III B). Attractive as the interpenetrating network elastomers are, no methods of incorporating them into the fabrication of multilayer DEAs has yet been demonstrated.

Another new class of elastomers with promise for DEA applications is the bottlebrush elastomers. In these elastomers, the backbones of the polymer network are inherently strained, due to the presence of long, densely packed side chains, leading to intrinsic strain-stiffening behavior to prevent electromechanical instabilities. Significantly, despite the high density of large side chains, areal expansions of more than 300% have been reported.[26] As shown in Fig. 7(c), high degrees of polymerization of the side chains lead to a unique combination of softness and strain stiffening at lower stretches. The key to making high-performance bottlebrush elastomers for DEA applications is the accurate and independent control of the degree of polymerization of the side chains, spacers between

neighboring side chains, and the backbone of the bottlebrush network strands.

C. Dielectric breakdown of dielectric elastomers

As the maximum achievable actuation strain and force depend on the square of the electric field that can be sustained, there is considerable interest in factors that determine the electric breakdown. Presently, the electrical breakdown strength of common dielectric elastomers used in DEA applications fall in the range of 50–300 V/μm.[61–63] In many respects, though, a detailed understanding of electrical breakdown in elastomers is still very much in its infancy. In part, this is because of the direct coupling between the electric field and deformation and because DEAs operate in a regime in which the stored electrical energy density is comparable with the mechanical strain energy density. This is not the case in other dielectrics, such as polymer capacitors or oxides. In addition to affecting underlying breakdown mechanisms, this can also affect the measurement of breakdown strengths since elastomers are so soft that their local thickness can decrease during the test. This requires particular care in some tests, such as those in which the voltage is applied using a spherical metal contact. It is also unclear how the intensive studies of electrical breakdown in thin gate oxides, and earlier studies of high-permittivity oxides and polymer dielectrics, can be translated to elastomer devices. Nevertheless, as in other materials, the breakdown must involve multiple processes including excitation and multiplication of free charge carriers,[64] the creation of excited radicals and species, as well as in the later stages Joule heating due to high current densities. Each of these are expected to be affected by local mechanical deformation due to the large localized electric fields.[65] Readers interested in mechanisms as well as reviews on breakdown mechanisms in polymers are referred to Refs. 66 and 67. In this section, dielectric breakdown of elastomer materials is considered. Soft breakdown, a phenomenon that mainly stems from the electrodes of the DEAs and capacitors, in which the electrical breakdown paths do not behave like Ohmic resistors,[68] will be discussed in Sec. V F.

The electrical breakdown strength of a material is not an intrinsic property of a material just as the mechanical strength is not. Instead, the breakdown strength is found to depend on geometrical parameters, such as thickness and area under field, and can vary from one batch to another. In stiff dielectrics, the breakdown field varies with thickness as $E_B \propto t^{-\alpha}$ where the exponent is ~0.5.[69] This power law dependency on thickness suggests that, as with the mechanical strength of brittle materials, the breakdown strength is statistically determined by the probability of a breakdown-facilitating defects lying within the stressed volume. By the same argument, the electrical breakdown strength can be expected to decrease with increasing area under field. At the present stage in DEA development, dielectric elastomers unavoidably contain defects such as dust particles, air microbubbles, nonuniform thickness, gel particles, and nonuniform cross-linking. These can act to initiate local electrical breakdown although the mechanisms involved are not established. Nevertheless, as will be described in Sec. V F, the ability of the electrodes to self-clear and form nonconductive regions around these defects can significantly improve the electrical breakdown strength of actuator devices and result in high-performance and fault-tolerant actuators.[70,71]

The statistical distribution in measured breakdown strengths are appropriately represented in terms of extreme value statistics, for instance, Weibull statistics. The cumulative distribution function of the two-parameter Weibull distribution is given by the probability that breakdown occurs at, or below, an electric field, E,

$$P(E) = 1 - e^{-\left(\frac{E}{E_B}\right)^{\beta}}. \tag{30}$$

E_B and β are, respectively, the electrical breakdown field and the Weibull modulus (also called shape parameter). A large Weibull modulus is desirable since it indicates a narrow distribution and is a measure of the reliability for designing devices based on a specific value of the electrical breakdown strength. The electrical breakdown strength parameter, E_B, is the electric field up to which 63% ($\cong 1 - e^{-1}$) of the samples fail, approximating the arithmetic average of the breakdown field. Figure 8 presents examples of electrical breakdown measurements for Sylgard 184 with different ratios of oligomers to curing agents and Wacker 613, commercial silicone-based elastomers, VHB F9460, an acrylic-based elastomer, and thermoplastic poly-(styrene-co-ethylene-co-butylene-co-styrene). Fitting the Weibull cumulative distribution functions to the measurements show electrical breakdown strengths ranging from ~30 to ~130 V/μm and Weibull moduli in the range of ~8 to ~34, characterized by the slope of the $\log[\log[1/(1-P)]]$ vs $\log E$ curves. These measurements were made with a spherical electrode in contact with the elastomer on a rigid, conducting substrate.[72]

The electrical breakdown field, E_B, and the reliability parameter, β, depend not only on the material but is also strongly affected by factors such as the film surface area,[73] film thickness,[61,74,75]

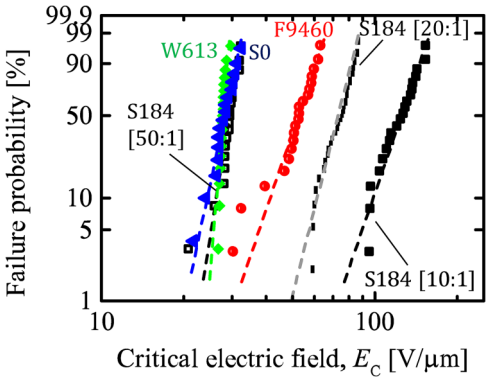

FIG. 8. Fitting cumulative Weibull distribution functions to the electrical breakdown strength measurements of Sylgard 184 (labeled as S184) with different ratios of oligomers to curing agents, Wacker 613 (labeled as W613), poly-(styrene-co-ethylene-co-butylene-co-styrene) (labeled as S0), and 3M VHB™ F9460 (labeled as F9460) show electrical breakdown strengths in the range of ~30 to ~130 V/μm and Weibull modulus of 8–34. Figure courtesy of M. Kollosche.

prestretch,[61,76] material stiffness,[4,77] and density of defects and inclusions.[78,79]

The effect of surface area on the electrical breakdown strength can be shown through a simple analysis of the Weibull distribution of electrical breakdown.[73] Consider that the electrical breakdown measured on a sample with surface area A_1 is E_{B1} and β_1. For a film whose surface area is $n = A_2/A_1$ times larger, the first electrical breakdowns in any of the n portions would lead to the breakdown of the entire film. Therefore, due to the statistical independence of electrical breakdown process of each of those n portions, the probability of survival of the film with n times larger surface area, $1 - P_2$, is the probability of survival of all n portions $(1 - P_1)^n$,

$$P_2(E) = 1 - (1 - P_1(E))^{\frac{A_2}{A_1}} = 1 - e^{-\frac{A_2}{A_1}\left(\frac{E}{E_{B1}}\right)^{\beta 1}}. \tag{31}$$

The implication is that the Weibull modulus does not change significantly with increases in the surface area, but the electrical breakdown is reduced by a factor of $(A_2/A_1)^{-1/\beta}$,

$$\begin{aligned} &\beta_2 \sim \beta_1, \\ &E_{B2}/E_{B1} \sim (A_2/A_1)^{-1/\beta}. \end{aligned} \tag{32}$$

The decrease in electrical breakdown with surface area is strongly affected by the value of the Weibull modulus, β. For instance, for silicone elastomers, for which a range of 10–40 is reported for β,[80] an increase in surface area by 100 and 10 000 times will decrease the electrical breakdown field by ~37% and ~60%, respectively, when $\beta = 10$, but by only 11% and 21%, respectively, when $\beta = 40$.

Although the electrical breakdown strength of elastomer films show a similar power law dependence on thickness as hard dielectrics, the physical basis and the exponent α in $E_B \propto t^{-\alpha}$ differs and also there is an apparent linear increase in the Weibull modulus with thickness $\beta \propto t$.[78,80] For instance, the VHB acrylic elastomer sheets from 3M, the material most commonly used in early works on dielectric elastomer actuators, exhibit a $E_B \propto t^{-0.25}$ dependency.[61] Silicone elastomers show similar thickness dependence: $E_B \propto t^{-0.23}$.[62] The possibility that the processing used to make the elastomer affected the observed reduction in electrical breakdown strength with thickness was ruled out, since electrical breakdown strength decreases with film thickness whether the films are made of single layers with different thicknesses or multiple layers each having the same thickness.[63]

No single model adequately describes the reduction of the electrical breakdown strength with thickness. Some of the essential ideas are, however, expressed in charge injection models such as[81] for polymer dielectrics. Under high fields, electrons from the cathode and holes from the anode are injected into the dielectric and diffuse as charge packets within the polymer film under the applied electric field to create space charge regions in the vicinity of both electrodes. This, in turn, modifies the electric field profile inside the polymer. The peak of the electric field profile is significantly larger than the nominal applied electric field, causing electrical breakdown when it exceeds the local breakdown strength. The model predicts a power law dependence on the thickness often observed in experiments but the calculated exponent, $\alpha = 0.125$, is significantly smaller, about half of that measured. It is also consistent with measurements of the distribution of space charges within polymer films and their strong influence on electrical breakdown.[82,83] According to this model, a significant contributor to the lower electrical breakdown field measured for the thicker polymer films is due to the fact that at the same voltage ramp up rate, the electric field ramp up rate is smaller for the thicker polymer films and there is a longer time for the injected charges to migrate and create a larger peak for electric field profile inside the polymer film. This suggests that if the polymer films were to be tested at the same electric field ramp up rate, the measured dependence of the electrical breakdown strength on thickness would have been different. While such charge injection models capture many key concepts, their direct applicability to elastomers remains to be established since they do not take account of the mechanical deformation produced under large electric fields in soft elastomers.

The electrical breakdown strengths of soft elastomers also depend on their mechanical stiffness. When breakdown is associated with the onset of the electromechanical instability, this can be readily understood from the instability criteria discussed in Sec. III. Support for this interpretation comes from experiments with chemically similar blends of thermoplastic soft elastomers having different elastic stiffness. These show an increase in electrical breakdown strength with stiffness and also showed that hyperelastic models of electromechanical instability predict the stiffness dependence of electrical breakdown.[77] As individual elastomer layers are constrained by one another in multilayers, it can be expected that the local electromechanical instability is less likely, at a given field than a free-standing elastomer. This would suggest, but has not been demonstrated, that the breakdown strengths are higher in multilayer devices than in single-layer actuators.

Preventing the electromechanical instability is not the only mechanism by which prestretching increases the electrical breakdown strength of elastomers. Even for fully constrained elastomer films for which no deformations are allowed and so no electromechanical instabilities are expected, prestretching increases the electrical breakdown strength of an elastomer.[61] Under fully constrained conditions, the dependence of the electrical breakdown strength on stretch has been found to vary as $E_B \propto \lambda^q$, with $q = 0.63$ for VHB acrylic elastomers[61] and $q = 0.77$ for silicone-based elastomers.[62] The increase in electrical breakdown strength with lateral stretch is also observed when the volume of the samples is conserved. This is observed with elastomers biaxially stretched by λ, where the electrodes are λ^2 times larger.[63] For context, prestretching is used in the manufacture of high-performance biaxially-oriented polypropylene (BOPP) polymer dielectrics. As the name suggests, the polypropylene is biaxially stretched, at elevated temperatures, to preferentially orient the polypropylene molecules in the plane of the film, and this oriented state is then frozen in on cooling. It is generally thought that such a preferential molecular alignment is not possible in elastomers since the energy for molecular re-arrangement is small. However, there are examples of optical birefringence in some elastomers while mechanically stretched,[84–86] indicating that molecular alignment can occur under deformation. This suggests that alignment can also occur under an electric field and this is demonstrated in Fig. 9,

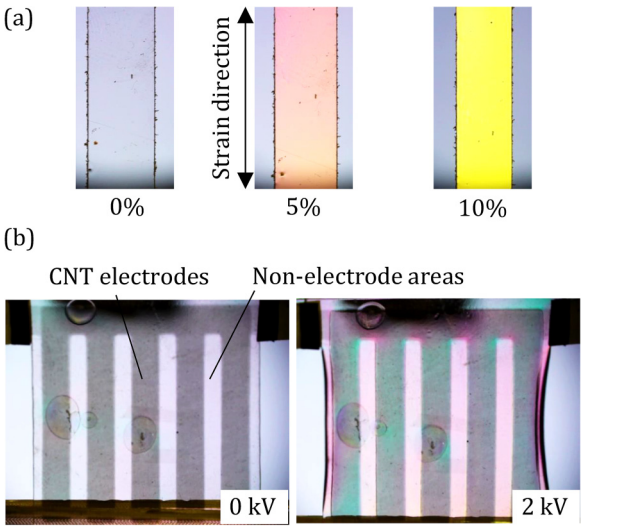

FIG. 9. Birefringence of dielectric elastomers. (a) Mechanically stretching a 0.7 mm thick multilayered strip of CN9028, an acrylic-based dielectric elastomer, by 5% and 10% uniaxial strain causes birefringence as evidenced by the change in its color when placed between two parallel polarizers with their axis at 45° with respect to the birefringence axis of the elastomer, and illuminated by a background white light source. (b) Birefringence of a CNT electroded elastomer sheet before and during electrostatic actuation. The electroded regions exhibit green birefringence at 2 kV as they expand, whereas the non-electroded areas that are inactive but are being compressed laterally in width appear red. Blisters formed as a result of soft breakdowns are also apparent.

which shows the birefringence of an acrylic-based elastomer, CN9028 (Sartomer Arkema Group), under both mechanical and electrical loadings. (The imaging conditions consist of the elastomer sheet between two parallel polarizers, whose transmission axis is at 45° with respect to the horizontal direction in Fig. 9, illuminated by a background white light source.) In Fig. 9(a), the elastomer strip is mechanically stretched by up to 10% showing a large change in color. The same effect can be seen for electrical loading of a DEA having a comb-like electrode geometry [Fig. 9(b)] where the birefringence colors in the electroded and non-electroded areas are different, indicating different magnitude and orientation of the polymer chains. In this configuration, when a voltage is applied, the electroded areas of the DEA expand in width while their neighboring non-electroded areas are compressed in width, causing two different orientations of largest principal stretch. Again, the mechanism by which molecular orientation might affect the breakdown strength remains to be established.

D. Long-term degradation of dielectric elastomers

The effect of large electric fields applied to elastomers over extended periods of time have yet to be studied in detail although some devices have exhibited voltage cycling for millions of cycles, albeit for short cycles. Long-term aging is a concern since it occurs in polymeric systems, such as high-density polyethylene (HDPE) and XLPE—cross-linked polyethylene used as insulation for high-voltage cables[87]—as well as in polymer films.[88] Assuming that the degradation mechanism is both thermally activated and biased by the electric field, the general transition rate equation can be written in the form

$$t_f \cong \frac{h}{2k_BT}\, e^{\Delta G_o/k_BT}\,\mathrm{csch}\left(\frac{eaE}{k_BT}\right), \tag{33}$$

where t_f is the time to fail, h is the Planck constant, k_B is the Boltzmann constant, T is the absolute temperature in Kelvin, ΔG_0 is the Gibbs free energy difference of the products and reactants, and e is electrical charge of electrons. a is a characteristic distance along which a charged species moves under the applied electric field, E.

A variety of mechanisms can be described by this formulation including field-assisted migration of moisture in HDPE and XLPE cables, space charges, or some other charged species in polymer films under an electric field.[88] The mechanism can then be represented by equilibrium reaction, for instance, between charges on radical species or the trapping–detrapping of space charges. The concentration of the species then evolves according to the local reaction as $dX/dt = k_f X + (1 - X)k_b$ where the coefficients k_f and k_b are, respectively, the forward and backward reaction rates and are proportional to the absolute temperature, T, and decrease exponentially with an activation energy, G. The electric field, E, biases the reaction, decreasing the forward activation energy as a function of electric field, $G - CE^b$, and drives the equilibrium toward an increase in local reaction products, X. To apply this biased equilibrium to breakdown under aging conditions, it is necessary to assume that electrical breakdown occurs when the reaction product concentration reaches a critical value of X^*. In the relatively few cases where detailed studies of aging have been performed, the lifetimes fit the temperature and electric field dependence given by Eq. (33).[87,88] Given the lack of specificity of the mechanisms, the predictions made using this equation can only be used to compare aging results for the same material, although this can be indispensable for a particular device. It can be expected that dielectric elastomer actuators will exhibit long-term aging. Indeed, because they are rather open structures, long-term degradation by field-assisted diffusion of moisture and other mobile charge species is likely unless protective measures are implemented.

Degradation of actuators can occur due to the degradation of the dielectric elastomer under high electric field but also by degradation of the electrode under cyclic deformations. This will be discussed in Sec. V C.

E. Increasing the dielectric constant

The dielectric permittivities of most elastomers are small, typically 3–6 at low frequencies, as elastomer molecules generally lack highly polarizable ions. As the actuation strains are proportional to the dielectric constant, there are continuing activities directed toward increasing its value by incorporating nanoparticles having large dielectric constants[89–91] or using sub-percolative concentrations of conductive fillers.[79,92,93] The results show increases in dielectric constant as expected and in proportion to their volume fraction, consistent with simple mixing rules, indicating that the approach

holds promise for the future. However, the approach faces two hurdles, one related to electrical breakdown and the other the inherent mechanical stiffening the particles confer. In most studies, the addition of high-dielectric particles severely reduces the electrical breakdown strength although only the breakdown field is usually reported and not the Weibull statistics. Much of the decrease is probably due to inhomogeneities in the spatial distribution of the particles, raising the local electric field and initiating breakdown. More refined approaches have been recently been used to creating a uniform particle distribution. Nevertheless, the difficulties in the approach are illustrated by reporting that the addition of 2% of conductive carbon black particles in poly-(styrene-co-ethylene-co-butylene-co-styrene) resulted in an order of magnitude decrease in electrical breakdown while the permittivity only increased by a factor of ~2.[79]

One way of assessing the relative merits of nanoparticle additions is to use the non-dimensional maximum electric field, $\sqrt{\epsilon/\mu}E_B$, as a figure of merit. For instance, this figure-of-merit decreases by a factor of ~7 for the 2% carbon black fillers in poly-(styrene-co-ethylene-co-butylene-co-styrene). Inclusion of 20% titanium dioxide particles in poly-(styrene-co-ethylene-co-butylene-co-styrene) increased the elastic modulus by a factor of ~3.9 while the permittivity only increased by ~2.5.[89] Composites of ceramic particles in elastomer matrices can moderately increase the permittivity while maintaining or, in some cases, even increasing the average electrical breakdown strength.[89,90] However, the large volume fractions of stiff ceramic particles required to cause a notable increase in permittivity increases the elastomer stiffness, balancing the increased permittivity and potentially reducing the non-dimensional electrical breakdown field. Furthermore, although increasing the average breakdown field is important in many practical instances, this is not useful if the Weibull modulus decreases.

V. COMPLIANT ELECTRODES

The over-riding requirements of the electrodes is that they can distribute charges from the power supply over the surface of the dielectric while also being sufficiently compliant that they can follow the large strain deformation of the elastomer without constraining the elastomer. Formally, this mechanical requirement is given by Eq. (29) for a biaxial actuator. It is also necessary that the electrode conductivity is sufficiently high so that Ohmic energy losses are low and the RC time constant for charging and discharging is less than the viscoelastic time constant for elastomer deformation. (RC time constant is the product of the circuit resistance and the circuit capacitance). In addition, it is also desirable that they can be patterned and adhered well to prevent possible delamination between layers when used in a multilayer configuration.

One effective method for achieving such compliant electrodes, which will be the focus of this section, is to form quasi-two-dimensional percolating networks of high-aspect-ratio nanoparticles such as carbon nanotubes or metallic nanowires on dielectric elastomer sheets.[94] A percolating network of conductive particles allows for electrical conduction through numerous percolating paths, and when stretched, the individual or patches of particles easily slide relative to each other to give high mechanical compliance. Methods other than percolating networks of conductive particles has also been developed for compliant electrodes of DEAs, such as ionogels[91] and liquid metals,[95] which will not be discussed here for reasons discussed in Sec. II.

In this section, first, a percolative network of conductive high-aspect-ratio particles, such as carbon nanotubes, is identified as an effective percolative system for compliant electrodes, drawn from a couple of key theoretical and experimental studies on percolative systems and their electrical conduction. Next, a simple recipe for fabrication of such percolative networks of carbon nanotubes is presented, for which mechanical and electrical characterizations are performed, and alternative fabrication methods are discussed. The electrical characterizations investigate the conductivity of these thin film electrodes, their performance as electrodes for capacitors given their partial surface coverage, and their degradation under high currents, which leads to self-clearing for fault-tolerant dielectric elastomer actuators. The mechanical characterizations investigate the added mechanical stiffness from the electrodes to the dielectric elastomer actuators and the change in electrical conductivity under mechanical loading.

A. Conductive networks of percolating particles as compliant electrodes

Even before the detailed mechanics of the restraining effect of electrodes were fully developed, it was recognized that the electrodes for DEAs need to be capable of large extensions and so would have to consist of networks or mats of percolating conducting particles. (In the earliest studies, carbon grease was often used as electrodes.) It was also appreciated that the electrodes need to have a low concentration of particles to minimize the electrode stiffness. These considerations naturally led to the development of electrodes based on carbon nanotubes, nanowires, and carbon black nanoparticles.

Although a thin electrode of high-aspect ratio conducting fibers is neither a random three-dimensional nor a truly two-dimensional random arrangement, for which exact solutions exist, guidance for the selection of random percolating fibers can be gained from the percolation properties of fibers. Specifically, Balberg *et al.*[96] developed the excluded volume method and showed that at the percolation threshold, the total excluded volume of a system of particles with a given shape is a system invariant. For a two-dimensional percolating network of high aspect ratio fibers of length l_{fiber} and diameter d_{fiber}, the number of fibers per surface area at the percolation threshold, N_c, is proportional to the inverse of squared length of fibers, $N_c l_{\text{fiber}}^2 = \text{constant}$. Therefore, the critical mass density of fibers required to form a percolating network, which is $\rho_c \propto N_c l_{\text{fiber}} d_{\text{fiber}}$ in 2D, is inversely proportional to their aspect ratio, $\rho_c \propto (l_{\text{fiber}}/d_{\text{fiber}})^{-1}$. In other words, high-aspect-ratio particles such as carbon nanotubes and metal nanowires require much lower volume densities to form the first percolating path, compared to more equiaxed nanoparticles such as carbon black and spherical colloids.

In practice, the density of conducting fibers must be significantly larger than the percolation threshold both to have a high conductivity and to assure uniform charge distribution, especially at maximum stretch. Beyond the percolation threshold, increasing the number density of fibers connects separate clusters resulting in

a sharp jump in the size of the largest cluster. However, the conductivity near the percolation threshold increases only gradually and fits a power law function, $\sigma \propto (\rho - \rho_c)^t$, whose slope is zero at percolation threshold. Well above the threshold, the conductivity increases linearly at higher densities, as shown in an elegant tabletop experiment by Last and Thouless,[97] and well described by effective medium models.[98]

Measurements of electrical conductivity of quasi-two-dimensional percolating networks of carbon nanotubes[99] showed similar results for electrical conductivity near the percolation threshold, $\sigma \propto (\rho - \rho_c)^{1.5}$. A similar dependence but with an exponent of 1.8 is found for the sheet conductivity of the CNT electrodes as a function of their areal density [Fig. 10(a)] fabricated using the procedure described in Appendix B. The power law function for the electrical conductivity shows that the lower the critical density, ρ_c, the higher the electrical conductivity, σ. Therefore, high-aspect-ratio conducting nanoparticles such as carbon nanotubes, for which the critical density $\rho_c \propto (l_{\text{fiber}}/d_{\text{fiber}})^{-1}$ is smaller by several orders of magnitude, are by far more effective than equiaxed nanoparticles, such as carbon black, for creating conductive percolative networks.

B. Fabrication of CNT electrodes

An enormous literature on CNT electrodes has developed in the last 20 years as interest has grown in their use in electronic devices, wearable electronics, and displays as possible replacement of ITO transparent conductors. Much of the knowledge established for these applications is transferrable to the use as electrodes for DEAs, but there are two important additional requirements. One is the requirement that the electrode must be stretchable without losing appreciable conductivity. The other is a processing constraint that they can be deposited uniformly on materials having a low surface energy since most elastomers have a surface energy of less than 0.03 mJ/m^2. This compares with the surface energy of silicon of 1.24 J/m^2 and glass of 4.4 J/m^2.

No single fabrication method suits all applications, but the one we have adopted for low volume applications is described in Appendix B for readers interested in making their own devices. This procedure, which is one of the many variations of the original techniques[99–101] for fabrication of thin film carbon nanotube electrodes, consists of two main steps: making a suspension of carbon nanotubes through sonication, centrifuging, and decanting, followed by depositing the suspension as a percolating thin film of CNTs by vacuum filtration and stamping.

The method used to prepare the CNT suspensions affects the concentration of CNTs in the suspension as well as the conductivity of the deposited CNT film (at the same film thicknesses). In addition to the procedure presented in Appendix B, other examples for making CNT suspensions are to disperse non-functionalized CNTs in solvents such as chloroform[99] or in de-ionized water using surfactants such as sodium dodecyl sulfate[94] or to use functionalized CNTs with other functional groups such as polyethylene glycol (PEG) or poly(aminobenzene sulfonic acid) (PABS). The latter can result in higher stable concentrations of carbon nanotubes in de-ionized water[102] but lower electrical conductivity of the electrode.[103,104] On the other hand, suspensions of CNTs with

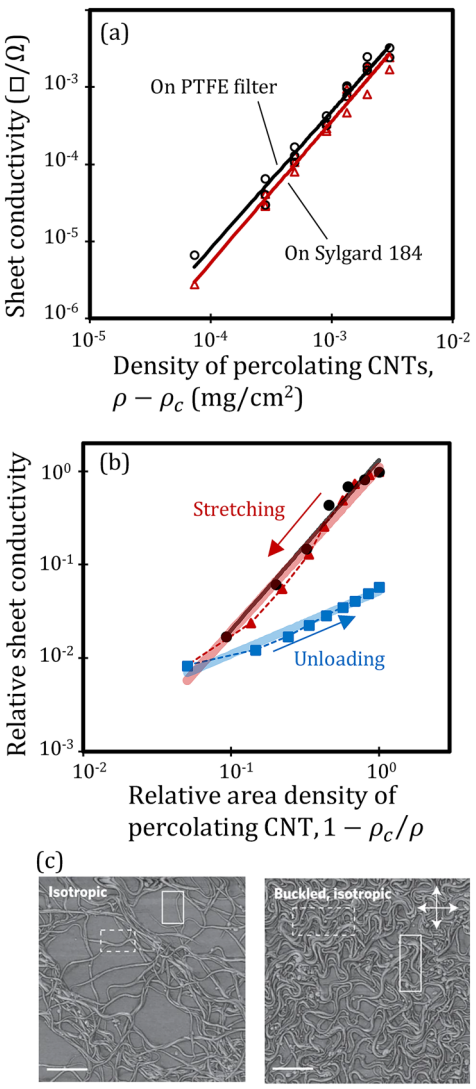

FIG. 10. Sheet conductivity of CNT electrodes under mechanical loading. (a) Sheet conductivity, σ, of CNT electrodes as a function of the area density, $\rho - \rho_c$, on a PTFE filter (black) and after stamping onto Sylgard 184 elastomer (red). Both exhibit a power law dependence, $\sigma \propto (\rho - \rho_c)^t$, with an exponent $t = 1.8$. (b) Comparison of the sheet conductivity of biaxially stretching a CNT electrode stamped on VHB (red solid triangles) with those measured for non-stretched electrodes with lower CNT density (black solid circles). The fitted curves for sheet conductivity under biaxial stretching (red line), $\sigma = \sigma_0(\rho_0/\lambda^2 - \rho_c)^t$, and non-stretched electrodes with lower CNT densities (black line), $\sigma = \sigma_0(\rho - \rho_c)^t$, match each other. On unloading back to the unstretched state, the electrode conductivity is reduced and follows a similar power law dependence but with a lower exponent. This is attributed to the permanent buckling of CNTs resulting in shorter effective lengths. The blue line shows the fitted curve $\sigma = \sigma_0(\rho_0/\lambda^2 - \rho_{c0}\lambda_{\max}/\lambda)^t$ with $\lambda_{\max} = 1.3$. (c) SEM images of CNT electrodes under mechanical loading shows buckling of CNTs during unloading.[120] The CNTs shown in white boxes show straight CNTs before mechanical loading and buckled CNTs after the first cycle of loading and unloading. Reproduced with permission from Lipomi *et al.*, Nat. Nanotechnol. **6**(12), 788–792 (2011). Copyright 2011 Springer Nature.

carboxylic acid groups (Appendix A) show high concentrations of CNTs, and their deposited electrodes have similar electrical conductivities as those of purified non-functionalized CNT electrodes at the same film thicknesses.[103] Electrical conductivity of CNT electrodes can be further enhanced through acid treatments[105–107] or doping with potassium or bromine.[108]

To deposit CNT suspensions and form electrodes, vacuum filtration and stamping through shadow masks (Appendix B) offers a good balance between ease of application and high homogeneity and complexity of the CNT electrodes. However, this method is not suited for automatic, precise, or large-scale fabrication of CNT electrodes, for which other deposition methods are preferable. For example, instead of using shadow masks, CNT electrodes can be transferred using patterned polydimethylsiloxane (PDMS) stamps[109] for repeated fabrication of electrodes with complex geometries. A comparison of three common deposition methods for CNT electrodes and their advantages and challenges are presented in Table II.

The main challenge with the inkjet printing and spray coating of CNT electrodes is avoiding inhomogeneities due to the capillary flow toward the edges of the deposited (micro-)droplets during the evaporation of the solvent that forms ring-like concentrations of CNTs, known as coffee rings.[110,111] Two common practices to minimize this form of processing inhomogeneity are oxygen plasma (or ozone UV) treatments to decrease the contact angle and heating the substrate to accelerate the solvent evaporation. While effective in reducing the dewetting inhomogeneity in inkjet printing of carbon nanotube electrodes,[112] surface plasma treatments can create very thin, brittle layers of silica on PDMS elastomers,[113,114] which micro-crack and grow when the elastomer is stretched. Not only is the surface embrittled but the cracks can disrupt the CNT network causing a sharp decrease in electrical conductivity.[106,115]

C. Electrical conductivity of CNT electrodes under mechanical deformations

When stretching an elastomer sheet with stamped CNT electrodes, individual and small bundles of carbon nanotubes must slide past one another, and the electrode only remains conductive as long as multiple percolating paths persist. However, the sheet conductivity decreases since the number of percolating paths in the CNT network decreases because of the increase in electrode surface area. This is illustrated in Fig. 10(b) by measurements of the electrical sheet conductivity of CNT electrodes, stamped onto a VHB elastomer, while it was stretched equi-biaxially, $\lambda = \lambda_x = \lambda_y$. The CNT electrodes were made by vacuum filtration of non-functionalized carbon nanotubes suspended in de-ionized water using 1% sodium dodecyl sulfate surfactants. Stretching the electrodes decreases the areal density of carbon nanotubes by $\rho = \rho_0/\lambda^2$, whereas the sheet conductivity of mechanically stretched electrodes decreased according to $\sigma = \sigma_0(\rho_0/\lambda^2 - \rho_c)^t$. The data follow the same curve as reference electrodes made with different areal densities of carbon nanotubes, $\sigma = \sigma_0(\rho - \rho_c)^t$, shown by the black solid circles in Fig. 10(b). The similarity over almost two orders of magnitude suggests that mechanical stretching of carbon nanotube electrodes does not damage either the individual CNTs, as they slide on top of each other, or the homogeneity of the network. Both these effects would have resulted in a percolative network with shortened or separated patches of carbon nanotubes that, in turn, would have had significantly lower sheet conductivity.

On unloading the mechanically stretched CNT electrodes, the sheet conductivity does not follow the same curve as the non-stretched electrodes and decreases orders of magnitude compared to the original non-stretched electrode, as has been reported previously.[120] The same behavior has been observed for the CNT electrodes sandwiched between two PDMS elastomer layers.[121] During unloading, the carbon nanotubes undergo compression and buckle, due to their high-aspect ratio, as has been observed in the scanning

TABLE II. Comparison of common deposition methods for CNT electrodes.

Deposition method	Advantages	Disadvantages
Vacuum filtration and stamping (Appendix B)[99–101]	• Highly homogeneous CNT electrodes with relatively complex geometries • Simplicity and ease of application	• Not scalable to large-scale electrodes or suitable for precise submillimeter electrodes • Not suitable for automation
Inkjet printing[104,106,112,115,116]	• Automated and high-resolution deposition of CNT electrodes with complex geometries (e.g., 80 μm feature sizes on PDMS elastomer sheets[106] • Precise control of the local density of CNTs and the local electrical conductivity[106,112,115]	• "Coffee ring" inhomogeneities due to the capillary flow during solvent evaporation
Spray coating[70,117,118]	• Fabrication of large-area CNT electrodes	• "Coffee ring" inhomogeneities due to the capillary flow during solvent evaporation • Mesoscale inhomogeneities due to the nonuniform flow velocity below the spray nozzle,[119] leading to nonuniform deposited film thicknesses[10]

electron microscopy images of unloaded carbon nanotube electrodes [Fig. 10(c)].[120] The decrease in the electrical conductivity can be understood in terms of the shortened effective length of the buckled and curved carbon nanotubes that translates into a higher critical density for percolation, $\rho_c l = \rho_{c0} l_0$. Assuming the carbon nanotubes do not tolerate any compressive force and buckle, their end-to-end lengths decrease proportionally to the unloading stretch, $l/l_0 = \lambda/\lambda_{max}$. This leads to an increase in the critical areal density of the unloaded electrode as $\rho_c = \rho_{c0}\lambda_{max}/\lambda$. As a result, the sheet conductivity increases very slowly as the electrode is unloaded, $\sigma = \sigma_0(\rho_0/\lambda^2 - \rho_{c0}\lambda_{max}/\lambda)^t$. When the electrode is fully unloaded, $\lambda = 1$, the sheet conductivity is $(\rho_0 - \rho_{c0}\lambda_{max})^t/(\rho_0 - \rho_{c0})^t$ times smaller than the original sheet conductivity. For a more detailed analysis of sheet conductivity of CNT electrodes under mechanical loading and unloading, the interested reader is referred to Ref. 122. Similar behavior is observed for the electrical conductivity of silver nanowires in elastomeric matrices during the first cycle of stretching and unloading.[123] The reduction in electrical conductivity of silver nanowire electrodes, which are typically both thicker and stiffer than CNT electrodes, is not due to the buckling of individual nanowires but rather by out of plane wrinkling during the first unloading. The wrinkling increases the surface area and, therefore, reduces the area density of silver nanowires.

Upon re-loading, the relative decrease in sheet conductivity with stretching becomes smaller in subsequent loading and unloading cycles.[124] There are also indications that after the first cycle, the subsequent changes in sheet conductivity are reproducible and reversible,[120] although this requires further, more detailed studies. Part of the decrease in conductivity from the first loading cycle is probably the result of the initial CNT buckling not recovering elastically due to changes in the surrounding elastomer. It also remains to be established whether the changes are greater if subsequent strains exceed the first cycle strains as might be expected if a Mullins's like effect occurs. Studies of long-term degradation of stretchable electrodes made of elastomers filled with conductive particles show that the decreased electric conductivity is highly dependent on the stretch that the electrode is subjected to.[125] Under these conditions, degradation is usually associated with separation between the particles and the elastomer and the rupture of conducting percolating paths between particles. Despite not always knowing the underlying degradation mechanisms, these results emphasize the importance of performing strain-controlled cyclic fatigue measurements of electrodes both on free surfaces and in multilayers.

D. Mechanical compliance of CNT electrodes

It is generally assumed that percolative electrode networks of CNT's and nanowires will have low stiffnesses, because when stretched, individual and small bundles of CNTs are able to slide relative to each other. Under unloading or compression, similar behavior is expected provided that the fibers do not jam into one another and lock together and creating a jamming transition. (Prior to jamming, they may buckle under compression as shown in Fig. 10.) The experimental results reported are consistent with CNT electrodes having high compliance at low areal concentrations but not necessarily at higher concentrations. For example, the added stiffness from CNT electrodes with densities lower than 22.5 mg m^{-2} between acrylic-based elastomer multilayers with layer thickness of ~90 μm and shear modulus of ~0.4 MPa was shown to be insignificant, by comparing the stress–strain curves of the elastomer sheets with and without CNT electrodes [Fig. 11(a)].[11] High densities of carbon nanotubes, however, can reduce the actuation

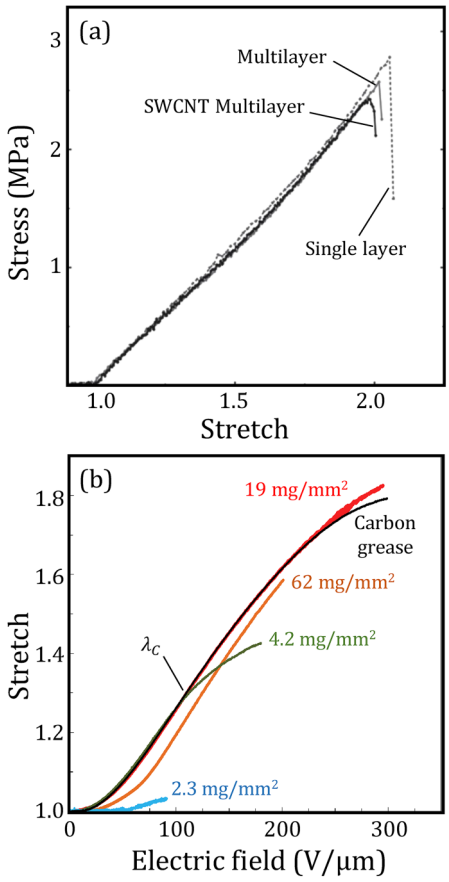

FIG. 11. Mechanical compliance of CNT electrodes. (a) Adding low density single-walled CNT electrodes (less than 22.5 mg m^{-2}) to a soft acrylic-based six-layer elastomer with layer thickness of ~90 μm and shear modulus of ~0.4 MPa does not cause any significant increase in stiffness.[11] The elastomers were stretched until rupture. Reproduced with permission from Duduta *et al.*, Adv. Mater. **28**(36), 8058–8063 (2016). Copyright 2016 John Wiley and Sons. (b) High density of CNTs, e.g., 62 mg m^{-2}, on a 0.5 mm thick acrylic-based elastomer (VHB 4905, 3M Co.) can cause significant decrease in the attainable actuation stretch of the DEA due to the added stiffness, whereas low densities of CNTs lead to loss of percolation at relatively low actuation stretches, e.g., $\lambda_c \sim 1.3$, for 4.2 mg m^{-2} CNT density.[94] Consequently, there is an optimum density of CNTs. Carbon grease is used as a comparison electrode since it follows the elastomer deformation and remains highly conducting. At too low CNT density, e.g., 2.3 mg m^{-2}, the electrode is almost nonconductive and consequently the actuation is nearly zero. Reproduced with permission from Shian *et al.*, Appl. Phys. Lett. **101**(6), 061101 (2012). Copyright 2012 AIP Publishing LLC.

of dielectric elastomer actuators due to their added stiffness. For example, a dielectric elastomer actuator consisting of a prestretched VHB 4905 (3M Co.) 0.5 mm thick elastomer with stamped CNT electrodes with density of 62 mg m^{-2} exhibited lower actuation displacement compared to a 19 mg m^{-2} electrode [Fig. 11(b)].[94] For the very low-density CNT electrodes, less than 4.2 mg m^{-2} s in this instance, the network of CNTs loses percolation at relatively low stretches, shown by λ_c in Fig. 11(b). These results highlight that there will exist an optimum CNT concentration, sufficiently low that its stiffness does not constrain actuation even for the thinnest elastomer actuators but also be sufficiently large that the electrode maintains the required electrical conductivity at maximum stretch.

E. Electrical capacitance of DEAs with CNT electrodes

The Coulombic attraction forces that cause actuation of DEAs are proportional to the voltage-induced electric field within the elastomer and the charge density on the electrodes, $P = qE$ (Sec. II). At a constant applied voltage, the former is proportional to the capacitance. Up until this point, it has been assumed that the charge over both elastomer surfaces is uniformly distributed so that the Coulombic attraction is the same as a parallel plate capacitor with metallic electrodes. Electrodes consisting of mats of conducting, percolative fibers do not cover the entire elastomer surface, so unless there is extensive charge spreading over the surface between the CNTs, the coverage will be patchy. It has been implicitly assumed in the actuator literature that the size of the uncovered areas between CNT patches is small compared with the thickness of the dielectric and so any effects can be neglected under current DEA operating conditions. Although these effects may indeed be negligible for commonly used elastomer thicknesses, in the range of 30–100 μm, they have not been quantified and so the effects of going to much thinner elastomers in order to operate at lower voltages are unknown.

An estimate can, nevertheless, be made using the results of calculations of the capacitance of capacitors with periodic arrays of conducting electrode strips. Grosser and Schulz[126] considered a double-layer capacitor consisting of a periodic array of conductive strips with surface coverage of $s = a/l$ [Fig. 12(a)] sandwiched between two elastomers of equal thickness covered by planar electrodes. They derived an expression for the distribution of electric potential using a potential that automatically satisfies both the Laplace equation and the boundary conditions on the two outer electrodes. From their analysis, it is straightforward to extract the relative capacitance of the double-layer capacitor as

$$\frac{C}{C_{s=1}} = \frac{1}{1 - \frac{l}{\pi t}\ln\left(\sin\left(\frac{\pi s}{2}\right)\right)}, \tag{34}$$

where $C_{s=1}$ is the capacitance for the case where the middle electrode is a planar sheet with full surface coverage and l/t is the relative spacing between the uncovered areas. Figure 12(c) compares the relative capacitance given by the analytical Eq. (34) with complementary COMSOL electrostatic simulations as a function of the ratio l/t and surface coverage s. The COMSOL solution for the distribution of electric potential at a cross section of the double-layer capacitor is shown in Fig. 12(b).

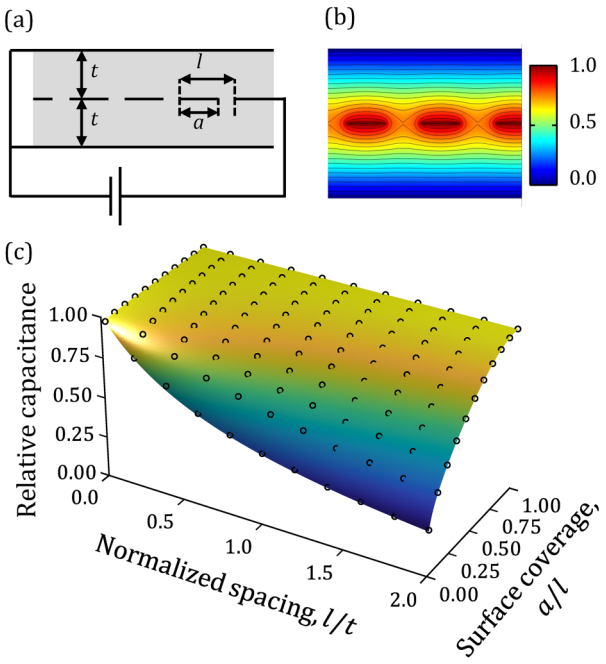

FIG. 12. The decrease in capacitance due to only partial coverage of the electrodes depends on both the surface coverage and the relative spacing between the uncovered areas. (a) Schematic of a double layer capacitor with perforated middle electrode whose surface coverage is $s = a/l$ and the normalized spacing between the uncovered area is l/t. (b) COMSOL simulations for the distribution of electric potentials inside a double-layer capacitor with a perforated strip middle electrode. (c) COMSOL simulations (black circles) and analytical solution for the relative capacitance, $C/C_{s=1}$, as a function of the surface coverage and normalized spacing show that even at extremely small surface coverage, the relative capacitance remains close to 1 if the spacing between the uncovered areas is small compared to the thickness of the dielectric layers.

The calculations reveal that the relative spacing between the uncovered areas, l/t, is as important as the surface coverage itself. This gives several new insights into the design parameters of the CNT electrodes including the importance of homogeneity of the CNT electrodes, the length of the individual CNTs, and the effect of reducing elastomer thickness on the relative capacitance $C/C_{s=1}$. For instance, for a homogeneous network of CNTs, the spacing between the uncovered areas is expected to be shorter than the length of the carbon nanotubes (of the order of 1 μm). So, for a DEA with homogeneous CNT electrodes and elastomer thickness of 20 μm, the relative capacitance, $C/C_{s=1}$, remains above 93% even when the surface coverage is as low as 1%. However, large-scale inhomogeneities in the spacing of the carbon nanotubes, for instance, due to the coffee ring effect, which might be tens of micrometers, can significantly reduce the capacitance of the DEA. Homogeneous percolating networks of metallic nanowires that have similar aspect ratio to that of CNTs but usually tend to be much longer and thicker have relatively larger spacing between the uncovered areas and, therefore, may

result in lower capacitance. This may, in part, be the reason that DEAs with silver nanowire electrodes show smaller actuations compared to the DEAs with CNT electrodes.[94]

Although it can be concluded that the effect of incomplete coverage is not presently significant since the elastomer thicknesses are usually tens of micrometers, it is likely to be of significance as substantially thinner elastomers are used in order to reduce the operating voltages. For instance, if the elastomer thickness is 1 μm, the relative capacitance drops to 44%–64% for surface coverage of 1%–10% (assuming that the spacing between the uncovered areas is of the order of the length of the CNTs, ~1 μm). The periodic arrangement of electrode strips is clearly a poor geometric description of a random, quasi-two-dimensional mat of CNTs, but unpublished results of simulations of an electrode containing a random arrangement of random sized circular holes indicate that the results for the periodic strips are nevertheless in reasonable agreement.

F. Self-cleaning and soft electrical breakdowns

The terms "soft breakdown" and "self-clearing"[127,128] come from the literature describing breakdown in gate electrodes, polymer capacitors, and electrical cables. Operationally, soft breakdown is characterized by the appearance of current spikes as the voltage is increased or held constant. As illustrated in Fig. 13,[71] numerous spikes can occur during the first few actuations without catastrophic breakdown and loss of functionality that occurs when the electrodes are shorted. Intriguingly, these current spikes do not reoccur after a few actuation cycles. The simplest explanation for soft breakdown is that a very high, localized current flows through the thickness of the dielectric destroying the material along the filamentary path by Joule heating, typically with the formation of various carbonaceous species. The observation that a device can continue to function suggests that the conducting filamentary channel either becomes isolated from the electrodes or there is sufficient flow of elastomer material from the surroundings to "heal" the channel. In high-performance density capacitors based on the biaxially-oriented polypropylene (BOPP) dielectric, the high energy dissipation associated with a current spike can lead to evaporation (or breakup) of the thin metal electrode surrounding the channel thereby insulating the channel from the current supply, shown schematically in Fig. 14(a) for single-layer capacitors and in Fig. 14(c) for multilayer capacitors.[128] Indeed, this is the basis for the "self-clearing" process used to proof test BOPP capacitors by systematically removing potential breakdown paths.

Early studies of self-clearing of thin metalized polymer films and capacitors[127,128] showed that the self-cleared areas of the electrodes are proportional to their sheet conductivity, $S_v \propto \sigma$, and therefore to the thickness of the electrodes, $S_v \propto t_e$. Furthermore, since the dissipated energy during a self-clearing event is proportional to the volume of the evaporated electrodes, $U \propto S_v t_e$, it varies with the square of the electrode thickness, $U \propto t_e^2$. Thinner and less conductive electrodes are, therefore, better suited for self-clearing, while thick electrodes will not self-clear and lead to premature electrical breakdown due to formation of a conducting channel, for instance, by the decomposition of the dielectric material. The same self-clearing isolation occurs when the electrodes consist of CNTs rather than a metal as a result of locally high

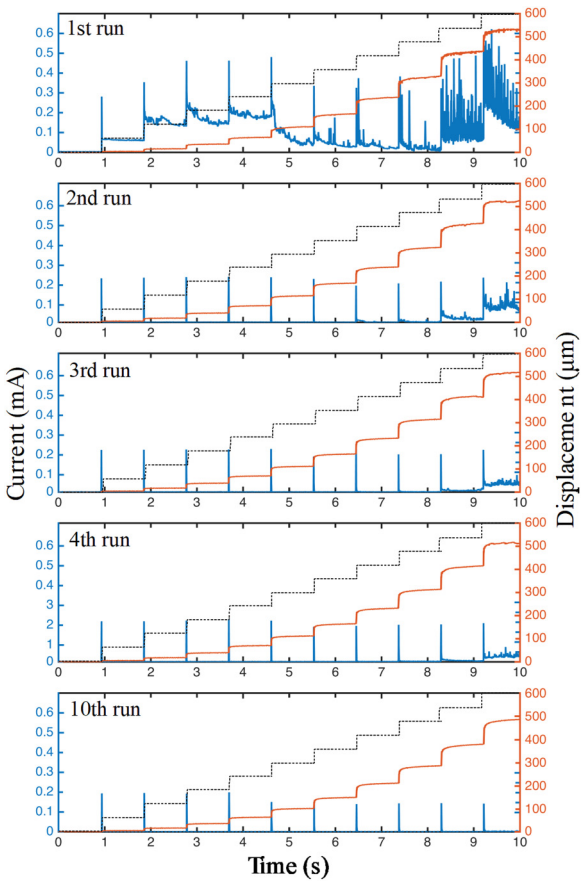

FIG. 13. Operationally, soft breakdown and self-clearing of CNT electrodes are characterized by the random appearance of current spikes during the first few runs (current as a function of time being shown in blue) as the voltage (black dotted curves) is increased stepwise, while the DEA keeps its actuation strain (orange curves) after each soft breakdown event. The self-clearing completes after a few runs and the spikes disappear.[71] The spikes that coincide with each voltage increase step, that are seen even in the later runs, correspond to the charging of the DEA. Reproduced with permission from Zhao *et al.*, Adv. Funct. Mater. **28**(42), 1804328 (2018). Copyright 2018 John Wiley and Sons.

current densities vaporizing (or oxidizing) the adjacent CNT electrode regions. The maximum current that an individual CNT can tolerate is ~19 μA.[129] For self-clearing to be effective, the areal concentration of CNTs cannot be too high; otherwise, there may be insufficient thermal energy to locally vaporize the CNT network, leaving some electrical continuity with the current supply and a current path through the dielectric. Photographs of the self-cleared spots of CNTs of dielectric elastomer actuators shows that the length scale of the self-cleared areas can be as large as millimeters, at least on a free surface [Fig. 14(b)].[130] Based on the estimates introduced in Sec. V E, such large areas will adversely affect the attainable actuation. This has yet to be evaluated.

In multilayer DEAs with CNT electrodes, the main difference is that the gaseous species formed during breakdown cannot escape

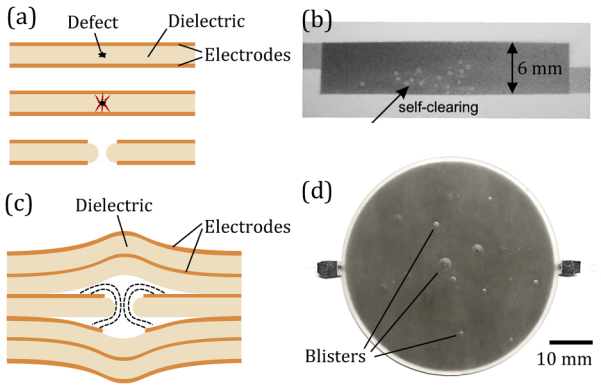

FIG. 14. Self-clearing of CNT electrodes on single-layer and multilayer DEAs. (a) Schematic of self-clearing of the electrodes around a weak spot on a single-layer polymer capacitors. (b) Photographs of a self-clearing of CNT electrodes on a single-layer silicone-based elastomer[130] shows that the self-cleared areas can be several mm^2 in size. Reproduced with permission from Stoyanov *et al.*, RSC Adv. **3**(7), 2272–2278 (2013). Copyright 2013 Royal Society of Chemistry. (c) Schematic of self-clearing and blister formation on a multilayer capacitor. The breakdown paths are shown by dashed lines. (d) Self-clearing in a multilayer acrylic-based DEA produces gaseous species that cannot escape and so form blisters.

and instead form blisters. For instance, Fig. 14(d) is a photograph of a multilayer acrylic-based DEA showing multiple blisters formed after several soft breakdown events, even while the actuator still functioned. (There is some evidence that the gases can diffuse out over time, particularly in silicones, and the blisters disappear, at least to the eye.) The literature on multilayer capacitors suggest that the carbon content of the gaseous species can significantly affect the effectiveness of the self-clearing process,[128] meaning that self-clearing in multilayer capacitors is not only determined by the electrode but also depends on the chemistry of the dielectric material. Indeed, it is not unusual in commercial polymer insulators to include additives to scavenge oxygen radicals, for instance.

In some elastomer actuators, soft breakdown together with self-clearing can significantly improve the electrical breakdown strength of DEAs and result in high-performance and fault-tolerant actuators.[70] In these instances, "self-clearing" acts to isolate breakdown paths that would otherwise lead to breakdowns at the lower side of the Weibull distribution thereby truncating the distribution, increasing the average breakdown strength and, if measured, increase the Weibull modulus. Similar proof testing has been used by Duduta[27] and Zhao[71] to improve electrical breakdown and reliability of multilayer DEAs. Key to successful proof testing is to slowly raise the voltage so that individual breakdown paths can be sequentially cleared without causing permanent catastrophic breakdown that shorts the electrodes.

Unresolved at the present time is the possibility that the CNTs or nanowires themselves and, in particular, their ends can act as local field concentrators. The basis for this is that nanowires and CNTs have very small diameters and the electric field varies as $1/r$ with radial distance, r, from a charged cylindrical conductor. The field concentration is even higher at the end of a cylindrical conductor if it is represented by the spherical cap.[131] Evidence suggesting that these geometrical effects can be important are observations of electric-field induced pitting in soft elastomers at the tip of a carbon fiber electrode lying on top of an elastomer film on an ITO coated glass. If the propensity for failure initiation at the ends of CNTs are borne out, then it would suggest that the electric breakdown field would increase with the length of the CNTs and that, ideally, electrodes should be fabricated from continuous CNTs

VI. ACTUATOR GEOMETRY

The parallel plate capacitor configuration forms the basis of several actuation geometries. The simplest being stacks of multilayers to generate a contractile displacement and tensile force in the electric field direction and a biaxial expansion and compressive force perpendicular to the field. This can be achieved through a layer-by-layer fabrication scheme,[11] folding an electrode coated thin elastomer layer back and forth,[9] or using a helical structures.[8] The tensile force can be used to lift a load in the stacking direction, whereas the compressive force acts orthogonally. Both the contractile displacement and the perpendicular compressive forces increase with the number of layers (at a constant total thickness and applied voltage) as described in Secs. II and III. This is an attractive proposition but places a premium on the manufacturing of multiple actuators and electrode layers having similar thicknesses and breakdown characteristics while avoiding defects. The biaxial actuation [e.g., the multilayer DEA in Fig. 1(c)] is akin to the contractile actuation of muscle tissues since the contractions in their length is associated with insignificant volume changes, less than 0.01%,[132] and their tensile properties are transversely isotropic,[133] which result in biaxial contractile actuations.

Biaxial actuators, however, are not common in engineering practice, which usually employs uniaxial actuators to apply a force or displacement in a specific direction. To meet this requirement, two modifications of the basic biaxial DEA have been utilized. One is to incorporate stiffening elements,[134] such as fibers or rings, to convert the biaxial expansion force into a tensile force that acts in a direction perpendicular to the stiffening elements. This configuration is analyzed in Sec. III C. The other is to wind the biaxial multilayer into a thick-wall cylinder, the elastomer layers being along the longitudinal axis and the azimuthal directions (Fig. 15), in which the friction or a glue between the layers prevents any expansion in the azimuthal direction converting the biaxial force produced by

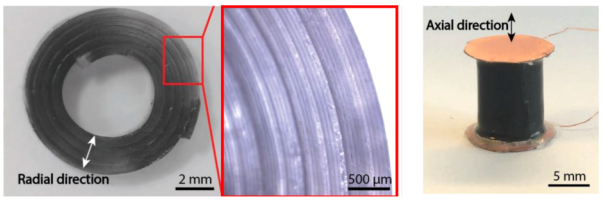

FIG. 15. Rolling of a multilayer DEA (left) forms compact cylindrical actuators (right) producing uniaxial actuations.[71] Reproduced with permission from Zhao *et al.*, Adv. Funct. Mater. **28**(42), 1804328 (2018). Copyright 2018 John Wiley and Sons.

the electric field into a force mainly acting along the axis of the cylinder.[71] This has found implementation in haptic devices[135] and flapping-wing robots (Fig. 16).[136] An important feature of the dielectric elastomer actuators is their impact resistance, analogous to the natural muscles. Recent work by Chen *et al.*[136] made use of this feature to create robust flapping-wing flying robots. The blocking forces of these compact cylindrical actuators were shown to remain unchanged over 0.5 kHz and the actuation displacement peaked at 0.5 kHz (Fig. 16), once again exceeding the performance of natural muscles shown in Fig. 1(d).[23]

The dynamic response of dielectric elastomers actuators depends on their geometry, the viscoelastic response of the elastomer material, and the response of the electrical drive circuit. It is often assumed that the bandwidth of the drive circuit, including the electrodes, is substantially larger than that of the elastomer, but this is not necessarily the case when using percolative CNT electrodes. For instance, if the electrode sheet resistance is of the order of ∼1 MΩ and the actuator capacitance is ∼1 nF, the electrical time constant, $\tau = RC$, is of the order of milliseconds. Furthermore, the resistance of percolative electrodes increases with stretch as does the capacitance, so during actuation the electrical time constant, $\tau = RC$, itself increases. Consequently, lowering the sheet resistance, without increasing the electrode stiffness, is essential for device operation up to and above 1 kHz.

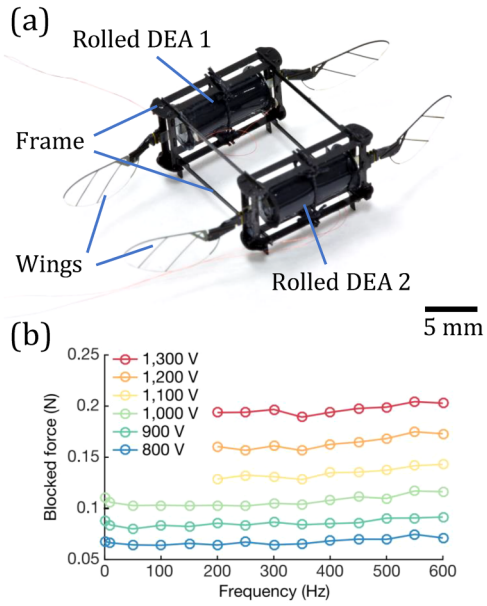

FIG. 16. Application of compact cylindrical DEAs for flapping-wing robots. Reproduced with permission from Chen *et al.*, Nature **575**(7782), 324–329 (2019). Copyright 2019 Springer Nature. (a) Photograph of a flapping-wing flying micro-robot using two compact cylindrical DEAs as impact resistant artificial muscles.[136] (b) The frequency response of the mesoscale silicone-based cylindrical DEA used in (a) shows that the blocking force remains unchanged up to 600 Hz, which significantly exceeds those of the mammalian skeletal muscles.

The simplicity of the cylindrical geometry actuator, consisting of concentric cylindrical layers, makes it well suited to fabrication in the laboratory as well as translation to large-scale manufacturing. For instance, they can be produced by successive dip-coating in elastomer and electrode solutions and curing[56] or by successive spray coating of the solutions onto a mandrel. Additionally, rolled DEAs can achieve multiple degrees of freedom by sectioning their electrode and addressing them separately.[137]

Advances in 3D printing have recently been utilized to create coaxial fibers and fiber bundle actuators.[138] Each fiber consists of an electrical conducting core, a sheath of dielectric, and an outer electrically conducting layer [Fig. 17(a)], similar to a standard coaxial cable except using compliant electrodes and a soft elastomer dielectric. The coaxial geometry creates a radial electric field in the dielectric, and to accommodate the incompressibility of the elastomer, the stresses in the fiber are purely hydrostatic. In response, when a voltage is applied, the fibers elongate and decrease in diameter. The axial actuation stretch is given by the relation

$$\lambda - \lambda^2 = \frac{\epsilon_0 \epsilon_r}{\mu R_3^2 \ln(R_2/R_1)}. \tag{35}$$

In contrast to the thin-walled cylindrical actuator, the solid core prevents the electromechanical instability so larger actuation strains are possible.[138]

The ability to print the fibers also facilitates the fabrication of hitherto unattainable shaped actuator designs, such as the micro-lattice structure [Fig. 17(c)] and possibly novel actuators. More significantly, fibers within a bundle can be individually addressed, akin to the innervation of natural muscle fascicles. In principle, this facilitates programmable and complex motions of the fiber bundles. As with all other

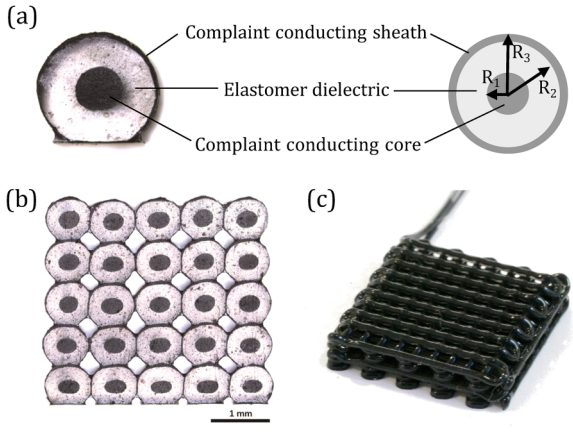

FIG. 17. 3D printing of coaxial dielectric elastomer fibers and actuators. (a) Micrograph (left) and schematic (right) of the cross section of a coaxial dielectric elastomer fiber consisting of the elastomer dielectric and the compliant conducting core and sheath. The dark center of each fiber is an elastomer containing nanocarbon particles to provide electrical conduction. The same conducting elastomer is used as the thinner, outer electrode. (b) Cross section of a 5×5 bundle of 3D-printed coaxial fiber actuators. (c) A 3D-printed micro-lattice structure using coaxial dielectric elastomer fibers.

designs of DEAs, one challenge with the 3D-printed coaxial fiber actuator is to reduce the elastomer layer thickness as well as the electrodes' thicknesses, in order to reduce their operating voltages. 3D printing poses additional processing challenges as both the dielectric and conductor materials must have matching rheological behavior so that both can be printed simultaneously and then subsequently cured to produce a uniform coaxial fiber geometry.

Multilayer and rolled DEAs that have been the focus of this section do not require any rigid frames, resulting in versatile functionalities and effortless integrations into soft machines. However, there are other important and well-developed DEAs that require rigid framing, such as diaphragm, bending, bistable, conical, and antagonistic DEAs. Diaphragm DEAs, such as the configuration shown in Fig. 1(a), consist of a prestretched layer of elastomer held onto a rigid frame with compliant electrodes deposited onto the two sides of the stretched elastomer. Applying voltage to the compliant electrodes expands the electroded areas reducing the prestretch of the surrounding elastomer. The result is in-plane actuations that can have used for applications such as thin rotary motors by sectioning the electrodes and addressing them sequentially[139] or tunable meta-lenses by bonding a meta-surface onto a DEA.[140] With a bias pressure, the diaphragm can be deformed out of plane and, in response to a voltage, deforms further in out-of-plane direction and changes curvature. The curvature change, in an antagonistic configuration, has been used for applications such as tunable lenses,[141] among other DEA-based tunable lenses.[142] Other bias forces such as those from compressed springs[143] or magnets[144] can also be used to deform the diaphragm. A particularly versatile configuration because it has six degrees of freedom for position and orientation is obtained by combining two cone DEAs, holding a stiff rod in the middle, and segmenting the electrodes[145] (Fig. 18). For instance, the rod can be moved in vertical or horizontal directions, respectively, if the electrodes on the top diaphragm or the left electrodes on both diaphragms are actuated [Figs. 18(b) and 18(c)]. To tilt the rod, the left electrodes on the top diaphragm and the right electrodes on the bottom diaphragm are actuated [Fig. 18(d)].

Bending actuators, discussed in Appendix A, are made of two layers of elastomer adhered to each other, one of which is coated on the two sides with compliant electrodes and expands when a voltage is applied, called the active layer, and the other resists the expansion, called the passive layer. The result is bending along one principal axis (and zero curvature along the second principal curvature). This has been used for applications such as grippers.[146]

VII. SHAPE-CHANGING DIELECTRIC ELASTOMERS

In the parallel plate capacitor configuration, the electric fields in the dielectric are spatially homogenous. This results in actuators that can homogeneously contract along field direction and expand in one or both perpendicular directions. In other words, the actuator only scales in its dimensions. Although such simple actuations are useful for various applications, such as applying a force in a single direction, more complex shape changes are also possible with dielectric elastomers. One simple approach is to break the

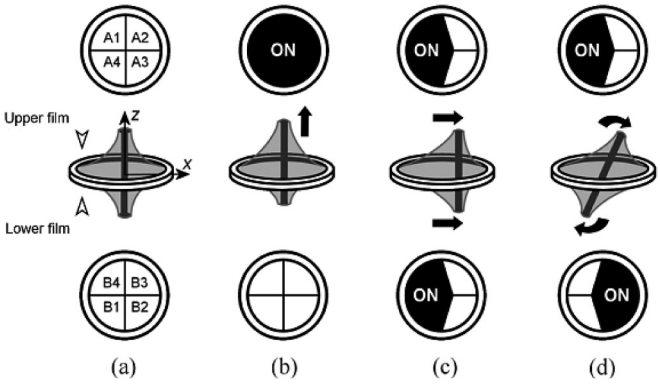

FIG. 18. Schematic of a six degree of freedom double-cone DEA attached to a circular frame with four, addressable segmented electrodes on each side.[145] Reproduced with permission from Conn and Rossiter, Smart Mater. Struct. **21** (3), 035012 (2012). Copyright 2012 IOP Publishing. (a) The actuator consists of two diaphragm DEAs that are pushed into a double-cone shape by a middle vertical rod, and the electrodes on both diaphragms are segmented into four parts, A1, A2, A3, and A4 on the top diaphragm and B1, B2, B3, and B4 on the bottom diaphragm. (b) Applying voltage to the electrodes of the top diaphragm displaces the rod in the +Z direction. (c) Applying voltage to the left electrodes of the two diaphragms, i.e., A1, A4, B1, and B4, moves the rod in the +X direction. (d) Actuating the left electrodes of the top diaphragm and right electrodes of the bottom diaphragm rotates the rod clockwise in the XZ plane.

symmetry along the thickness direction by adhering a passive layer of elastomer onto the DEA, which results in a bending actuator that can produce out of plane deformations.[146] This is analyzed in Appendix A. Although non-symmetric along the thickness direction, the electric field is homogeneous along the surface of the DEA, which results in bending along only one axis and zero curvature along the perpendicular axis. A double curvature requires an actuation that is inhomogeneous along the surface of the DEA. As a result, the Gaussian curvature of the bending actuator, which is the product of the two principal curvatures, remains zero. Since the shape of any surface is characterized by its local Gaussian curvatures, a generalizable shape-changing method must be able to produce locally controlled, nonzero Gaussian curvatures. To change the Gaussian curvature, the actuator must deform inhomogeneously along the surface, as implied by Gauss's Theorema Egregium.[147,148]

To produce controlled, spatially varying deformations in DEAs, several methods can be envisaged, two of which have been proven effective for shape-changing in dielectric elastomer actuators. One is to create a spatial variation of internal electric fields inside the elastomer[149] by the design of the electrodes on adjacent layers whose overlap determines the regions with nonzero electric fields. In essence, it is to create an embedded meso-architecture of the electrodes. The other is to control the local anisotropy of the DEA[150] by incorporating 3D-printed stiff fibers into the DEAs. Other methods that could also potentially result in controlled spatial variations of the actuation in DEAs are to control the shear modulus or the permittivity of the elastomer locally. These methods, however, are currently difficult to implement in practice

although half-tone lithography,[49] for instance, might be used to locally control the stiffness of single-layer elastomers. Recent advances in 3D printing of DEAs[151] also provide new opportunities for fabrication of shape-changing DEAs.

A. Shape-changing through spatial variation of internal electric field

To create spatial variations of the internal electric field,[149] the DEA is fabricated using a layer-by-layer scheme with different designs of the electrode geometries on each layer. Upon applying a voltage between the inter-digitated electrodes, an electric field is induced inside the elastomer layers, primarily in those regions where the adjacent electrodes overlap. This is perhaps better understood with the example shown in Fig. 19(a). In this example, the electrodes are a set of concentric circular disks whose diameters increase from the minimum on the top electrode to maximum on the bottom electrode. When a voltage is applied, all the elastomer layers at the center of the circular disk of the DEA will actuate but decreasing toward the edge of the DEA as the number of active, overlapping layers decreases to zero. Consequently, this geometry results in spatially varying lateral expansions that are larger at the center of the disk and smaller near its outer edge. To accommodate this incompatible actuation, the flat sheet of elastomer morphs into a dome-like shape with positive Gaussian curvature [Figs. 19(b) (top) and 19(c)]. The opposite geometry of overlap with a large lateral expansion near the edge and decreasing toward the center results in saddle-like shapes with negative Gaussian curvatures [Fig. 19(b) (bottom)].

A shape-changing DEA that uses the spatial variation of internal electric fields can be designed to morph into several fundamentally different actuation shapes, when different sets of electrodes are incorporated inside the DEA and addressed separately. The spatial distribution of the internal electric fields and actuation deformations depend on the set of the electrodes that are addressed. For instance, two sets of addressable electrodes were incorporated into the elastomer sheet to create the reconfigurable shape-morphing actuator shown in Fig. 19(d); one set of circular electrodes, as used to create a positive Gaussian curvature, and another set of electrodes, as used for the saddle shape, were positioned on alternate layers. Upon applying a voltage to the two sets of electrodes that correspond to the circular disk electrodes with varying radius, the elastomer morphs into a dome-like shape [Fig. 19(d) (left)], and applying voltage to the other set of electrodes results in a saddle-like shape [Fig. 19(d) (right)].

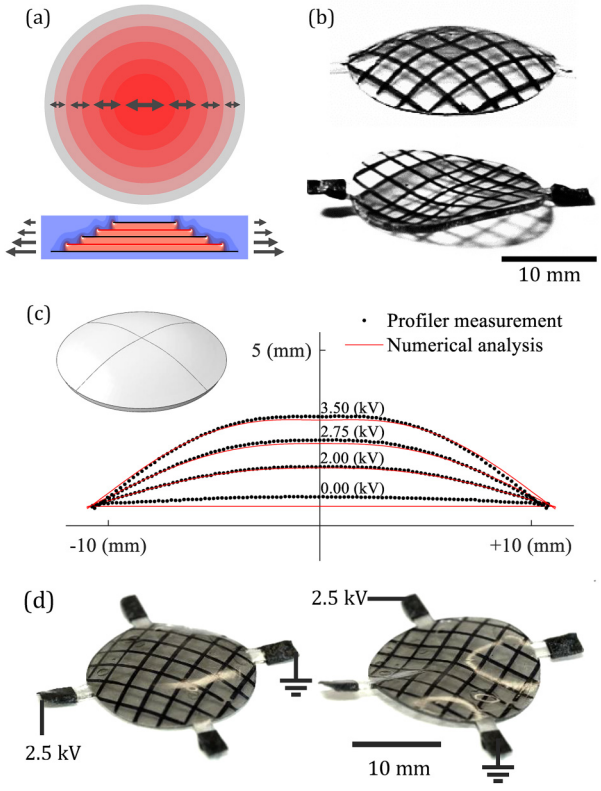

FIG. 19. Shape-changing dielectric elastomer actuators using spatial variation of internal electric fields.[149] Reproduced with permission from Hajiesmaili and Clarke, Nat. Commun. **10**, 183 (2019). Copyright 2019 Author(s), licensed under a Creative Commons Attribution (CC BY 4.0) license (a) An example of a shape-changing DEA in which the embedded inter-digitated electrodes are concentric circular disks, shown in red, with diameters varying with height. Applying a voltage to the inter-digitated electrodes creates electric fields mainly in the overlapping regions between the adjacent electrodes. The spatial variation of electric field results in an axisymmetric distribution of actuation strains. To accommodate the incompatible strain, the DEA morphs its shape, in this case into a dome-like shape with positive Gaussian curvatures. (b) Example of shape-changing DEAs designed to morph into dome-like shape with positive Gaussian curvature (top) and saddle-like shape with negative Gaussian curvature (bottom). (c) Finite element analysis of the dome-like DEA shown in (b) can accurately analyze the actuation shapes and displacements at different applied voltages. (d) A reconfigurable shape-changing DEA consisting of two sets of inter-digitated electrodes that are placed on alternating layers. The ones set correspond to dome-like shapes (left) and the others correspond to the saddle-like shape (right). The black lines are ink lines written on the surface to facilitate shape change measurements.

B. Shape-changing through spatial variation of anisotropy

The other method to achieve shape-changing DEAs is to create spatially varying anisotropy by incorporating 3D-printed fibers into the DEAs.[150] These fibers were selected so that they are much stiffer than the elastomer and constrain the deformation along the fiber, permitting only the actuations that are locally perpendicular to the fibers.[146] The inhomogeneity in isotropy can be used to create inhomogeneous deformations that result in shape-morphing. Figure 20(a) (top) shows the example of a multilayer DEA, with homogeneous internal electric field, onto which a set of concentric stiff rings are 3D-printed to create the spatial variation in anisotropy. Upon applying a voltage, the DEA morphs into a conical shape [Fig. 20(a) (bottom)]. Other examples of shape-changing DEAs are shown in Fig. 20(b), the actuation of which depends on the pattern of the 3D-printed stiff fibers. For example, in Fig. 20(b) (top), constraining the radial deformation of a DEA disk causes an "anti-cone" actuation shape.[152] Combining this method with the spatial variation

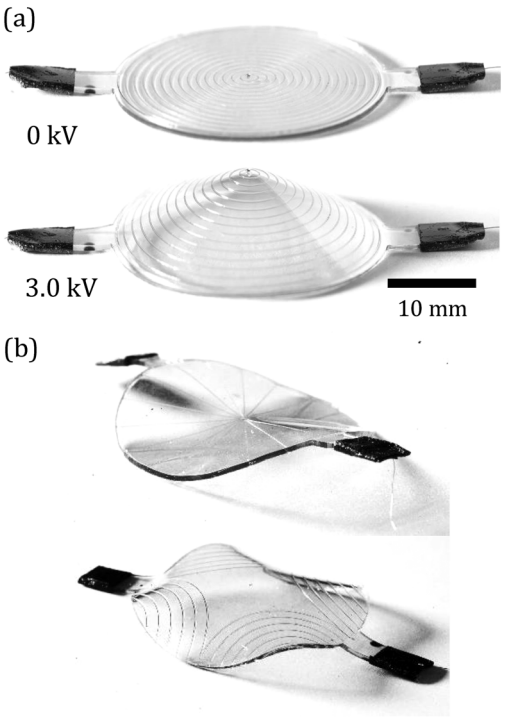

FIG. 20. Shape-changing DEAs using local control of anisotropy.[150] Reproduced with permission from Hajiesmaili *et al.*, Extreme Mech. Lett. **30**, 100504 (2019). Copyright 2019 Elsevier. (a) A circular multilayer DEA with a set of concentric circular stiff 3D-printed rings on top (top) morphs into a conical shape upon applying a voltage (bottom). (b) Two shape-morphing DEAs in which the actuation depends on the pattern of 3D-printed fibers. For example, constraining the radial deformation of the top actuator created an "anti-cone."

of the internal electric field can lead to a more powerful shape-changing actuation scheme in which not only the magnitude of the lateral stretch but also its direction is locally controlled.

C. Numerical analysis of shape-changing DEAs

Because of their complexity, the development of shape with voltage can only be predicted numerically. The following describes a finite elements formulation for the quasi-static fully coupled electromechanical actuations.[149,150,153] Based on this formulation, a User Element (UEL) subroutine was developed to be used with Abaqus/CAE. The UEL introduces the coupling between the electrostatics and mechanical deformations into the stiffness matrix and residual vectors of the finite element formulation. Abaqus/CAE is used to define the geometry of the dielectric elastomer, electrode designs and boundary conditions, and material model and parameters, and then solves the system of algebraic equations iteratively using the Newton–Raphson method.

For the finite element formulation, the partial differential equations of electrostatic and mechanical equilibrium are rewritten in the integral weak form that needs to be satisfied for any arbitrary weight function,

$$\begin{aligned}&\int_V \left(\frac{\partial \sigma_{ij}}{\partial x_i} + b_j\right) w_{1j} dV = 0, \ \forall w_{1j}, \ j = 1, 2, 3,\\ &\int_V \left(\frac{\partial D_i}{\partial x_i} - \rho_f\right) w_2 dV = 0, \ \forall w_2.\end{aligned} \tag{36}$$

It is straightforward to show that the partial differential form and the weak form are equivalent, simply by choosing the weight function to be $w_{1j} = \partial\sigma_{ij}/\partial x_i + b_j$ and $w_2 = \partial D_i/\partial x_i - \rho_f$. Using integration by parts, the integral weak form can be rewritten as

$$\begin{aligned}\begin{Bmatrix} R_{u_j} \\ R_\phi \end{Bmatrix} &= \begin{Bmatrix} \int_V \left(-\sigma_{ij}\frac{\partial w_{1j}}{\partial x_i} + b_j w_{1j}\right) dV + \int_S w_{1j} t_j dS \\ \int_V \left(-D_i \frac{\partial w_2}{\partial x_i} - \rho_f w_2\right) dV + \int_S w_2 q_s dS \end{Bmatrix} \\ &= \begin{Bmatrix} 0 \\ 0 \end{Bmatrix}, \quad j = 1, 2, 3.\end{aligned} \tag{37}$$

Two approximations are made for the finite element method. One is that instead of any arbitrary function for the weight functions, we choose the weight functions to have polynomial forms with arbitrary coefficients:

$$\begin{aligned}w_{1j}(\xi_1, \xi_2, \xi_3) &= N^A(\xi_1, \xi_2, \xi_3) w_{1j}^A, \quad \forall w_{1j}^A, \quad j = 1, 2, 3,\\ w_2(\xi_1, \xi_2, \xi_3) &= N^A(\xi_1, \xi_2, \xi_3) w_2^A, \quad \forall w_2^A,\end{aligned} \tag{38}$$

where ξ_1, ξ_2, and ξ_3 are the local element coordinates, N^A is the Ath polynomial, and w_{1j}^A and w_2^A are any arbitrary coefficients. The second approximation is that the solution variables $u_k(\xi_1, \xi_2, \xi_3) = X_k(\xi_1, \xi_2, \xi_3) - x_k(\xi_1, \xi_2, \xi_3)$ and $\phi(\xi_1, \xi_2, \xi_3)$ are also assumed to have polynomial forms but with unknown coefficients, instead of being any arbitrary function,

$$\begin{aligned}u_k(\xi_1, \xi_2, \xi_3) &= N^B(\xi_1, \xi_2, \xi_3) u_k^B,\\ \phi(\xi_1, \xi_2, \xi_3) &= N^B(\xi_1, \xi_2, \xi_3) \phi^B.\end{aligned} \tag{39}$$

Using these two approximations with the integral weak form, the four partial differential equations of electrostatic and mechanical equilibrium in three dimensions are converted into a set of $4N$ nonlinear algebraic equations, where N is the number of nodes and is the same as the number of polynomials in the approximation of the solution variables,

$$\begin{aligned}\begin{Bmatrix} R_{u_j}^A \\ R_\phi^A \end{Bmatrix} &= \begin{Bmatrix} \sum_{n_G}\left(-\sigma_{ij}\frac{\partial N^A}{\partial x_i} + b_j N^A\right) w_{n_G} \det\frac{\partial x_p}{\partial \xi_q} + \sum_{n_G}(t_j N^A) w_{n_G} \det\frac{\partial x_p}{\partial \xi_q} \\ \sum_{n_G}\left(-D_i\frac{\partial N^A}{\partial x_i} - \rho_f N^A\right) w_{n_G} \det\frac{\partial x_p}{\partial \xi_q} + \sum_{n_G}(q_s N^A) w_{n_G} \det\frac{\partial x_p}{\partial \xi_q} \end{Bmatrix} \\ &= \begin{Bmatrix} 0 \\ 0 \end{Bmatrix},\end{aligned} \tag{40}$$

with $A = 1, \ldots, N$. This system of nonlinear partial differential equations is solved numerically using the Newton–Raphson method,

$$\begin{Bmatrix} R^A_{u_j} \\ R^A_{\phi} \end{Bmatrix}^{i+1} = \begin{Bmatrix} R^A_{u_j} \\ R^A_{\phi} \end{Bmatrix}^{i} + \frac{\partial}{\partial u^B_k} \begin{Bmatrix} R^A_{u_j} \\ R^A_{\phi} \end{Bmatrix}^{i} \delta u^B_k + \frac{\partial}{\partial \phi^B} \begin{Bmatrix} R^A_{u_j} \\ R^A_{\phi} \end{Bmatrix}^{i}$$

$$\delta\phi^B = \begin{Bmatrix} 0 \\ 0 \end{Bmatrix}, \quad j = 1, 2, 3, \quad A = 1, \ldots, N$$

$$\rightarrow -\frac{\partial}{\partial u^B_k} \begin{Bmatrix} R^A_{u_j} \\ R^A_{\phi} \end{Bmatrix} \delta u^B_k - \frac{\partial}{\partial \phi^B} \begin{Bmatrix} R^A_{u_j} \\ R^A_{\phi} \end{Bmatrix} \delta\phi^B = \begin{Bmatrix} R^A_{u_j} \\ R^A_{\phi} \end{Bmatrix},$$

$$j = 1, 2, 3, \quad A = 1, \ldots, N, \tag{41}$$

where the superscripts $i+1$ and i are the iteration numbers. Therefore,

$$\begin{bmatrix} K_{u^A_j u^B_k} & K_{u^A_j \phi^B} \\ K_{\phi^A u^B_k} & K_{\phi^A \phi^B} \end{bmatrix} \begin{Bmatrix} \delta u^B_k \\ \delta\phi^B \end{Bmatrix} = \begin{Bmatrix} R^A_{u_j} \\ R^A_{\phi} \end{Bmatrix}, \; j = 1, 2, 3, \; A = 1, \ldots, N. \tag{42}$$

Successive iterations are continued until the changes in the solution variables and the absolute value of the largest element of the right-hand-side residual vector are smaller than some predefined tolerance values. Based on this formulation, an Abaqus User Element (UEL) subroutine adds the Maxwell stress contributions to the mechanical residual vector and the coupling terms $K_{u^A_j \phi^B}$ and $K_{\phi^A u^B_k}$ to the stiffness matrix. The finite element code, with an accompanying tutorial of using it within the finite element commercial program Abaqus, is presented in the supplementary material. The finite element formulation and the accompanying code are not only able to analyze the actuation shapes of the shape-morphing DEAs qualitatively [the insert in Fig. 19(c)] but also prove to accurately describe the actuation shapes and displacements shown in Fig. 19(c).

VIII. FUTURE PROSPECTS

Significant improvements in DEAs' actuation forces, displacements, reliability, and functionality can be anticipated based on the properties and issues discussed in this Tutorial. Although these may not require an improved understanding of the detailed physics involved, there are clear benefits from a deeper understanding of phenomena such as electrical breakdown and charge injection in soft disordered materials where the electrical energies are comparable to the deformation energies.

One major area of improvement is likely to be the development of elastomers specifically designed for high-field actuator applications. Existing elastomers have been designed for very different applications, such as for sealing gaps, adhesive applications, or as potting materials. Improved high-field elastomers can be anticipated to be purer, contain a lower concentration of non-network polymers, and have additives designed for specific purposes such as getters to absorb mobile radicals produced under very high local electric fields. Together, it is expected that these will lead to greater reproducibility and higher electric breakdown strength elastomers. In addition, one can also anticipate that by careful control of the network molecular weight, a variety of chemically similar elastomers can be tailored to produce desired combinations of blocking force and actuation displacements.

Two other areas of elastomer research can also be expected to lead to further improvements in capabilities of DEAs. One is to incorporate conducting molecules in the elastomer to form compliant electrodes to replace current CNT electrodes, improving electrode homogeneity and actuator reliability. This is a major challenge since conducting molecules are very stiff and do not exhibit the flexible network forming characteristics of elastomers. Nevertheless, the development of liquid crystal elastomers suggests that it is possible to incorporate stiff molecules into elastomers without compromising their flexibility. The second is the development of higher permittivity elastomers, whether by adding polarizable groups to the polymer chains or the incorporation of high-permittivity second phase particles. As described in Sec. IV E, to be beneficial for device operation, the increase in permittivity must outweigh the possible decrease in breakdown strength and increase in stiffness that has so far limited the success of this approach.

DEAs currently operate at high voltages (1–5 kV) because current processing methods limit the minimum uniform thickness of elastomers that can be reproducibly fabricated. While these high voltages do not pose a safety issue provided the current is limited,[154] it would be desirable to operate at substantially lower voltages to take advantage of the availability of existing low voltage circuits and also to avoid having to operate high-voltage circuits in parallel with low voltage ones. Substantial progress to achieving lower voltages has been made by combining processing methods more suited to producing thin elastomer layers (e.g., 3 μm[57]) with more controlled deposition of CNTs, such as the Langmuir–Blodgett method. New questions will then arise as to the effects of charge uniformity, attainable capacitance, and the possible role of charge injection and preferential breakdown from the ends of the CNTs. For instance, the 7.5% maximum lateral strain that a 3 μm thin pad-printed DEA shows at 245 V[57] is nearly half of the maximum actuation that a 30 μm thick DEA made of the same material can achieve, due to the higher ratio of electrodes' to elastomer's thickness for the 3 μm DEA and, potentially, lower tolerance for electrode and surface inhomogeneities. Nevertheless, it is likely that the major impediment to lower voltage operation will primarily be the wide variability in breakdown fields caused by fabrication defects, such as bubbles and dust. Consequently, operation at high voltages together with "proof testing"[71] is the most straightforward way of dealing with the poor reproducibility of currently produced devices.

Multiple layer stacks of elastomers and electrodes are likely to be the basis of all actuators because of the larger forces that can be generated as well as for ease of handling. Multilayered structures allow for structural improvements to the DEAs' performance. For instance, depositing strain-stiffening elastomers onto the two sides of each soft elastomer layers can help with preventing electromechanical and local instabilities. Including high-breakdown layers such as hexagonal boron nitride layers can result in DEAs with higher electrical breakdown strength. Scalable fabrication of multilayer devices will require the development of

reel-to-reel manufacturing and in clean-room conditions to avoid dust and other impurities. The availability of prefabricated multilayers would also speed up technology innovation, much as the availability of resin impregnated carbon fibers pre-forms enabled broad applications of carbon fiber composites. UV curing is faster than thermal curing and hence more suited for multilayers and large-scale fabrication. However, it remains to be seen whether chemical defects introduced by UV curing affect long-term aging under high fields.

At the system level, two areas of improvement for the control circuitry of the DEAs can be expected. One is to incorporate miniaturized and integrated high-voltage switches into the DEAs for reprogrammable local control of their actuations. The other is methods and electronics for charge recovery to realize the high energy efficiency of DEAs. Intrinsically, the low electric currents that DEAs consume (typically less than one up to a few milliamps) leads to high energy efficiencies at low frequencies with insignificant joule heating, but high efficiencies can only be achieved if the stored charges during the discharge of the DEAs can be reused. Additionally, for untethered DEA robots, energy storage at high voltages, e.g., using high-voltage capacitors as opposed to 5 V batteries with lossy DC–DC converters, may be an advantage.

The continuing improvements of elastomers, their processing, and their control circuitry are expected to lead to improved actuator designs. Developing design tools that enable morphing into predefined target shapes together with improved actuation displacements, forces, and reliability will result in novel devices such as shape-morphing airfoils and adaptive optical lenses and mirrors. Furthermore, the use of liquid crystal elastomers opens up the possibility of directional properties, enhancing DEAs' performance and allowing for even more complex shape-morphing. By incorporating miniaturized high-voltage soft switches, fully reprogrammable shape-morphing DEAs can be realized, resulting in highly versatile soft machines. The revolution that integrated circuits and liquid crystal displays created in electronics industry could be repeated for mechanical devices using high-performance reprogrammable shape-morphing DEAs.

SUPPLEMENTARY MATERIAL

See the supplementary material for demonstrations of DEA artificial muscles, birefringence of dielectric elastomers under mechanical loadings and electrostatic actuations, flight of flapping-wing micro-robots powered by DEAs, and shape-morphing of DEAs with spatial variations of internal electric field and anisotropy, as well as the finite element codes for analysis of complex DEAs:

Supplementary video S1. A multilayer acrylic-based dielectric elastomer actuator, weighing ~20 g, lifting a 1 kg weight. The video demonstrates utilization of a stack of multilayer dielectric elastomer actuators as an artificial muscle on a real-size plastic skeleton. Adopted from Duduta *et al.*, Proc. Natl. Acad. Sci. U.S.A. **116**(7), 2476–2481 (2019). Copyright 2019, published under the PNAS license.

Supplementary video S2. Birefringence of a strip of an acrylic-based, multilayered dielectric elastomer under uniaxial mechanical stretch, demonstrated by the color change of the elastomer, placed between two parallel polarizers with their axis at 45° with respect to the birefringence axis of the elastomer and illuminated by a background white light source. At one stage, as the multilayer strip is stretched, the outer layer of elastomer breaks and progressively delaminates, followed by rupture of the entire elastomer strip.

Supplementary video S3. Birefringence of a dielectric elastomer actuator with comb-like electrode geometries under electric field induced deformations, demonstrated by the color change of the actuator, placed between two parallel polarizers with their axis at 45° with respect to the birefringence axis of the elastomer and illuminated by a background white light source. The blisters, arrowed, formed under applied voltages are the products of soft breakdowns of the multilayer actuator. The actuator remains operational even after multiple soft breakdowns and blister formations.

Supplementary video S4. Flapping-wing micro-robots, each with two dielectric elastomer actuators, showing impact resistance and robustness under in-flight collisions. Adopted from Chen *et al.*, Nature **575**(7782), 324–329 (2019). Copyright 2019 Springer Nature.

Supplementary video S5. Demonstration of a reconfigurable shape-morphing dielectric elastomer actuator. The actuator consists of two sets of embedded electrodes placed on alternating layers. The first set of electrodes corresponds to morphing into dome-like shapes and consists of concentric circular disks of inter-digitated ground and high-voltage electrodes with linearly increasing diameters from the bottom layer to the top layer. The second set of electrodes correspond to morphing into saddle-like shapes, having zero active layer at the center of the disk and linearly increasing with radius to the maximum number of active layers around the edge. The shape-morphing is determined by the addressed set of electrodes. Reproduced with permission from Hajiesmaili and Clarke, Nat. Commun. **10**, 183 (2019). Copyright 2019 Author(s), licensed under a Creative Commons Attribution (CC BY 4.0) license.

Supplementary video S6. Actuation of a shape-morphing dielectric elastomer actuator with spatially varying anisotropy, using 3D-printed circular rings of stiff elastomers on the bottom of the actuator. The actuation shapes for this design of the stiff elastomers are cone shapes. Adopted from Hajiesmaili *et al.*, Extreme Mech. Lett. **30**, 100504 (2019). Copyright 2019 Elsevier.

Supplementary codes: The Abaqus user element subroutine (static.f) for finite element analysis of DEAs, together with an auxiliary run code (run.py) and a brief user guide on how to use the codes are provided.

ACKNOWLEDGMENTS

We are grateful for extensive discussions with several colleagues during the preparation of this contribution as well as allowing us to use illustrations from their research, including Kezi Cheng, Kevin Chen, Alex Chortos, Mishu Dutta, Rico Felber, Matthias Kollosche, Jie Mao, Samuel Shian, and Robert Wood.

This research was primarily supported by the NSF through the Harvard University Materials Research Science and Engineering Center (No. DMR-2011754).

APPENDIX A: BILAYER BENDING DIELECTRIC ELASTOMER ACTUATORS

Dielectric elastomer actuators can produce large out of plane actuations if the actuator is designed to have inhomogeneities in either lateral or through-thickness directions. The simplest are bilayer bending actuators that consist of a homogeneous active layer of dielectric elastomer coated with compliant electrodes, attached to a homogeneous passive layer of elastomer, as shown in Fig. 21(a). The actuation is inhomogeneous in through-thickness direction, but homogeneous laterally. When a voltage is applied to the electrodes, the lateral expansion of the active layer is constrained by the passive layer causing the out of plane bending actuation.

For the deformation mapping function of the bilayer bending actuators, it can be assumed that the actuator bends into a thick-wall cylindrical shape. This is based on two assumptions: one is the Kirchhoff–Love plate theory that considers the straight lines normal to the plate's mid-surface to remain straight and normal to the mid-surface after the deformation. The other assumption is that the second principal curvature is zero, since the actuation is expected to be homogeneous in lateral directions. Therefore, the

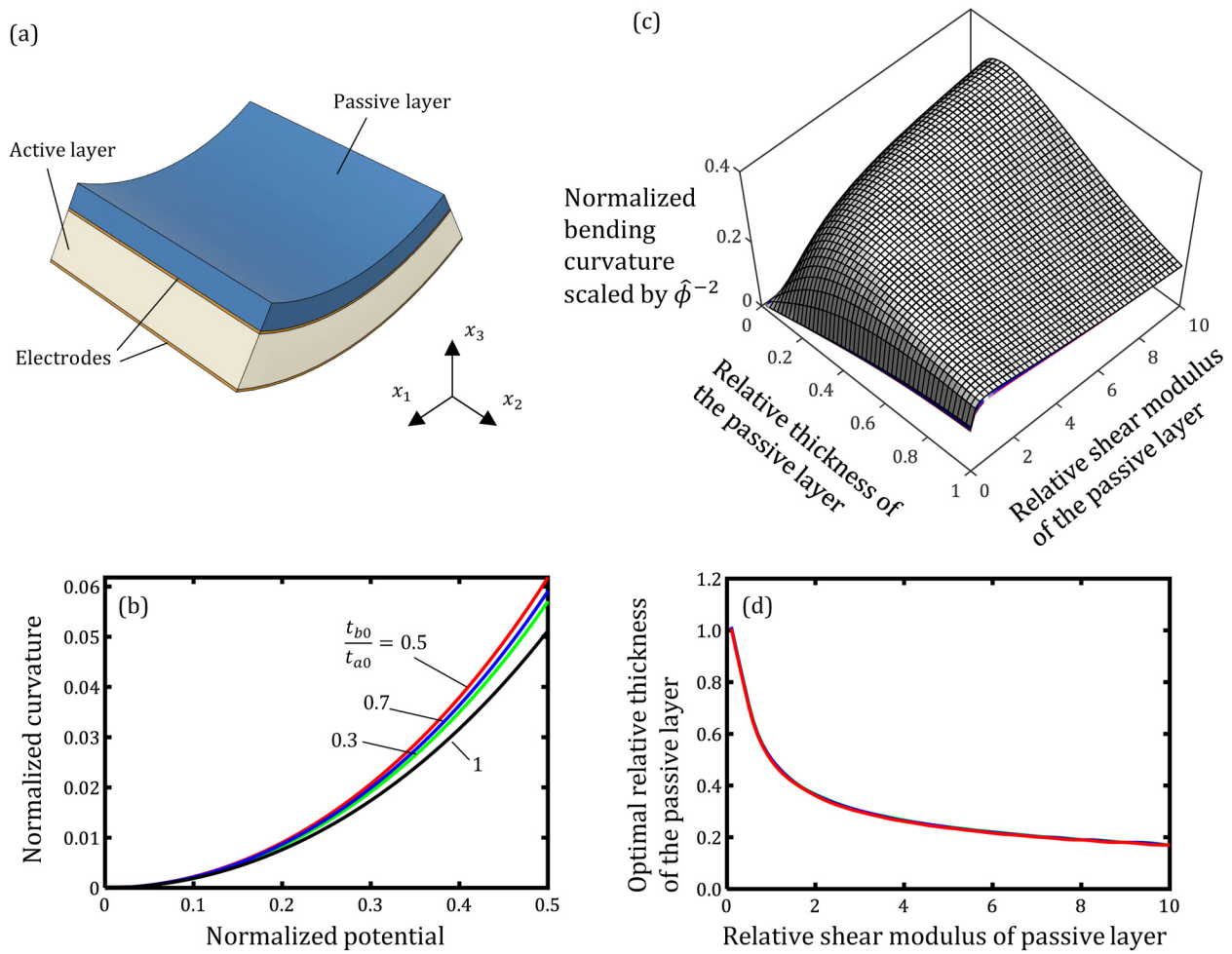

FIG. 21. Bilayer bending dielectric elastomer actuators. (a) Schematic of a bilayer bending DEA consisting of an active layer sandwiched between two compliant capacitors and a passive layer adhered, bended along an axis under an applied voltage. (b) The curvature of bending as a function of the normalized electric potential, $\hat{\phi} = \sqrt{\epsilon/\mu_a}\phi/t_{a0}$, for different rations of passive to active layer thicknesses. (c) Bending curvature normalized by the thickness of the active layer, t_{a0}/R, as a function of the two design parameters of the bending actuators, i.e., relative thickness and shear modulus of the passive layer. The normalized curvature is scaled by the inverse square of the normalized electric potential and plotted for $\hat{\phi} = 0.1$, 0.3, and 0.5, which nearly overlap. (d) The optimum relative thickness of the passive layer for a given relative shear modulus is the ridge of the 3D plot in (c).

deformation mapping function can be written as

$$x_1 = r\sin(\theta),\ \ x_2 = \lambda_2 X_2,\ \ x_3 = R - r\cos(\theta), \tag{A1}$$

where $r = R - \lambda_3(X_3)X_3$ and $\theta = \lambda_1 X_1/R$. R is the radius of curvature and the function $\lambda_3(X_3)$ accounts for the change in thickness of the elastomer layers. and it would have been $\lambda_3(X_3) = 1$ if there was no change in thickness as is often the case with the Kirchhoff–Love plate theory. Using the mapping function $x_i(X_1, X_2, X_3)$, the deformation gradient tensor and the left Cauchy–Green deformation tensor are calculated to find the first and third invariants. For an incompressible material, the third invariant does not change during the deformation allowing $\lambda_3(X_3)$ to be determined,

$$I_3 = \det \boldsymbol{B} = 1 \rightarrow \frac{\lambda_1^2\lambda_2^2(R - \lambda_3(X_3))^2\lambda_3'(X_3)^2}{R^2} = 1. \tag{A2}$$

This ordinary differential equation can be solved for $\lambda_3(X_3)$ and the solution is chosen such that $\lambda_3 = 1/\lambda_1\lambda_2$ for $X_3 \rightarrow 0$ and $\lambda_3(X_3) \rightarrow 1$ when $R \rightarrow \infty$, $\lambda_1 \rightarrow 1$, and $\lambda_2 \rightarrow 1$,

$$\lambda_3(X_3) = \frac{R}{X_3}\left(1 - \sqrt{1 - \frac{2X_3}{\lambda_1\lambda_2 R}}\right). \tag{A3}$$

Using $\lambda_3(X_3)$, the first invariant of the Cauchy–Green deformation tensors can be evaluated as

$$I_1 = \mathrm{tr}\boldsymbol{B} = \frac{4X_3^2\lambda_1^2 - 2RX_3\lambda_1\lambda_2(2\lambda_1^2 + \lambda_2^2) + R^2(1 + \lambda_1^4\lambda_2^2 + \lambda_1^2\lambda_2^4)}{R\lambda_1\lambda_2(-2X_3 + R\lambda_1\lambda_2)}. \tag{A4}$$

The fact that the first invariant and, therefore, the Helmholtz free energy is independent of the lateral positions, X_1 and X_2, confirms that the choice of cylindrical actuation shape satisfies the lateral homogeneity of the actuation. The strain energy of the system can be calculated as

$$\begin{aligned} U_{\text{strain}} &= l_0^2\int_0^{t_{a0}}\frac{\mu_a}{2}(I_1(X_3) - 3)dX_3 + l_0^2\int_{t_{a0}}^{t_{a0}+t_{b0}}\frac{\mu_b}{2}(I_1(X_3) - 3)dX_3 \\ &= \frac{\mu_a l_0^2 t_{a0}}{R/t_{a0}}\left(-\frac{\lambda_1}{2\lambda_2} + \frac{R}{2t_{a0}}(-3 + \lambda_1^2 + \lambda_2^2) - \frac{R^2}{4t_{a0}^2\lambda_1\lambda_2}\log\left[1 - \frac{2}{\lambda_1\lambda_2 R/t_{a0}}\right]\right. \\ &\quad \left. + \frac{\mu_b}{\mu_a}\left(-\frac{t_{b0}\lambda_1}{t_{a0}\lambda_2} + \frac{t_{b0}}{t_{a0}}\left(-\frac{\lambda_1}{2\lambda_2} + \frac{R}{2t_{a0}}(-3 + \lambda_1^2 + \lambda_2^2)\right) - \frac{R^2}{4t_{a0}^2\lambda_1\lambda_2}\log\left[1 - \frac{2t_{b0}/t_{a0}}{\lambda_1\lambda_2 R/t_{a0} - 2}\right]\right)\right). \end{aligned} \tag{A5}$$

The electrostatic energy of the whole system is

$$U_{\text{electric}} = -\frac{1}{2}C\phi^2 = -\frac{\epsilon\lambda_1 l_0^2\phi^2}{2R\log\left(\frac{R}{R - \lambda_3(t_{a0})t_{a0}}\right)}. \tag{A6}$$

The solution for the actuation parameters λ_1, λ_2, and R can be calculated from the minimization of the total energy, $U_{\text{total}} = U_{\text{strain}} + U_{\text{electric}}$, which occurs when

$$\frac{\partial U_{\text{total}}}{\partial\lambda_1} = 0,\quad \frac{\partial U_{\text{total}}}{\partial\lambda_2} = 0,\quad \frac{\partial U_{\text{total}}}{\partial R} = 0. \tag{A7}$$

These three nonlinear algebraic equations can be solved numerically for any given normalized voltage $\sqrt{\epsilon/\mu_a}\phi/t_{a0}$ and normalized thickness and shear modulus of the passive layer t_{b0}/t_{a0} and μ_b/μ_a. Figure 21(b) shows the normalized curvature t_{a0}/R of four bilayer actuators with different normalized thicknesses of the passive layer, as a function of the normalized voltage, indicating that the normalized curvature scales with the square of the normalized voltage, to the first degree. When the active and passive layers are made of the same material, $\mu_a = \mu_b$, the maximum normalized curvature is achieved with the thickness of the passive layer being half of that of the active layer, as shown in Fig. 21(b). To explore the optimal designs of the bilayer actuators that can achieve maximum normalized curvatures, Fig. 21(c) shows the normalized curvature scaled by $\hat{\phi}^{-2}$, for different design parameters of the normalized thickness and shear modulus of the passive layer, t_{b0}/t_{a0} and μ_b/μ_a, and at different normalized voltages. The graph shows that larger normalized curvatures can be achieved if stiffer passive layers with optimal thicknesses are used.

APPENDIX B: FABRICATION PROCEDURE OF CNT ELECTRODES

A simple recipe to form thin films of percolating networks of carbon nanotubes on elastomer sheets is described below, which is one of the many variations of the original techniques[99–101] for fabrication of thin film carbon nanotube electrodes.

1. 100 mg of carbon nanotubes functionalized with carboxylic acid (P3-SWNT, outer diameter of individual or bundles 1–5 nm,

length 1 ± 0.5 μm, Carbon Solutions, Inc.) is added to 200 ml of de-ionized water in a 200 ml glass beaker.
2. To exfoliate carbon nanotubes from the large bundles, the mixture is ultrasonicated using a probe sonicator at 300 W power for 10 min. A Branson 450 Digital Sonifier attached to a 0.5 in. tapped stepped disruptor horn through a 102C convertor is used and set to 75% power with intervals of 5 s on and 5 s off for a total duration of 20 min.
3. To sediment the remaining large bundles, the ultrasonicated dispersion is then transferred to 50 ml centrifuge tubes and centrifuged for 1 h at 8000 rpm (Sorvall Primo Centrifuge, Thermo Fisher Scientific, Waltham, MA).
4. A stable suspension is obtained by decanting the top three-fourth supernatant of the dispersion and disposing the remaining. Typical concentration of the carbon nanotubes in the decanted dispersion is 0.2 mg/ml, or 0.02 wt. %, measured through thermogravimetric analysis (TGA Q5000, TA Instruments, New Castle, DE).
5. To provide a reference for the concentration of carbon nanotubes, the dispersion can then be diluted with de-ionized water to 17% transmittance at 550 nm wavelength, for which the concentration of carbon nanotubes is 15 μg/ml. Figure 22 shows the transmittance of the suspension of CNTs as a function of the concentration. The transmittance is measured through a path length of 10 mm (Standard-Sized 3.5 ml glass cuvettes, EW-83301-03, Cole-Parmer, Vernon Hills, IL) using USB650 Red Tide Spectrometer (Ocean Optics, New Port Richey, FL), and calibrated with the cuvette filled with de-ionized water as the 100% transmittance.
6. To form a thin film of percolating network of carbon nanotubes, the diluted solution is vacuum filtered through a porous filter membrane whose pores are smaller than the length of the carbon nanotubes and its surface energy is high so that the carbon nanotube film can be easily stamped onto an elastomer. To form a circular disk of thin film carbon nanotubes with diameter of 35 mm and carbon nanotubes with areal density of 1.3 μg/cm^2 onto the filter, 500 μl of the diluted solution is further diluted with isopropanol and vacuum filtered through hydrophobic polytetrafluoroethylene (PTFE) filter membrane with 0.2 μm pore size and 47 mm diameter (T020A047A, Advantec, Dublin, CA) placed onto a supporting filter paper (Whatman 1004-042, GE Healthcare Life Sciences, Chicago, IL) and mounted onto a vacuum filter holder set with fritted glass support base (FHFT47, United Scientific Supplies, Inc., Waukegan, IL) whose circular opening is 35 mm in diameter. To form a larger thin film circular disk of carbon nanotubes with diameter of 70 mm and the same carbon nanotubes with areal density of 1.3 μg/cm^2, 2 ml of the diluted solution is vacuum filtered through a hydrophobic PTFE filter membrane with 0.2 μm pore size and 90 mm diameter (T020A090C, Advantec, Dublin, CA) placed onto a supporting filter paper (Whatman 1004-090, GE Healthcare Life Sciences, Chicago, IL) and mounted onto a vacuum filter holder set with fritted glass support base (FHSS90, United Scientific Supplies, Inc., Waukegan, IL) whose circular opening is 70 mm in diameter.
7. The compliant electrode of percolating networks of carbon nanotube is formed onto the elastomer by stamping the filter onto the elastomer sheet through a mask that defines the two-dimensional geometry of the electrode. Masks are cut from a clear silicone release film (CRP41082, Drytac, Richmond, VA) using either a low-cost desktop cutting machine (Silhouette Cameo, Silhouette America, Inc., Lindon, Utah) or a laser cutting machine.

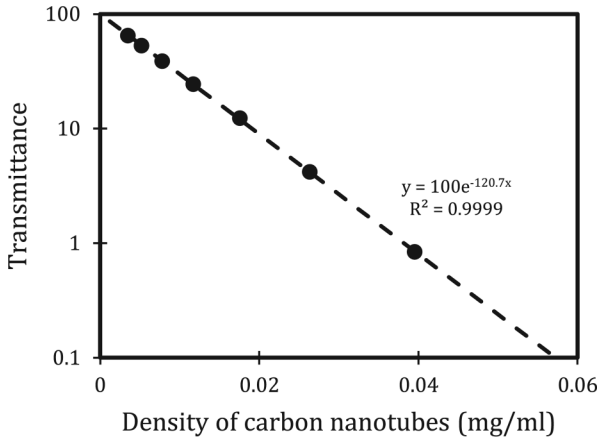

FIG. 22. Optical transmittance at 550 nm of a dispersion of CNTs in de-ionized water as a function of the concentration of CNTs, measured through a 10 mm path length.

The sheet conductivity in Fig. 10 is measured by the four-point probe method[155] using a Keithley 6221 current source and Keithley 2182A Nanovoltmeter. To show the effectiveness of transferring the CNT film by stamping, the sheet conductivity in Fig. 10(a) was measured for both the CNT film on the PTFE filter and after stamping onto a silicone elastomer with high surface tension (Sylgard 184 with stoichiometric ratio of 10:1 Part A to Part B cured for 30 min at 70 °C).

DATA AVAILABILITY

The data that support the findings of this study are available from the corresponding author upon reasonable request.

REFERENCES

[1]T. Mirfakhrai, J. D. W. Madden, and R. H. Baughman, "Polymer artificial muscles," Mater. Today **10**(4), 30–38 (2007).
[2]R. Pelrine *et al.*, "High-speed electrically actuated elastomers with strain greater than 100%," Science **287**(5454), 836–839 (2000).
[3]R. Pelrine *et al.*, "Dielectric elastomer artificial muscle actuators toward biomimetic motion," in *Smart Structures and Materials 2002 Electroactive Polymer Actuators and Devices (EAPAD)* (International Society for Optics and Photonics, 2002).
[4]K. H. Stark and C. G. Garton, "Electric strength of irradiated polythene," Nature **176**(4495), 1225–1226 (1955).
[5]X. Zhao and Z. Suo, "Method to analyze electromechanical stability of dielectric elastomers," Appl. Phys. Lett. **91**(6), 061921 (2007).
[6]Z. Suo, "Theory of dielectric elastomers," Acta Mech. Solida Sin. **23**(6), 549–578 (2010).

[7]S. J. A. Koh *et al.*, "Mechanisms of large actuation strain in dielectric elastomers," J. Polym. Sci., Part B: Polym. Phys. **49**(7), 504–515 (2011).
[8]F. Carpi *et al.*, "Helical dielectric elastomer actuators," Smart Mater. Struct. **14**(6), 1210–1216 (2005).
[9]F. Carpi, C. Salaris, and D. De Rossi, "Folded dielectric elastomer actuators," Smart Mater. Struct. **16**(2), S300–S305 (2007).
[10]O. A. Araromi *et al.*, "Spray deposited multilayered dielectric elastomer actuators," Sens. Actuators, A **167**(2), 459–467 (2011).
[11]M. Duduta, R. J. Wood, and D. R. Clarke, "Multilayer dielectric elastomers for fast, programmable actuation without prestretch," Adv. Mater. **28**(36), 8058–8063 (2016).
[12]A. O'Halloran, F. O'Malley, and P. McHugh, "A review on dielectric elastomer actuators, technology, applications, and challenges," J. Appl. Phys. **104**(7), 071101 (2008).
[13]P. Brochu and Q. Pei, "Advances in dielectric elastomers for actuators and artificial muscles," Macromol. Rapid Commun. **31**(1), 10–36 (2010).
[14]S. Rosset and H. R. Shea, "Flexible and stretchable electrodes for dielectric elastomer actuators," Appl. Phys. A **110**(2), 281–307 (2013).
[15]L. J. Romasanta, M. A. López-Manchado, and R. Verdejo, "Increasing the performance of dielectric elastomer actuators: A review from the materials perspective," Prog. Polym. Sci. **51**, 188–211 (2015).
[16]G.-Y. Gu *et al.*, "A survey on dielectric elastomer actuators for soft robots," Bioinspir. Biomim. **12**(1), 011003 (2017).
[17]N. Wang *et al.*, "Advances in dielectric elastomer actuation technology," Sci. China Technol. Sci. **61**(10), 1512–1527 (2018).
[18]X. Cao *et al.*, "Review of soft linear actuator and the design of a dielectric elastomer linear actuator," Acta Mech. Solida Sin. **32**(5), 566–579 (2019).
[19]U. Gupta *et al.*, "Soft robots based on dielectric elastomer actuators: A review," Smart Mater. Struct. **28**(10), 103002 (2019).
[20]J.-H. Youn *et al.*, "Dielectric elastomer actuator for soft robotics applications and challenges," Appl. Sci. **10**(2), 640 (2020).
[21]T. Lu, C. Ma, and T. Wang, "Mechanics of dielectric elastomer structures: A review," Extreme Mech. Lett. **38**, 100752 (2020).
[22]H. E. Huxley, "The mechanism of muscular contraction," Science **164**(3886), 1356–1366 (1969).
[23]R. J. Full and K. Meijer, "Chapter 3: Metrics of natural muscle function," in *Electroactive Polymer (EAP) Actuators as Artificial Muscles Reality, Potential, and Challenges*, edited by Y. Bar-Cohen (SPIE Press, 2004).
[24]R. J. Full and K. Meijer, "Artificial muscles versus natural actuators from frogs to flies," in *Smart Structures and Materials 2000 Electroactive Polymer Actuators and Devices (EAPAD)* (International Society for Optics and Photonics, 2000).
[25]D. E. Rassier, B. R. MacIntosh, and W. Herzog, "Length dependence of active force production in skeletal muscle," J. Appl. Physiol. **86**(5), 1445–1457 (1999).
[26]M. Vatankhah-Varnoosfaderani *et al.*, "Bottlebrush elastomers: A new platform for freestanding electroactuation," Adv. Mater. **29**(2), 1604209 (2017).
[27]M. Duduta *et al.*, "Realizing the potential of dielectric elastomer artificial muscles," Proc. Natl. Acad. Sci. U.S.A. **116**(7), 2476–2481 (2019).
[28]R. J. Full, "Invertebrate locomotor systems," in *Comprehensive Physiology* (John Wiley and Sons, 2010), pp. 853–930.
[29]T. Li *et al.*, "Giant voltage-induced deformation in dielectric elastomers near the verge of snap-through instability," J. Mech. Phys. Solids **61**(2), 611–628 (2013).
[30]G. M. Rebeiz, *RF MEMS: Theory, Design, and Technology* (John Wiley & Sons, 2004).
[31]A. N. Gent, "A new constitutive relation for rubber," Rubber Chem. Technol. **69**(1), 59–61 (1996).
[32]C. O. Horgan and G. Saccomandi, "Constitutive models for compressible nonlinearly elastic materials with limiting chain extensibility," J. Elast. **77**(2), 123–138 (2004).
[33]J. C. Simo and K. S. Pister, "Remarks on rate constitutive equations for finite deformation problems: Computational implications," Comput. Methods Appl. Mech. Eng. **46**(2), 201–215 (1984).
[34]B. Erman, "Molecular aspects of rubber elasticity," in *Mechanics and Thermomechanics of Rubberlike Solids* (Springer, 2004), pp. 63–89.
[35]S. M. Ha *et al.*, "Interpenetrating polymer networks for high-performance electroelastomer artificial muscles," Adv. Mater. **18**(7), 887–891 (2006).
[36]G. Zurlo *et al.*, "Catastrophic thinning of dielectric elastomers," Phys. Rev. Lett. **118**(7), 078001 (2017).
[37]D. De Tommasi, G. Puglisi, and G. Zurlo, "Inhomogeneous deformations and pull-in instability in electroactive polymeric films," Int. J. Non-Linear Mech. **57**, 123–129 (2013).
[38]J. Zhu *et al.*, "Two types of transitions to wrinkles in dielectric elastomers," Soft Matter **8**(34), 8840–8846 (2012).
[39]R. Huang and Z. Suo, "Electromechanical phase transition in dielectric elastomers," Proc. R. Soc. Lond. Ser. A **468**(2140), 1014–1040 (2012).
[40]A. T. Conn and J. Rossiter, "Harnessing electromechanical membrane wrinkling for actuation," Appl. Phys. Lett. **101**(17), 171906 (2012).
[41]H. Godaba *et al.*, "Instabilities in dielectric elastomers: Buckling, wrinkling, and crumpling," Soft Matter **15**(36), 7137–7144 (2019).
[42]L. R. G. Treloar, *The Physics of Rubber Elasticity* (Oxford University Press, 1975).
[43]J. E. Mark and B. Erman, *Rubberlike Elasticity: A Molecular Primer* (Cambridge University Press, 2007).
[44]M. Warner and E. M. Terentjev, *Liquid Crystal Elastomers* (Oxford University Press, 2007), Vol. 120.
[45]F. B. Madsen *et al.*, "A new soft dielectric silicone elastomer matrix with high mechanical integrity and low losses," RSC Adv. **5**(14), 10254–10259 (2015).
[46]A. G. Bejenariu, L. Yu, and A. L. Skov, "Low moduli elastomers with low viscous dissipation," Soft Matter **8**(14), 3917–3923 (2012).
[47]P. Mazurek, S. Vudayagiri, and A. L. Skov, "How to tailor flexible silicone elastomers with mechanical integrity: A tutorial review," Chem. Soc. Rev. **48**(6), 1448–1464 (2019).
[48]R. E. Pelrine, R. D. Kornbluh, and J. P. Joseph, "Electrostriction of polymer dielectrics with compliant electrodes as a means of actuation," Sens. Actuators, A **64**(1), 77–85 (1998).
[49]J. Kim *et al.*, "Designing responsive buckled surfaces by halftone gel lithography," Science **335**(6073), 1201–1205 (2012).
[50]Y. Qiu *et al.*, "Dielectric elastomer artificial muscle: Materials innovations and device explorations," Acc. Chem. Res. **52**(2), 316–325 (2019).
[51]C. J. Lawrence, "The mechanics of spin coating of polymer films," Phys. Fluids **31**(10), 2786–2795 (1988).
[52]D. B. Hall, P. Underhill, and J. M. Torkelson, "Spin coating of thin and ultrathin polymer films," Polym. Eng. Sci. **38**(12), 2039–2045 (1998).
[53]M. Jabbari *et al.*, "Ceramic tape casting: A review of current methods and trends with emphasis on rheological behaviour and flow analysis," Mater. Sci. Eng. B **212**, 39–61 (2016).
[54]R. R. Søndergaard, M. Hösel, and F. C. Krebs, "Roll-to-roll fabrication of large area functional organic materials," J. Polym. Sci., Part B: Polym. Phys. **51**(1), 16–34 (2013).
[55]D. McCoul *et al.*, "Inkjet 3D printing of UV and thermal cure silicone elastomers for dielectric elastomer actuators," Smart Mater. Struct. **26**(12), 125022 (2017).
[56]G. Kofod, H. Stoyanov, and R. Gerhard, "Multilayer coaxial fiber dielectric elastomers for actuation and sensing," Appl. Phys. A **102**(3), 577–581 (2011).
[57]A. Poulin, S. Rosset, and H. R. Shea, "Printing low-voltage dielectric elastomer actuators," Appl. Phys. Lett. **107**(24), 244104 (2015).
[58]M. C. Boyce and E. M. Arruda, "Constitutive models of rubber elasticity: A review," Rubber Chem. Technol. **73**(3), 504–523 (2000).
[59]C. O. Horgan and G. Saccomandi, "A molecular-statistical basis for the Gent constitutive model of rubber elasticity," J. Elast. **68**(1–3), 167–176 (2002).
[60]X. Niu *et al.*, "Synthesizing a new dielectric elastomer exhibiting large actuation strain and suppressed electromechanical instability without prestretching," J. Polym. Sci., Part B: Polym. Phys. **51**(3), 197–206 (2013).
[61]J. Huang *et al.*, "The thickness and stretch dependence of the electrical breakdown strength of an acrylic dielectric elastomer," Appl. Phys. Lett. **101**(12), 122905 (2012).

[62]D. Gatti *et al.*, "The dielectric breakdown limit of silicone dielectric elastomer actuators," Appl. Phys. Lett. **104**(5), 052905 (2014).
[63]S. Zakaria *et al.*, "The electrical breakdown strength of pre-stretched elastomers, with and without sample volume conservation," Smart Mater. Struct. **24**(5), 055009 (2015).
[64]M. Sparks *et al.*, "Theory of electron-avalanche breakdown in solids," Phys. Rev. B **24**(6), 3519–3536 (1981).
[65]N. Zebouchi *et al.*, "Electrical breakdown theories applied to polyethylene terephthalate films under the combined effects of pressure and temperature," J. Appl. Phys. **79**(5), 2497–2501 (1996).
[66]L. A. Dissado and J. C. Fothergill, *Electrical Degradation and Breakdown in Polymers* (IET, 1992), Vol. 9.
[67]K. C. Kao, *Dielectric Phenomena in Solids* (Elsevier, 2004).
[68]M. A. Alam, B. E. Weir, and P. J. Silverman, "A study of soft and hard breakdown—Part I: Analysis of statistical percolation conductance," IEEE Trans. Electron Devices **49**(2), 232–238 (2002).
[69]F. Forlani and N. Minnaja, "Thickness influence in breakdown phenomena of thin dielectric films," Phys. Status Solidi B **4**(2), 311–324 (1964).
[70]W. Yuan *et al.*, "Fault-tolerant dielectric elastomer actuators using single-walled carbon nanotube electrodes," Adv. Mater. **20**(3), 621–625 (2008).
[71]H. Zhao *et al.*, "Compact dielectric elastomer linear actuators," Adv. Funct. Mater. **28**(42), 1804328 (2018).
[72]F. Carpi *et al.*, "Standards for dielectric elastomer transducers," Smart Mater. Struct. **24**(10), 105025 (2015).
[73]T. Nitta, N. Yamada, and Y. Fujiwara, "Area effect of electrical breakdown in compressed SF6," IEEE Trans. Power Appar. Syst. **2**, 623–629 (1974).
[74]V. K. Agarwal and V. K. Srivastava, "Thickness dependence of breakdown field in thin films," Thin Solid Films **8**(5), 377–381 (1971).
[75]H. K. Kim and F. G. Shi, "Thickness dependent dielectric strength of a low-permittivity dielectric film," IEEE Trans. Dielectr. Electr. Insul. **8**(2), 248–252 (2001).
[76]G. Kofod *et al.*, "Actuation response of polyacrylate dielectric elastomers," J. Intell. Mater. Syst. Struct. **14**(12), 787–793 (2003).
[77]M. Kollosche and G. Kofod, "Electrical failure in blends of chemically identical, soft thermoplastic elastomers with different elastic stiffness," Appl. Phys. Lett. **96**(7), 071904 (2010).
[78]R. Degraeve *et al.*, "New insights in the relation between electron trap generation and the statistical properties of oxide breakdown," IEEE Trans. Electron Devices **45**(4), 904–911 (1998).
[79]H. Stoyanov *et al.*, "Dielectric properties and electric breakdown strength of a subpercolative composite of carbon black in thermoplastic copolymer," Appl. Phys. Lett. **94**(23), 232905 (2009).
[80]H. Silau *et al.*, "Weibull analysis of electrical breakdown strength as an effective means of evaluating elastomer thin film quality," Adv. Eng. Mater. **20**(9), 1800241 (2018).
[81]G. Chen *et al.*, "Origin of thickness dependent dc electrical breakdown in dielectrics," Appl. Phys. Lett. **100**(22), 222904 (2012).
[82]A. Bradwell, R. Cooper, and B. Varlow, "Conduction in polythene with strong electric fields and the effect of prestressing on the electric strength," in *Proceedings of the Institution of Electrical Engineers* (IET, 1971).
[83]K. Matsui *et al.*, "Space charge behavior in low density polyethylene at prebreakdown," IEEE Trans. Dielectr. Electr. Insul. **12**(3), 406–415 (2005).
[84]E. M. Arruda and P. A. Przybylo, "An investigation into the three-dimensional stress-birefringence-strain relationship in elastomers," Polym. Eng. Sci. **35**(5), 395–402 (1995).
[85]P. R. Von Lockette and E. Arruda, "A network description of the non-Gaussian stress-optic and Raman scattering responses of elastomer networks," Acta Mech. **134**(1–2), 81–107 (1999).
[86]A. Conn and J. Rossiter, "Radially expanding mechanism for dielectric elastomers," in *Electroactive Polymer Actuators and Devices (EAPAD) 2010* (International Society for Optics and Photonics, 2010).
[87]J.-L. Parpal, J.-P. Crine, and C. Dang, "Electrical aging of extruded dielectric cables. A physical model," IEEE Trans. Dielectr. Electr. Insul. **4**(2), 197–209 (1997).
[88]L. A. Dissado, G. Mazzanti, and G. C. Montanari, "The role of trapped space charges in the electrical aging of insulating materials," IEEE Trans. Dielectr. Electr. Insul. **4**(5), 496–506 (1997).
[89]H. Stoyanov *et al.*, "Elastic block copolymer nanocomposites with controlled interfacial interactions for artificial muscles with direct voltage control," Soft Matter **7**(1), 194–202 (2011).
[90]Y. Song *et al.*, "Improving the dielectric constants and breakdown strength of polymer composites: Effects of the shape of the $BaTiO_3$ nanoinclusions, surface modification and polymer matrix," J. Mater. Chem. **22**(32), 16491–16498 (2012).
[91]B. Chen *et al.*, "Highly stretchable and transparent ionogels as nonvolatile conductors for dielectric elastomer transducers," ACS Appl. Mater. Interfaces **6**(10), 7840–7845 (2014).
[92]Z.-M. Dang, Y.-H. Lin, and C.-W. Nan, "Novel ferroelectric polymer composites with high dielectric constants," Adv. Mater. **15**(19), 1625–1629 (2003).
[93]F. Carpi *et al.*, "Silicone–poly (hexylthiophene) blends as elastomers with enhanced electromechanical transduction properties," Adv. Funct. Mater. **18**(2), 235–241 (2008).
[94]S. Shian *et al.*, "Highly compliant transparent electrodes," Appl. Phys. Lett. **101**(6), 061101 (2012).
[95]Y. Liu *et al.*, "Ultra-compliant liquid metal electrodes with in-plane self-healing capability for dielectric elastomer actuators," Appl. Phys. Lett. **103**(6), 064101 (2013).
[96]I. Balberg *et al.*, "Excluded volume and its relation to the onset of percolation," Phys. Rev. B **30**(7), 3933–3943 (1984).
[97]B. J. Last and D. J. Thouless, "Percolation theory and electrical conductivity," Phys. Rev. Lett. **27**(25), 1719–1721 (1971).
[98]S. Kirkpatrick, "Percolation and conduction," Rev. Mod. Phys. **45**(4), 574–588 (1973).
[99]L. Hu, D. S. Hecht, and G. Grüner, "Percolation in transparent and conducting carbon nanotube networks," Nano Lett. **4**(12), 2513–2517 (2004).
[100]Z. Wu *et al.*, "Transparent, conductive carbon nanotube films," Science **305**(5688), 1273–1276 (2004).
[101]F. Hennrich *et al.*, "Preparation, characterization and applications of free-standing single walled carbon nanotube thin films," Phys. Chem. Chem. Phys. **4**(11), 2273–2277 (2002).
[102]B. Zhao *et al.*, "Synthesis and characterization of water soluble single-walled carbon nanotube graft copolymers," J. Am. Chem. Soc. **127**(22), 8197–8203 (2005).
[103]E. Bekyarova *et al.*, "Electronic properties of single-walled carbon nanotube networks," J. Am. Chem. Soc. **127**(16), 5990–5995 (2005).
[104]E. Gracia-Espino *et al.*, "Electrical transport and field-effect transistors using inkjet-printed SWCNT films having different functional side groups," ACS Nano **4**(6), 3318–3324 (2010).
[105]H.-Z. Geng *et al.*, "Effect of acid treatment on carbon nanotube-based flexible transparent conducting films," J. Am. Chem. Soc. **129**(25), 7758–7759 (2007).
[106]T. Kim *et al.*, "Inkjet-printed stretchable single-walled carbon nanotube electrodes with excellent mechanical properties," Appl. Phys. Lett. **104**(11), 113103 (2014).
[107]R. Graupner *et al.*, "Doping of single-walled carbon nanotube bundles by Brønsted acids," Phys. Chem. Chem. Phys. **5**(24), 5472–5476 (2003).
[108]R. S. Lee *et al.*, "Conductivity enhancement in single-walled carbon nanotube bundles doped with K and Br," Nature **388**(6639), 255–257 (1997).
[109]Y. Zhou, L. Hu, and G. Grüner, "A method of printing carbon nanotube thin films," Appl. Phys. Lett. **88**(12), 123109 (2006).
[110]R. D. Deegan *et al.*, "Capillary flow as the cause of ring stains from dried liquid drops," Nature **389**(6653), 827–829 (1997).
[111]R. G. Larson, "Transport and deposition patterns in drying sessile droplets," AIChE J. **60**(5), 1538–1571 (2014).
[112]J.-W. Song *et al.*, "Inkjet printing of single-walled carbon nanotubes and electrical characterization of the line pattern," Nanotechnology **19**(9), 095702 (2008).
[113]M. J. Owen and P. J. Smith, "Plasma treatment of polydimethylsiloxane," J. Adhes. Sci. Technol. **8**(10), 1063–1075 (1994).
[114]B. Olander, A. Wirsén, and A.-C. Albertsson, "Oxygen microwave plasma treatment of silicone elastomer: Kinetic behavior and surface composition," J. Appl. Polym. Sci. **91**(6), 4098–4104 (2004).

[115]C. Baechler *et al.*, "Inkjet printed multiwall carbon nanotube electrodes for dielectric elastomer actuators," Smart Mater. Struct. **25**(5), 055009 (2016).
[116]K. Kordás *et al.*, "Inkjet printing of electrically conductive patterns of carbon nanotubes," Small **2**(8–9), 1021–1025 (2006).
[117]R. C. Tenent *et al.*, "Ultrasmooth, large-area, high-uniformity, conductive transparent single-walled-carbon-nanotube films for photovoltaics produced by ultrasonic spraying," Adv. Mater. **21**(31), 3210–3216 (2009).
[118]S. Kim *et al.*, "Spin-and spray-deposited single-walled carbon-nanotube electrodes for organic solar cells," Adv. Funct. Mater. **20**(14), 2310–2316 (2010).
[119]B. P. Bewlay and B. Cantor, "Gas velocity measurements from a close-coupled spray deposition atomizer," Mater. Sci. Eng. A **118**, 207–222 (1989).
[120]D. J. Lipomi *et al.*, "Skin-like pressure and strain sensors based on transparent elastic films of carbon nanotubes," Nat. Nanotechnol. **6**(12), 788–792 (2011).
[121]Y. Zhang *et al.*, "Polymer-embedded carbon nanotube ribbons for stretchable conductors," Adv. Mater. **22**(28), 3027–3031 (2010).
[122]L. Jin *et al.*, "Microstructural origin of resistance–strain hysteresis in carbon nanotube thin film conductors," Proc. Natl Acad. Sci. U.S.A. **115**(9), 1986–1991 (2018).
[123]F. Xu and Y. Zhu, "Highly conductive and stretchable silver nanowire conductors," Adv. Mater. **24**(37), 5117–5122 (2012).
[124]L. Hu *et al.*, "Highly stretchable, conductive, and transparent nanotube thin films," Appl. Phys. Lett. **94**(16), 161108 (2009).
[125]S. Rosset *et al.*, "Assessing the degradation of compliant electrodes for soft actuators," Rev. Sci. Instrum. **88**(10), 105002 (2017).
[126]J. Grosser and H. Schulz, "Electrostatic screening by a plane grid," J. Phys. D: Appl. Phys. **22**(6), 723–729 (1989).
[127]H. Heywang, "Physikalische und chemische Vorgänge in selbstheilenden Kunststoff-Kondensatoren," Colloid Polym. Sci. **254**(2), 139–147 (1976).
[128]C. W. Reed and S. W. Cichanowski, "The fundamentals of aging in Hv polymer-film capacitors," IEEE Trans. Dielectr. Electr. Insul. **1**(5), 904–922 (1994).
[129]P. G. Collins, M. S. Arnold, and P. Avouris, "Engineering carbon nanotubes and nanotube circuits using electrical breakdown," Science **292**(5517), 706–709 (2001).
[130]H. Stoyanov *et al.*, "Long lifetime, fault-tolerant freestanding actuators based on a silicone dielectric elastomer and self-clearing carbon nanotube compliant electrodes," RSC Adv. **3**(7), 2272–2278 (2013).
[131]R. Becker and F. Sauter, *Electromagnetic Fields and Interactions* (Courier Corporation, 1982), Vol. 1.
[132]R. J. Baskin and P. J. Paolini, "Volume change and pressure development in muscle during contraction," Am. J. Physiol. **213**(4), 1025–1030 (1967).
[133]D. A. Morrow *et al.*, "Transversely isotropic tensile material properties of skeletal muscle tissue," J. Mech. Behav. Biomed. Mater. **3**(1), 124–129 (2010).
[134]T. Lu *et al.*, "Dielectric elastomer actuators under equal-biaxial forces, uniaxial forces, and uniaxial constraint of stiff fibers," Soft Matter **8**(22), 6167–6173 (2012).
[135]H. Zhao *et al.*, "A wearable soft haptic communicator based on dielectric elastomer actuators," Soft Rob. **7**, 451 (2020).
[136]Y. Chen *et al.*, "Controlled flight of a microrobot powered by soft artificial muscles," Nature **575**(7782), 324–329 (2019).
[137]Q. Pei *et al.*, "Multiple-degrees-of-freedom electroelastomer roll actuators," Smart Mater. Struct. **13**(5), N86–N92 (2004).
[138]A. Chortos *et al.*, "Printing reconfigurable bundles of dielectrice elastomer fibers" Adv. Funct. Mater. (published online) (2021).
[139]I. A. Anderson *et al.*, "A thin membrane artificial muscle rotary motor," Appl. Phys. A **98**(1), 75–83 (2010).
[140]A. She *et al.*, "Adaptive metalenses with simultaneous electrical control of focal length, astigmatism, and shift," Sci. Adv. **4**(2), eaap9957 (2018).
[141]S. Shian, R. M. Diebold, and D. R. Clarke, "Tunable lenses using transparent dielectric elastomer actuators," Opt. Express **21**(7), 8669–8676 (2013).
[142]F. Carpi *et al.*, "Bioinspired tunable lens with muscle-like electroactive elastomers," Adv. Funct. Mater. **21**(21), 4152–4158 (2011).
[143]M. Hodgins, A. York, and S. Seelecke, "Experimental comparison of bias elements for out-of-plane DEAP actuator system," Smart Mater. Struct. **22**(9), 094016 (2013).
[144]C. Cao, X. Gao, and A. Conn, "A compliantly coupled dielectric elastomer actuator using magnetic repulsion," Appl. Phys. Lett. **114**(1), 011904 (2019).
[145]A. T. Conn and J. Rossiter, "Towards holonomic electro-elastomer actuators with six degrees of freedom," Smart Mater. Struct. **21**(3), 035012 (2012).
[146]S. Shian, K. Bertoldi, and D. R. Clarke, "Dielectric elastomer based "grippers" for soft robotics," Adv. Mater. **27**(43), 6814–6819 (2015).
[147]Y. Klein, E. Efrati, and E. Sharon, "Shaping of elastic sheets by prescription of non-Euclidean metrics," Science **315**(5815), 1116–1120 (2007).
[148]P. G. Ciarlet, "An introduction to differential geometry with applications to elasticity," J. Elast. **78**(1–3), 1–215 (2005).
[149]E. Hajiesmaili and D. R. Clarke, "Reconfigurable shape-morphing dielectric elastomers using spatially varying electric fields," Nat. Commun. **10**(1), 1–7 (2019).
[150]E. Hajiesmaili *et al.*, "Voltage-controlled morphing of dielectric elastomer circular sheets into conical surfaces," Extreme Mech. Lett. **30**, 100504 (2019).
[151]A. Chortos *et al.*, "3D printing of interdigitated dielectric elastomer actuators," Adv. Funct. Mater. **30**(1), 1907375 (2020).
[152]C. Modes, K. Bhattacharya, and M. Warner, "Gaussian curvature from flat elastica sheets," Proc. R. Soc. London Ser. A **467**(2128), 1121–1140 (2011).
[153]D. L. Henann, S. A. Chester, and K. Bertoldi, "Modeling of dielectric elastomers: Design of actuators and energy harvesting devices," J. Mech. Phys. Solids **61**(10), 2047–2066 (2013).
[154]S. Pourazadi *et al.*, "On the electrical safety of dielectric elastomer actuators in proximity to the human body," Smart Mater. Struct. **26**(11), 115007 (2017).
[155]L. B. Valdes, "Resistivity measurements on germanium for transistors," Proc. IRE **42**(2), 420–427 (1954).